論文 / 著書情報
Article / Book Information

題目(和文)	Al-Mg-Cu合金における時効硬化挙動とナノ構造の形成
Title(English)	Age-hardening Behavior with Evolution of Nanostructures in Al-Mg-Cu Alloys
著者(和文)	三原麻未
Author(English)	Mami Mihara
出典(和文)	学位:博士(工学), 学位授与機関:東京工業大学, 報告番号:甲第10440号, 授与年月日:2017年3月26日, 学位の種別:課程博士, 審査員:小林 郁夫,藤居 俊之,熊井 真次,曽根 正人,村石 信二
Citation(English)	Degree:Doctor (Engineering), Conferring organization: Tokyo Institute of Technology, Report number:甲第10440号, Conferred date:2017/3/26, Degree Type:Course doctor, Examiner:,,,,
学位種別(和文)	博士論文
Type(English)	Doctoral Thesis

Age-hardening Behavior with Evolution of Nanostructures in Al-Mg-Cu Alloys

by

Mami Mihara

Doctoral Thesis

Department of Metallurgy and Ceramics Science

Tokyo Institute of Technology

2016

Acknowledgements

There are many people I'd like to thank for their kind support during this PhD work. Firstly, I would like to express my sincere gratitude to my supervisor **Prof. Equo Kobayashi**. His advice helped me in all time of research and writing of this thesis. I am deeply grateful to **Prof. Tatsuo Sato** who was my supervisor during master course for enlightening me the first glance of research. I also thank **Mr. Hiroyasu Tezuka** for giving me a lot of advice on my research and taking me out for drinking.

Besides my supervisors, I would like to thank the rest of my thesis committee: **Prof. Toshiyuki Fujii**, **Prof. Shinji Muraishi, Prof. Masato Sone** and **Prof. Shinji Kumai** for their insightful and meticulous comments and encouragement, but also for the hard questions which incented me to widen my research from various perspectives.

My sincere thanks also go to **Prof. Randi Holmestad** who provided me an opportunity to join her TEM group in Trondheim for five months in 2014. This experience has changed my life. I would like to thank **Dr. Calin D. Marioara** and **Dr. Sigmund Andersen** for continuous support of my Ph.D study since 2014, for their motivation and immense knowledge. I also thank **Prof. Knut Martinsen**, **Dr. Sigurd Wenner** and **Dr. Takeshi Saito** for their advice and concern.

For another international collaboration, I am grateful to **Prof. Alberto Somoza** and **Dr. Carlos Macchi** who gave me an opportunity to visit Tandil to use the positron annihilation spectroscopy. Without their support, it would not be possible to complete this research.

Those international collaborations with distinguished researchers during my PhD were supported by **ACEEES** program. Special thanks must go to ACEEES. I deeply appreciate **Prof. Masao Takeyama** for his constructive comments and warm encouragement through ACEEES program.

I also would like to thank **Dr. Yasuhiro Aruga** and **Dr. Masaya Kozuka** who provided me an opportunity to use the atom probe tomography. Their generous support were invaluable.

My sincere appreciation also go to **Dr. JaeHwang Kim**, **Prof. Tomo Ogura** and **Prof. Shoichi Hirosawa** for their concern and encouragement.

I'm deeply grateful to **UACJ Corporation** for material supply. My heartfelt appreciation goes to **Japan Aluminium Association** Research Grant Program for the financial support.

I thank my fellow labmates for the stimulating discussions, for the sleepless nights we were working together before deadlines, and for all the fun we have had. In particular, I would thank **Dr. SeongNyeong Kim**. I will never forget about both hard days and nice days we spent together in Tokyo Tech.

Finally, I would like to thank **my family**: my parents, brother and sister for supporting me spiritually throughout writing this thesis and my life in general.

Abstract of the present thesis

Characteristic age-hardening behavior in Al-Mg-Cu(-Ag) alloys was investigated by a combination of the several experimental techniques. The composition of the Base alloy is located within the (α+S+T) phase field. During aging at 443 K, the hardness changed in three distinct stages separated by a plateau, where the hardness remains constant for a long time. The first stage of age-hardening occurs rapidly and is completed after aging for 0.06 ks at 443 K. It contributes as much as 60% of the total hardening. This phenomena is called rapid age-hardening. A large exothermic peak was detected in the A.Q. state specimens using DSC analysis. This peak disappears after short term aging and is attributed to the formation of nanostructures which is responsible for the rapid age-hardening. In both alloys, after aging at 443 K for 0.06 ks, formation of the nanostructures associated with Cu aggregates were identified as the structural units of GPB zone by HAADF-STEM investigation. Small amount of Ag addition promoted the units to grow to form the spherical zones. The zones contributes the further increase in the hardness during the rapid age-hardening. 3DAP data clearly suggested that Cu aggregates were formed after short term aging. Moreover, PAS investigation revealed that the rapid age-hardening in both alloys is related to the rapid increase of the Cu atoms in contact with vacancies during aging. It also revealed that Ag addition promoted more vacancies to be retained after quenching and during aging. At the peak aging, three types of precipitates were formed and were identified as GPB zone, S' and Z phase in the Base alloy. The Ag addition changed the microstructure drastically and improved the age-hardenability. Fine distributed precipitates formed in the Ag-added alloy was identified as icosahedral quasi-crystalline (iQC) intermixed with T phase.

概要

本論文は（α＋S+T）相領域に位置する合金組成を持つ Al-Mg-Cu 合金に着目し，特異な時効硬化挙動ならびにそれに伴う微細組織の形成挙動を解明した．また，種々の実験手法を相補的に用いることで，急速時効硬化現象の起源と考えられる，短時間時効熱処理によって形成するナノ組織の形成挙動を明らかにした．さらに，マイクロアロイング元素として効果的な Ag 添加に着目し，Ag 添加の影響について明らかにした．本論文は 6 章から構成され，各章の概要は以下の通りである．

第 1 章では本研究の背景として，基本的なアルミニウム合金の強化機構ならびに Al-Mg-Cu 合金の特異な時効硬化挙動について述べた．Al-Cu-Mg 合金系についての時効初期の急速時効硬化現象の起源としては様々な説が唱えられているが，いまだ統一的な解釈に至っていない．特に，状態図上で（α+S+T）相領域に位置する Al-Mg-Cu 合金についての報告は限られており，この相領域に位置しながら T 相の析出が認められないとの報告もあり，析出過程が十分に明らかにされていない．従来の報告を背景に，時効初期の微細組織形成挙動，空孔挙動ならびに析出過程を明らかにすることの重要性を指摘した．また，マイクロアロイングは本合金系の時効硬化性向上に非常に有効であり，特に微量 Ag 添加による効果は著しく，合金組成に依存して異なる新たな析出相が形成すると報告されている．Al-Mg-Cu 合金では Z 相の析出が報告されているが，十分に検討されていない．以上を背景に，微量 Ag 添加が時効硬化挙動に及ぼす影響について明らかにすることの必要性を示し，本研究の意義と目的を示した．第 2 章では Al-Mg-Cu 合金の基本的な時効硬化挙動について，硬さ試験，電気比抵抗測定，熱分析（DSC 測定），TEM 観察などの手法を用いて詳細に検討した．その結果，Al-Mg-Cu 合金は第一硬化段階，plateau 段階および第二硬化段階の三段階で時効硬化することを示した．また，第一硬化段階では急速に時効硬化し（170℃時効で 1 分），それに伴い電気比抵抗が増大することを明らかにした．電気比抵抗増加は溶質原子の集合体形成に起因すると考えられ，DSC 測定により，それに伴う発熱ピークが認められた．一方，長時間時効材の TEM 観察により，第二硬化段階は GPB ゾーンおよび S' 相の形成によることを明らかにした．HAADF-STEM 観察により，GPB ゾーンは構造ユニットの

集合体として理解できることを示した．ピーク時効材ではそれらの析出相に加え，新たに Z 相が析出することを明らかにした．第 3 章では HAADF-STEM 観察，3 次元アトムプローブ法（3DAP），陽電子消滅法（PAS）を用いて，急速時効硬化が起こる時効初期の微細組織形成挙動について検討した．その結果， Cu 原子の明るいコントラストから，1 分の時効熱処理によって GPB ゾーンの構造ユニットの最小単位がすでに形成していることを初めて明らかにした．さらに，1 分および 1 時間時効材の 3DAP 解析により，Cu 原子周囲の Cu 濃度が合金組成と比べ際立って高いことを明らかにした．また，PAS の手法の一つである同時計数ドップラー拡がり法により，1 分の時効熱処理によって空孔付近の Cu 濃度が急激に増大することを明らかにした．第 4 章では Cu および Mg の添加量を変化させ，合金組成が時効硬化挙動に及ぼす影響について硬さ試験，電気比抵抗測定，熱分析（DSC 測定），PAS 測定および引張試験によって検討した．その結果，本合金における Cu 添加量を増やすことで，時効初期の GPB ゾーンの構造ユニットの形成量が増大し，急速時効硬化が促進されることを明らかにした．一方，PAS 解析により Mg 添加量を増やすことによる焼入れ過剰空孔量の増大が示唆されたが，時効硬化性の向上は顕著ではない．また，A.Q.材における引張試験により，応力-ひずみ線上に応力変動（セレーション）が発生することを示した．長時間時効後もセレーションは残存し，セレーションを発生する固溶 Mg 原子が多く存在していることを示した．第 5 章では微量 Ag 添加が時効硬化挙動および微細組織形成挙動に及ぼす影響について詳細に検討した．その結果，T 相が微細・均一かつ高密に析出し，本合金の時効硬化性が向上することを示した． T 相に対する詳細な HAADF-STEM 観察により，一部で準結晶が形成していることを初めて明らかにした．また，1 分時効材の HAADF-STEM 観察により，GPB ゾーンの構造ユニットとそれらが成長した球状ゾーンが形成していることを明らかにした．三元合金同様，時効初期に形成し急速時効硬化に寄与する微細組織は GPB ゾーンの構造ユニットであり，微量 Ag 添加によって棒状の GPB ゾーンとは異なる球状のゾーン形成が促進されることを初めて明らかにした．また，微量 Ag 添加によってより多量の空孔が焼入れ後に凍結し，時効熱処理後もそれらが維持されることを明らかにした．第 6 章では各章で得られた結果をまとめ，本研究の総括を述べた．

Table of Contents

Chapter 1

General Introduction

1.1 Motivation

Aluminum is the third most abundant metal on the Earth's surface. Nowadays, aluminum products are found everywhere. It supports our society and enriches our life. The versatility of aluminum makes it the most widely used metal after steel, for instance automotive body panels, beverages, window frames, foil, digital home appliances and so on. Comparing to other light metals, the consumption of aluminum has been dramatically increased all over the world as shown in **Fig. 1.1** [1]. By utilizing various combinations of aluminum's properties such as strength, lightness, corrosion resistance, recyclability and formability, aluminum is being employed in an ever-increasing number of applications. In particular, from an environmental point of view, the application of aluminum for automobiles is important since the light-weighting is effective to reduce the emission of CO_2 which causes global warming. A car with 40 percent recycled aluminum has a lifetime energy saving of 680 liters of gasoline and a lifetime emission saving of 1,950 kg of CO_2 [2].

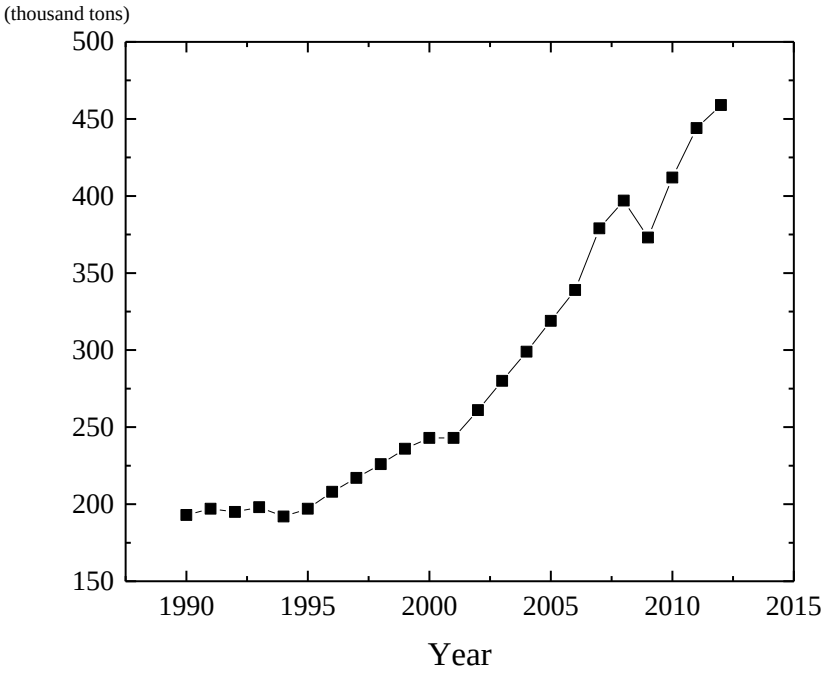

Fig. 1.1 History of world Aluminum production [1].

Al-Mg based alloys have been widely utilized as transportation material in automotive applications because of their excellent properties such as high strength to weight ratio, ductility and corrosion resistance. During the paint baking treatment (i.e. heat treating the body panel sheets for 20-30 min at temperatures between 433K and 453 K after painting) for automotive body applications, softening might occur in classical Al-Mg alloys. It can be overcome by the addition of small amounts of Cu [3,4]. By addition of Cu, formation of nano-sized fine precipitates is obtained during heat treatment and the hardness is increased. This is called precipitation hardening. There has been limited number of published work, regarding the precipitation processes occurring in these Cu-lean alloys [3,4], compared to the Al-Cu-Mg system [5-20]. Al-Mg-Cu system has started to attract many scientists recently [21-25], although it remains complicated and unclarified phenomena.

Al-Mg-Cu alloy shows rapid age-hardening during aging at medium temperatures and stable strength at a room temperature which are characteristic feature of this alloy system. This does not occur in binary Al-Cu and Al-Mg alloys nor in general within ternary Al-Cu-Mg alloys which have phase compositions in the $\alpha+\theta$ field (high Cu/Mg ratio), even though all are age-hardenable [26-28]. In general, the precipitate microstructure has a significant influence on properties of the aluminum alloys, which are dominated by the alloy composition and the heat treatment procedure. In Al-Mg-Cu alloy, rapid age-hardening is now believed to be attributed to the formation of solute clusters which is the precursor of precipitates. This is so called cluster hardening. Cluster hardening was originally proposed in Al-Cu-Mg alloys, which concluded that the rapid age-hardening is due to solute clustering rather than precipitate formation. Although some researchers propose the dislocation-solute atom interaction as the origin of rapid age-hardening, there is still no unified interpretation. In order to clarify the origin of the rapid age-hardening, investigation of the formation behavior of solute clusters and its effect on the age-hardening is crucial.

Another interesting point of the age-hardening in a wide range of compositions based on the Al-Cu-Mg system is that the effect of Ag addition which changes the precipitate morphology and accelerates the age-hardening response dramatically [29-31]. This is so called microalloying effect. Furthermore, depending on the Mg:Cu ratios of the alloys, Ag has been found to promote formation of three new precipitates. In Cu lean Al-Mg-Cu alloys, Z phase is formed by Ag addition. Some researchers reported that Z phase can be detected even in Al-Mg-Cu ternary alloys, however it has been less investigated [22, 23, 25].

The principle objective of the present thesis is to achieve more precise understanding of the age-hardening behavior in Al-Mg-Cu alloys which lie in (α+S+T) phase field, with particular attention to the rapid age-hardening during the initial decomposition stage. The effects of aging temperature, alloy compositions and addition of Ag on the age-hardening behavior of Al-Mg-Cu alloys will be investigated by a combination of several kinds of experimental techniques.

1.2 Introduction to Aluminum Alloys

Pure Aluminum is relatively soft and it has limited applications. To overcome this, the material can be alloyed with other elements. Most of the aluminum reaching the marketplace has been alloyed with at least one other element. Such alloying elements can add enhanced properties to the base aluminum such as corrosion resistance, formability, strength, and/or other beneficial properties, in a wide range of permutations and combinations.

1.2.1 Aluminum Alloy Designations

Wrought aluminum alloys are commonly classified into eight types with a 4-digit designation. The first digit designates purity or alloy type. The second digit indicates modifications of the

alloy. Only in 1xxx series the third and fourth digits indicate the purity. For example, 1050 indicates an aluminum with 99.50% purity. The third and fourth digits in the other series identify different alloys in the group and have no numerical importance. **Table 1.1** shows the alloy designations based on the classification. Those series are fall into two categories; non-heat-treatable and heat-treatable.

Non-Heat-Treatable Alloys The initial strength of alloys in this group depends upon the hardening effect of elements such as manganese, silicon, iron and magnesium. The non-heat-treatable alloys are usually designated in the 1xxx, 3xxx, 4xxx, or 5xxx series. These alloys rely mainly on work hardening for property development.

Heat-Treatable Alloys The initial strength of alloys in this group is enhanced by the addition of alloying elements such as copper, magnesium, zinc, and silicon. These elements in various combinations show increasing solid solubility in aluminum with increasing temperature. Thus, it is possible to subject them to thermal treatments that will impart the pronounced strengthening.

Table 1.1 Wrought aluminum alloys in the international designation system.

Alloy series	Principal Alloying Element
1xxx	Aluminum (99.000 % minimum)
2xxx	Copper
3xxx	Manganese
4xxx	Silicon
5xxx	Magnesium
6xxx	Magnesium and Silicon
7xxx	Zinc
8xxx	Other elements

1.2.2 Basics of Strengthening Mechanisms

Like all metals, aluminum has a crystalline structure. Atoms are arranged in crystals in a three-dimensional lattice. Aluminum alloys are always polycrystalline, consisting of many

grains with different orientations. The size of the individual grains is varied from several millimeters to thousandth of a millimeter. Grain boundaries are described as planar defects leading to strength. Deformation can induce some defects in the crystal lattice - so-called "dislocations". A dislocation is a line defect. When a force is applied to a metal, these dislocations can move along appropriate slip planes, causing plastic deform of the metal. If dislocations are prevented from moving, the strength of the material is increased. This mechanism is the basis for the various methods of strengthening. Vacancies and substitutional solute atoms in solid solution can give strength as point defects. Precipitates also play an important role to impede the movements of dislocations. Several kinds of nano-scale defects are illustrated in **Fig. 1.2**. Various strengthening mechanisms are described below.

Work hardening Deformation at room temperature leads to the formation of new dislocations, which in turn makes further deformation more difficult; dislocations pile up at grain boundaries and there is an increase in strength.

Solid-solution strengthening This strengthening is caused by the interaction between strain field around solute atoms and dislocations. The alloying elements hinder the movements of dislocations and hence the strength increases.

Fine-grain hardening Grain refinement leads to an increase in the number of grain boundaries and more barriers to dislocation movement, results in an increase of strength.

Heat treatment By exposing a material to elevated temperatures, the structure and property of the material can be changed. With aluminum alloys, precipitation hardening is the most important process. “Age-hardening” is also used to designate this procedure. During age-hardening, lattice strains are established at the precipitate-matrix interface.

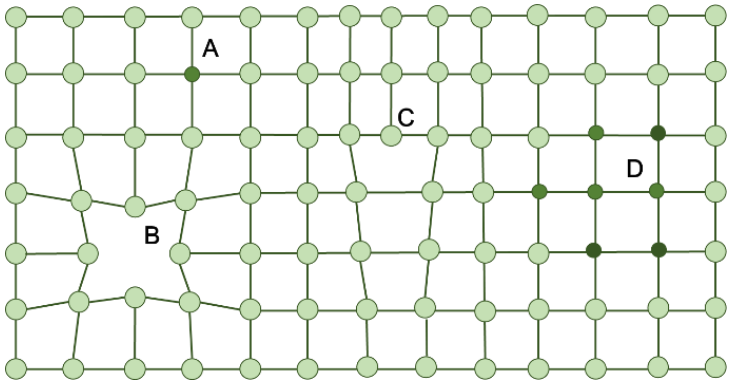

Fig. 1.2 Several kinds of nano-scale defects relevant for strengthening. A: Substitutional solute atom, B: Vacancy, C: Dislocation, D: Cluster of solute atoms.

1.2.3 Precipitation Hardening

Precipitation hardening (Age-hardening) is the process of strengthening of an alloy by precipitating finely dispersed precipitates of the solute atoms in a supersaturated matrix.

I. Steps in Precipitation Hardening Process

Three steps in precipitation hardening process are described as follows;

1. Solution treatment or homogenization During this step, an alloy is heated to a temperature, between the solvus and solidus temperatures at T1 in **Fig. 1.3 (a)** and soaked there until all of the solute dissolves into the α phase and a uniform solid solution structure is produced.

2. Quenching By quenching, the sample is cooled rapidly to a lower temperature from T1 to T2 in **Fig. 1.3 (a)**. The solute is supersaturated during quenching. The uniform solid solution structure of the alloy below the homogenization temperature is obtained.

3. Aging During aging treatment, the supersaturated solution is heated to an intermediate temperature at T3 in **Fig. 1.3 (a)** so as to induce precipitation and held at that temperature for a specific amount of time. When aging is conducted at room temperature, it is called natural aging. Aging above room temperature is called artificial aging. The whole precipitation process is described in **Fig. 1.3 (b)**.

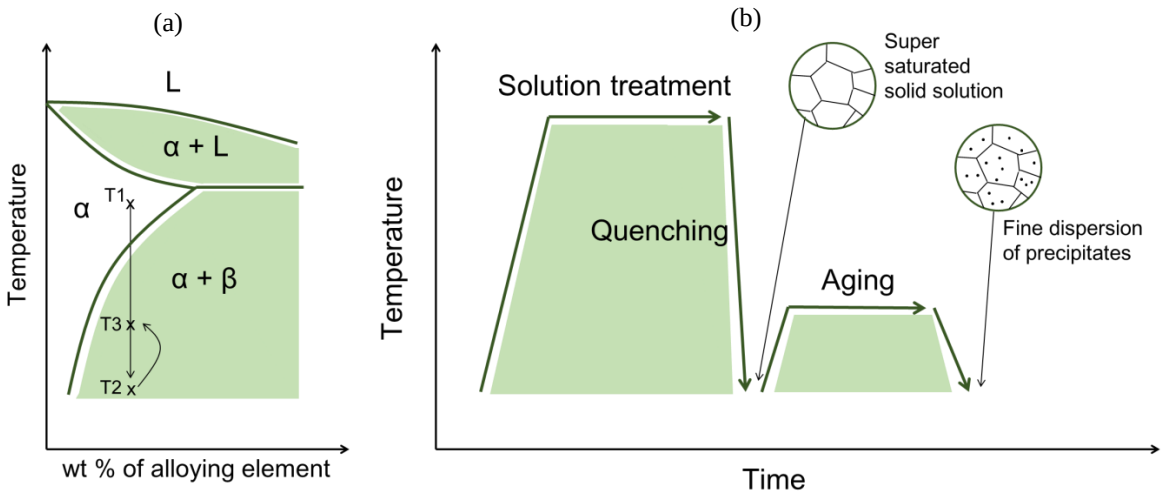

Fig. 1.3 (a) Steps in the age-hardening process. (b) An example of a phase diagram for binary aluminum alloys.

II. Decomposition of Super-saturated Solid Solution in Aluminum Alloys

As described before, age-hardenable aluminum alloys are solution-treated at a temperature high enough to dissolve the alloying elements into a random solid solution, then quenched in order to create a supersaturated solid solution (SSSS) having a random distribution of solutes [31]. Quenching is often followed by natural aging and/or artificial aging. During aging the supersaturated solid solution will decompose. This decomposition often follows a sequence as follows [31],

SSSS→ clusters→ Guinier-Preston (GP) zones→ metastable precipitates→ equilibrium precipitates

This sequence is observed in 2xxx, 6xxx and 7xxx series of aluminum alloys [32-34]. Solute clustering is observed widely in many Al alloys prior to the precipitation of GP zones, and these clusters have great effects on both the nature and kinetics of the precipitation process. The term "GP zones" was used for the first time to coherent aggregates of Cu atoms that were observed in Al-Cu alloys using X-Ray scattering techniques by Guinier [35] and Preston [36] in 1938 independently. GP zones are generally regarded as fully coherent metastable precipitates. Subsequent evolution of the microstructure involves the replacement of the GP zones with more stable phases.

1.2.4 Solute Clustering

The term "clusters" is used to describe regions of the matrix richer in solute than the nominal composition. Usually clusters contain the order of 100 atoms or less [37]. In the literatures, the term clusters is often used without precise definition and there is no clear distinction between solute clusters and GP zones. Usually, it is defined that clusters are solute atoms aggregated together without a definite structures, whereas GP zones possess a definite structure. By using atom probe tomography (APT), Komiya et al. investigated the shape and concentration of solute clusters in the early stage of aging for an Al-Zn alloy and distinguished between solute clusters and GP zones (**Fig. 1.4**) [38].

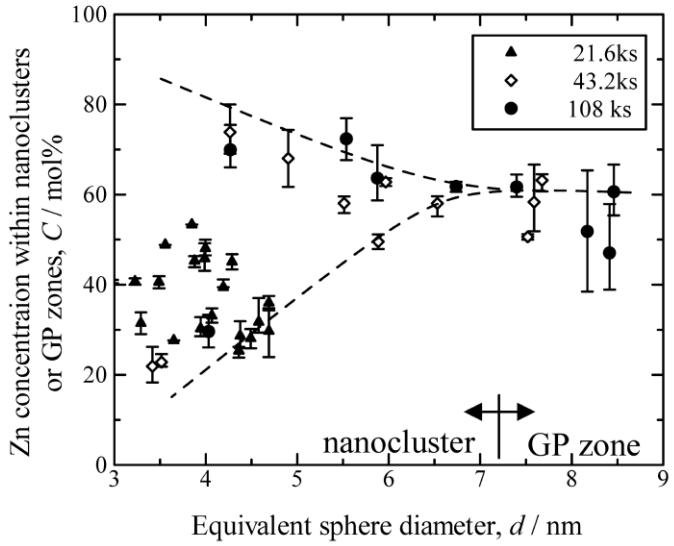

Fig. 1.4 Size dependence of Zn concentration within nanoclusters or GP zones in the Al-4.9mol%Zn alloy aged at 293 K for 21.6 ks, 43.2 ks and 108 ks.

I. Formation of Solute Clusters

In Al-Mg based alloys, the formation rate of clusters is low during both natural and artificial agings [39]. In binary Al-Cu alloys, Somoza et al. reported that vacancy-Cu pairs are presented immediately after quenching by using positron annihilation spectroscopy (PAS) measurement [40]. The vacancies are gradually released during aging at low temperatures with the formation of Cu clusters or GP zones. However, when both Mg and Cu are used as

alloying elements, i.e. in Al-Cu-Mg alloys, the formation of clusters is faster than that of Al-Mg and Al-Cu alloys. Rapid solute aggregation seems to occur in Al-Cu-Mg alloys [9]. The rate of cluster formation has been considered to be dominated by the concentration of vacancies that control the rate of diffusion of solute atoms from the matrix to the clusters [41]. For example, when Sn is added to Al-Cu alloys, the growth rate of Cu rich clusters in Al-Cu-Sn alloys becomes much slower than in Al-Cu alloys [42]. Due to stronger interactions of vacancies with Sn than with Cu, Cu clustering or GP zone formation was suppressed since the number of vacancies enabling Cu diffusion is reduced. This result was also proved by computer simulations by Hirosawa et al. [43]. In Al-Cu-Mg alloys, Mg stabilizes free volume in the form of vacancy complexes, possibly by co-clustering with Cu [26].

II. Relation Between Clustering and Strengthening

Many experimental studies have linked the presence of clusters to an increase of strength in Al-Cu [44], Al-Mg-Si [45], Al-Mg-Zn [46], and Al-Cu-Mg alloys [19]. Surprisingly, not all of the alloys exhibit strengthening with natural aging, for example binary Al-Zn alloys [47]. In Al-Zn alloys, clusters form during natural aging, however, there is no accompanying increase in hardness [47-49]. In fact, a decrease of hardness is seen at long aging times [47]. Chemical composition seems to play an important role in cluster strengthening. The origin of cluster strengthening especially for Al-Cu-Mg alloys will be described in next section.

III. Solute-vacancy Binding in Aluminum

Binding energy between vacancies and solute atoms is important for understanding diffusion [50, 51], however these bindings are quite difficult to measure accurately. For example, more than 20 values of Mg-vacancy binding energy have been reported in the literatures, ranging from extremely strong solute-vacancy binding energy of 0.4eV to a very weak but negative binding energy of -0.01 eV [50, 51]. For Cu-vacancy binding energy, the range of reported value is 0 to 0.4eV. There are similar trend for most of other solute elements. Recently,

Wolverton reported a large database of solute-vacancy binding energies determined from first-principles density functional calculations [52]. He found that Cu possess very weak binding energy. They also found that Mg possess even repulsive binding energy. In Al-Cu-Mg alloys, rapid age-hardening by rapid solute clustering (formation of vacancy-solute complexes) has been considered to be occurred after short time aging. In this regard, vacancy behavior during the initial decomposition stage has particular interest in Al-Cu-Mg alloys.

1.3 Age-hardening of Al-Cu-Mg Alloys

Age-hardening was first discovered in the alloy Al-3.5%Cu-0.5%Mg-0.5%Mn (wt %) by Wilm in 1906 [31]. Since then the Al-Cu-Mg system has been the basis for the 2000 series of high strength aluminum alloys which have compositions in the (α + S) phase field of the ternary phase diagram (**Fig. 1.5**) [53]. One of the characteristic features of these alloys is that, during aging at elevated temperatures (373-513 K), hardening occurs in two distinct stages separated by a plateau, where the hardness may remain constant for a long time. Schematic illustration for the age-hardening stages of an Al-Mg-Cu alloy is shown in **Fig. 1.6**. Another interesting feature is that the first stage of age-hardening occurs rapidly and complete after aging for only 60 s at 443 K. It contributes as much as 60% of the total hardening.

1.3.1 Precipitation Sequence and Age-hardening Stages

The strengthening of Al-Mg-Cu alloys is based on a precipitation hardening through the sequence as follows:

$$\alpha\ (SSSS) \rightarrow \text{Cu/Mg clusters} \rightarrow \text{GPB zones (S")} \rightarrow S' \rightarrow S$$

where SSSS is the super saturated solid solution. Cu/Mg clusters are considered as precursors of the GPB zones. The S" phase represents the Guinier-Preston-Bagaryatsky (GPB) zones, originally suggested by Bagaryatsky [54] to be a solute ordering structure formed on the

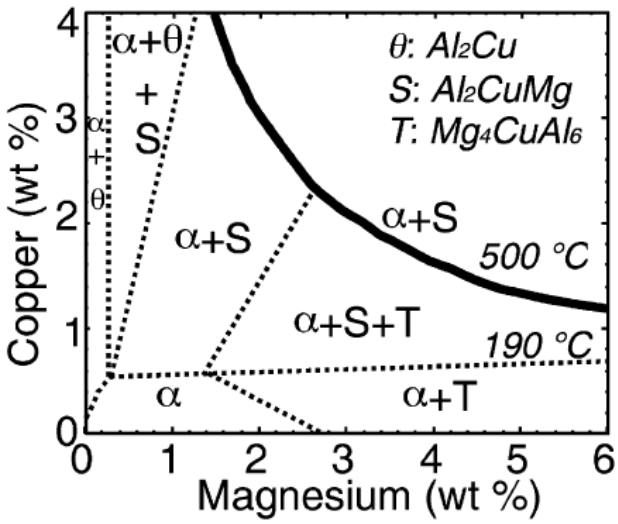

Fig. 1.5 Aluminum-rich corner of the Al-Cu-Mg phase diagram indicating the phases present as a function of composition, after long term ageing at 190 °C [53].

$\{001\}_{Al}$ planes and by Silcock [55] to be "agglomerated one-dimensional (1D) crystals" along $<100>_{Al}$ directions. Both descriptions can be said to be supported by recent studies in the atomic scale by high angle annual dark field scanning transmission electron microscopy (HAADF-STEM) and theoretical calculations.

The first increase in the age-hardening curve is now considered to be attributed to the solute clusters rather than to the formation of more structurally developed GPB zones [6, 7]. GPB zones and S' phase are considered to cause the second stage of hardening. S phase is the representation of the stable S' phase in the Al matrix. It has recently been verified that the S and S' phases are structurally similar, with composition Al_2CuMg [56, 57]. This is the same structure as suggested originally by Perlitz and Westgren [58]. In the following, this phase will be referred to as S'. According to several previous studies on Al-Mg-Cu alloys containing industrial levels of Mn, Fe and Si, T-phase has not been observed although the investigated alloys lie in (α+S+T) phase field [59, 60]. The T-phase is assumed to contain Cu instead of Zn, however with the same structure as the cubic T-Mg_{32} (Al, Zn)$_{49}$ [61, 62]. This phase can exist in commercial Al-Zn-Mg alloys of sufficient Mg-content [63].

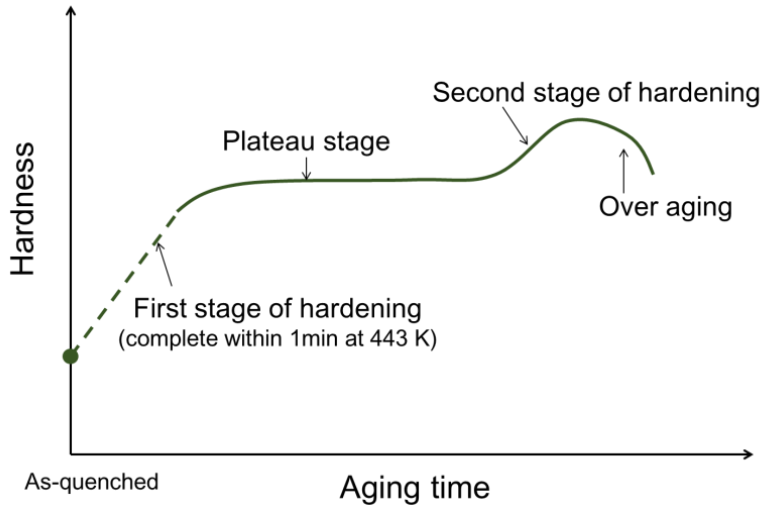

Fig. 1.6 Schematic illustration for the age-hardening stages in an Al-Mg-Cu alloy.

1.3.2 History of Rapid Age-hardening

The origin of the rapid age-hardening response in the Al-Cu-Mg system has attracted considerable research interest and various experimental techniques have been applied to reveal the mechanisms. Several mechanisms have been proposed as shown in **Fig. 1.7**. Following Silcock (1961) [55], it was widely accepted that the rapid age-hardening was attributed to the formation of fully-coherent GPB zones, and the second stage of hardening was associated with the precipitation of the S phase. In 1997, Ringer et al. [6] discovered the pre-precipitate atomic co-clusters of Cu and Mg by using atom probe together with field ion microscopy technique. Those clusters contained 3-20 atoms and were related to the onset of the rapid age-hardening reaction. An interaction between these clusters and moving dislocations during deformation was proposed as a new mechanism of hardening which was termed *cluster hardening*. Ringer et al. also demonstrated that GPB zones does not formed during the rapid age-hardening reaction. They concluded that the second stage of hardening is related to a fine and uniform dispersion of GPB zones and S phase has a relatively minor contribution to strengthening. In 1999, Reich et al. [10] could not identify solute clusters by

atom probe tomography, however they observed further hardening in an initially aged specimen which was re-aged after deformation. Thus, they proposed that the rapid age-hardening was attributed to the segregation of solute to the existing dislocations formed during quenching. It caused a dislocation-solute locking interaction. Starink et al. [13, 14] reported that a dislocation-solute interaction mechanism is not acceptable at room temperature aging. Alternatively, a modulus hardening mechanism was suggested based on the shear modulus difference between co-clusters of Cu and Mg and the Al matrix. According to the results obtained by differential scanning calorimetry (DSC) measurements, Zahra et al. [16] proposed that GPB zones nucleate on Cu–Mg co-clusters are responsible for the rapid age-hardening. Kovarik et al. [64-66] investigated the formation of GPB zones by HRTEM techniques for an Al-Cu-Mg alloy with very low Cu:Mg ratio aged at 453 K. With the aid of ab initio calculations, GPB zones show very favorable enthalpy of formation from the solid solution. They concluded that GPB zones cause the rapid age-hardening. Recently, Marceau et al. [67] characterized the clustering behavior in Al–1.1Cu–xMg alloys ($0.2 < x < 1.7$), during aging at 423 K by using quantitative atom probe tomography in combination with positron annihilation spectroscopy. They proposed that not all solute clusters have the same hardening effect but Cu/Mg clusters with a high Mg:Cu ratio (> ~ 2) and sized > ~ 3-10 atoms are the most potent strengthening agents.

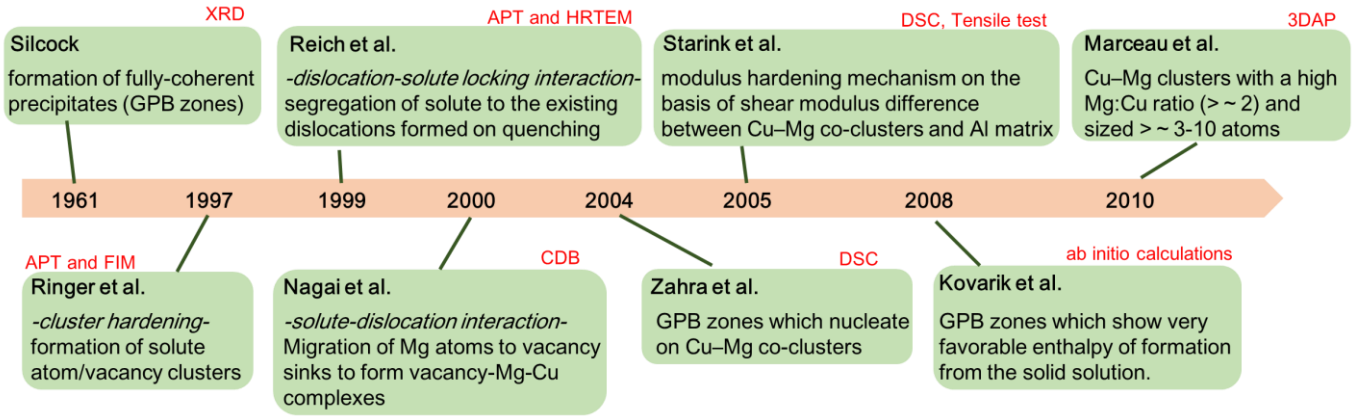

Fig. 1.7 History of research on rapid age-hardening phenomena in Al-Cu-Mg alloys.

1.3.3 Characteristic Effect of Ag Addition

The role of trace elements on the aging behavior of Al alloys has been extensively studied. It was found that the small amount of Ag addition can enhance the age-hardening response in aluminum alloys that contain magnesium. Each system behaves differently. In Al-Zn-Mg alloys aged, Ag stimulates the existing aging process and this effect is attributed to an increase in the aging temperature range over which GP zones are stable. In binary Al-Mg alloys, Ag may induce precipitation in alloys which is absent in the Al-Mg binary alloys. In the Al-Cu-Mg system, Ag addition promotes the formation of three new phases depending on the Cu/Mg ratio (**Table 1.2**) [74]. The addition of Ag to Al-Cu-Mg alloys with high Cu/Mg ratios (in the α + θ + S phase field) promotes the formation of Ω phase as finely dispersed plates on $\{111\}_{Al}$. Ag modifies the precipitation process from the initial decomposition through a preferred Mg-Ag interaction [5, 68]. Sano et al. [69, 70] revealed that the Ω phase has the same Cu concentration as the θ (Al_2Cu) phase with only difference in segregation of Ag and Mg at the Ω/matrix interfaces, and this suggests that both Ω and θ are chemically equivalent. The addition of Ag to Al-Cu-Mg alloys with medium Cu/Mg ratios (in the α+ S phase field) stimulates the formation of X' phase as fine platelets on $\{111\}_{Al}$ [71]. Contrary to the Ω phase, Ag is contained inside the X' precipitate. Since Mg and Ag has the strong interaction, it is expected that Ag accompanies Mg into the X' phase during nucleation and growth. Ag atoms may substitute for Al atoms because of their similar atomic sizes. It has been proposed that the addition of Ag to Al-Cu-Mg alloys with low Cu/Mg ratios (in the α+ S + T phase field) promotes the precipitation of a finely distributed metastable T phase in Al-Cu-Mg alloys with low Mg/Cu ratio . However, the existence of the T phase was based only on the visual observations of X-ray intensities which shows similarity to the T phase observed in the Al-Zn-Mg system. Chopra et al. [72] re-examined an Al-1.5Cu-4Mg-0.5Ag (wt %) alloy which lie in (α+S+T) phase field and clarified that the obtained precipitates on

{111}$_{Al}$ which possesses a cubic structure were not isomorph of the T phase [21, 72, 73]. The precipitates were newly designated as Z phase. Ag is contained inside the Z precipitate.

Table 1.2 Details of precipitates formed by the addition of Ag to aged ternary Al-Cu-Mg alloys [74].

Cu / Mg ratio	Precipitate	Crystal Structure	
High: e.g. Al-4Cu-0.3Mg	Ω	orthorohombic	a = 0.496 nm b = 0.859 nm c = 0.848 nm
Medium: e.g. Al-2.5Cu-1.5Mg	X'	c.p. hexagonal	a = 0.496 nm c = 1.375 nm
Low: e.g. Al-1.5Cu-4.0Mg	Z	Cubic	a = 1.999 nm

1.4 Experimental Evidence of Clustering and Vacancy Behavior in Aluminum Alloys

1.4.1 Electrical Resistivity Measurement

Electrical resistivity measurement has been frequently applied to investigate the progress of precipitation phenomena in an alloy. The electrical resistivity depends on the number and the distribution of point defects, dislocations, vacancies, and solute atoms [75]. Due to the low concentration of vacancies compared to that of solute atoms in alloys, the change of electrical resistivity is very sensitive to solute clustering events. As the supersaturated solid solution decomposes and starts forming solute clusters, the electrical resistivity increases. The increase of resistivity is due to a higher scattering of electrons because of the non-random character of the distribution of solute atoms. The following decrease of resistivity occurs as the precipitation proceeds.

1.4.2 Differential Scanning Calorimetry (DSC) Measurement

DSC have been applied extensively to the analysis of light metals, especially Al based alloys. DSC is an indirect characterization technique with respect to obtaining quantitative structural

information. DSC technique can monitor the difference of heat flux required to increase the temperature of a sample compared to a reference sample. In aged aluminum alloys, the exothermal peaks which appear in the DSC curves correspond to the formation of phases. The endothermal peaks correspond to the dissolution of phases. For the Al-Cu-Mg alloys which shows rapid age-hardening, it is known that an exothermal peak appears during DSC scan of quenched Al-Cu-Mg alloys. One example of a hardness and DSC results obtained for an Al-4.4 wt% Cu- 1.7 wt% Mg alloy is shown in **Fig. 1.8** [76]. This reaction is important as it is the cause of the rapid age-hardening. Various terms to identify the structures formed in this exothermal peak reaction have been made (GP or GPB zones clusters) [77, 78]. However most of them achieved without conclusive microstructural evidence. DSC work supported by further microstructural observations such as electron microscopy or atom probe is needed.

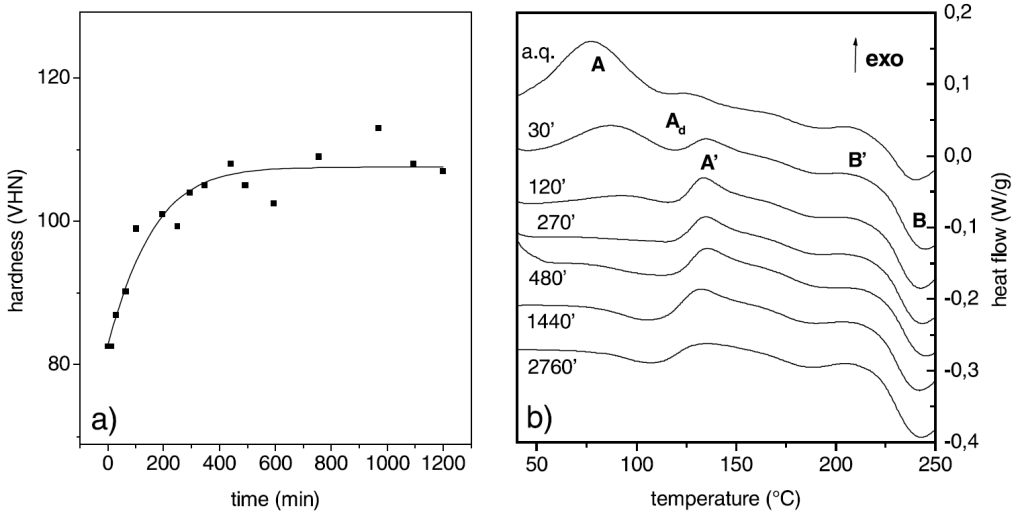

Fig. 1.8 (a) Hardness trend as a function of the annealing time at room temperature for the a.q. sample; (b) DSC traces on a.q. and on samples aged at room temperature for the indicated times (scanning rate: 20 K/ min) [76].

1.4.3 Atom Probe Tomography (APT)

Three dimensional APT can resolve both the three-dimensional position and chemical identity of individual atoms. The sample for APT is prepared in the form of a very sharp tip. The very small radius of the tip and the high voltage induce a very high electrostatic field at

the tip surface. Under laser or HV pulsing, atoms are evaporated from the surface by field effect (near 100% ionization), and projected onto a detector as shown in **Fig. 1.9**. Since ions are specified from flight time which is decided by weight of each ions, the time of flight of the ions and the position of the ions impact on the detector are obtained to reconstruct a 3D image of the material at the atomic scale. APT has been applied to study the initial decomposition stages in many alloy systems including Al-Cu-Mg alloys [79]. In order to investigate the density and composition of clusters from APT data, the maximum separation method has been widely used. However, the measured value of cluster density depends on the parameters selected and is subject to significant errors due to the limited number of clusters detected in any one analysis [80]. To address these problems, Marceau et al. applied a new cluster-finding algorithm to much larger APT data sets than previously available to obtain comprehensive microstructural information [67]. However, the conclusion from APT analysis are still open to debate. Kovarik and Mills argued that it has yet to be shown whether the nominal composition of the potent strengthening clusters is biased by the presence of Mg-Cu clusters with an extremely high Mg/Cu ratio that do not have a potent strengthening effect [66]. In addition, APT has its physical limitation at this size scale. The detection efficiency and a limited lateral resolution should also be noted.

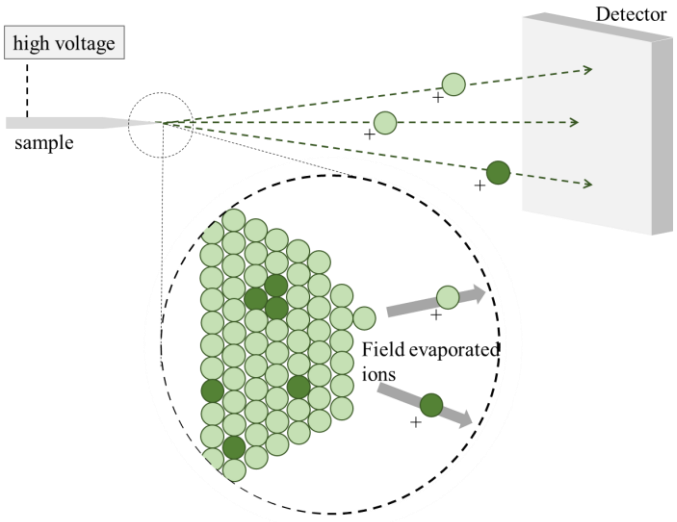

Fig. 1.9 Schematic illustration of APT.

1.4.4 Positron Annihilation Spectroscopy (PAS)

PAS is a non-destructive spectroscopy technique that allows studying a variety of phenomena and material properties on an atomic scale [81]. PAS is the spectroscopy of the photons coming out from annihilation of positrons and electrons. Positrons implanted in a metal will diffuse through the lattice and reach the thermal equilibrium in a few picoseconds. Positrons are repelled by electrostatic forces away from positive metal ions. Thus, any open-volume available in the lattice (a vacancy, a void, a lattice irregularity near to a dislocation or next to an incoherent interface) appears as a potential energy minimum for a positron. The result of the positron-electron reaction is annihilation. Both particles disappear and their mass $2m_0$ is converted in electromagnetic energy $E = 2m_0c^2$. Two photons emission is the most likely annihilation channel in a metal (**Fig. 1.10**). The two photons are not exactly anti-parallel. Thus, they are shifted by opposite amounts due to the Doppler effect. This energy shift appears as a broadening of the annihilation line. The time interval between the injection of a positron into a sample and the instant of annihilation is called positron lifetime.

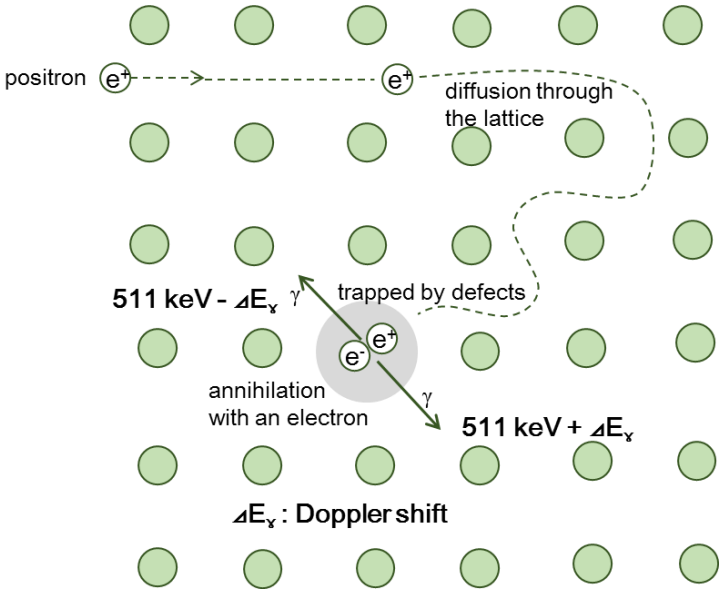

Fig. 1.10 Schematic illustration for the positron annihilation reaction in a metal.

The two main experimental techniques of PAS are positron annihilation lifetime spectroscopy (PALS) and coincidence Doppler broadening (CDB). PALS provides a most sensitive and specific tool for vacancy detection and identification [82]. In defect-free pure Al, the lifetime spectrum is a simple decaying exponentials and the mean positron lifetime is about 160 ps. With monovacancies in Al, the lifetime becomes about 240 ps. The lifetime spectra is sensitive to the chemistry of the samples and to the presence of defects.

PALS can follow the decomposition of a supersaturated solid solution (SSSS) by measuring in situ the annihilation reactions. **Figure 1.11** shows the evolution of positron lifetime during natural aging for Al-1.1Cu and Al-1.1Cu-0.5Mg (at %) alloys [83]. A monotonic decrease of positron lifetime was observed during natural aging of both alloys after solution treatment. This evolution of positron lifetime is consistent with progressive formation of vacancy-Cu clusters [84]. The lifetime curve for Al-1.1Cu alloy tends to approach that of vacancies in pure Cu, indicating that vacancies are included in three-dimensional Cu clusters.

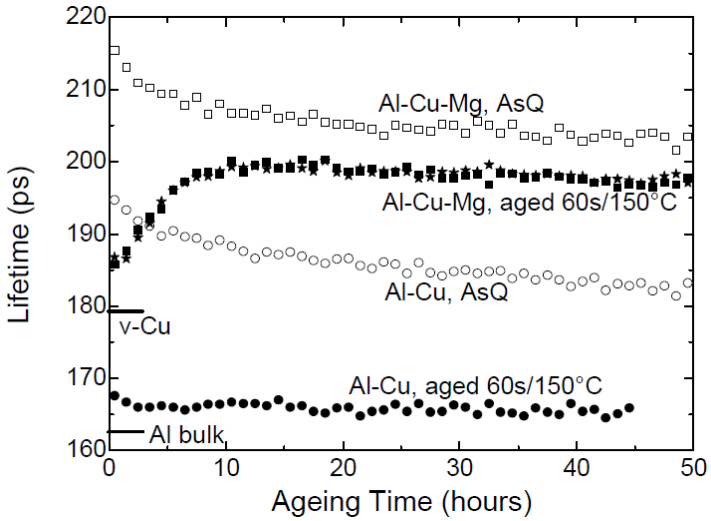

Fig. 1.11 PALS results. Open symbols refer to natural aging after solution treatment and quenching. Solid symbols refer to natural ageing after solution treatment, quenching, aging for 60 sec at 150 °C and quenching. Circles: Al-1.1 Cu, squares and stars: Al-1.1Cu-0.5Mg (at %) alloys [83].

After aging at 150 °C for 60 sec, the lifetime curve for Al-1.1Cu alloy runs very closely to the value expected for bulk Al, suggesting a substantial reduction in residual vacancy supersaturation. On the other hand, the lifetime curve for Al-1.1Cu-0.5Mg alloy increases significantly during natural aging after initial aging at150 °C for 60 sec. It indicates that Mg stabilizes free volume in the form of vacancy complexes, possibly by co-clustering with Cu. The lifetime variations during aging reflect the changing of the chemical environment of the vacancies. **Figure 1.12 (a)** shows the CDB data for Al-4Cu and Al-4Cu-0.3Mg (wt %) alloys at various stage of aging [40]. The longitudinal component p_L of the positron-electron momentum along the direction of emission of one of the annihilation photons is attributed to the Doppler shift $\Delta E = p_L c/2$ in the photon energy. The result shows a broadening of the annihilation line since p_L is a random variable symmetrically distributed around zero. In the A.Q. state in **Fig. 1.12 (a)**, localization peaks at the $p_L = \pm 1.3$ atomic units (a.u.) are appeared due to the positron confinement in an atomic-size open volume (most provably, vacancies). For Al-4Cu (wt %) alloy, the Cu characteristic signal (the structure peaked around ±2 atomic units) becomes weaker during aging, indicating that the number of vacancy-Cu complexes, where positrons can be trapped, decreases in concomitance with the growth of GP zones. On the other hands, for the ternary alloy (Al-4Cu-0.3Mg (wt %) alloy), a Cu signal becomes stronger as aging proceeds. It indicates that all positrons are trapped by vacancy-Cu complexes that become richer in Cu. Finally, all surviving vacancies are included into GP zones. The intensity of the Cu signal is correlated with the number of Cu atoms surrounding the vacancies. **Figure 1.12 (b)** shows the reference momentum spectra [40]. These spectra are obtained under the condition of saturated positron trapping. CDB curves for alloys can be very accurately fitted by linear combinations of those reference curves. The main contribution to p_L comes from the electron motion. Thus, the shape of the "wings", broadened annihilation line is the "fingerprint" of the annihilation with alloy components, which can be used for

evaluating the relative contribution of alloy components to annihilation in an alloy. By using PAS techniques, valuable information about the role of vacancies during precipitation process can be obtained. Particularly, it is important to investigate the vacancy behavior during the initial decomposition stage where vacancy-solute aggregates are formed.

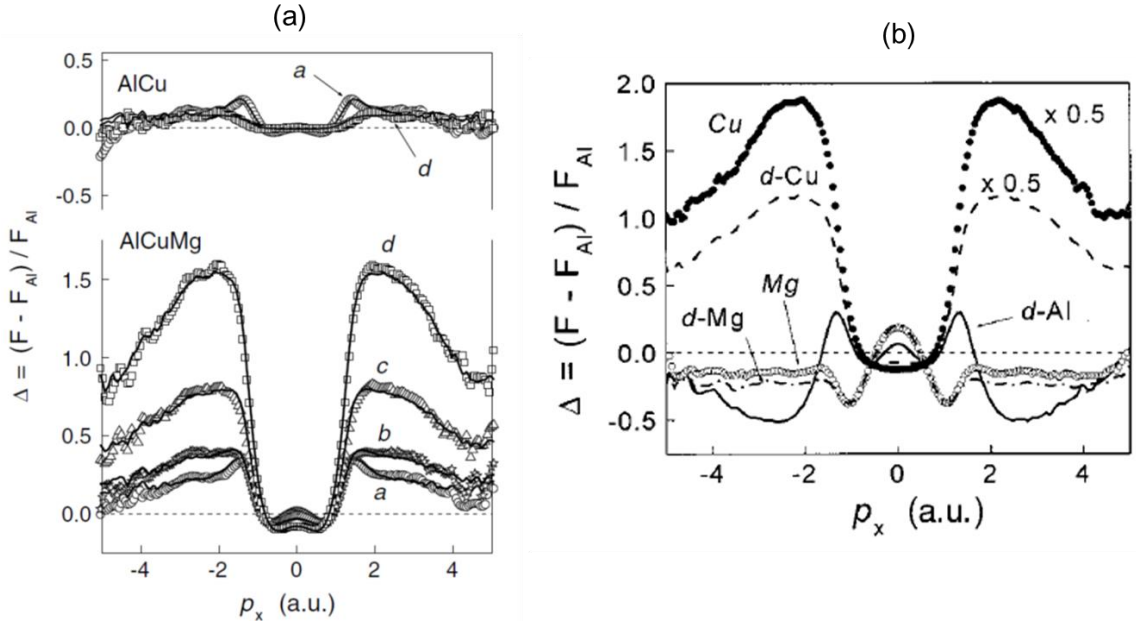

Fig. 1.12 (a) CDB data for Al-Cu and Al-Cu-Mg at a: as-quenched (supersaturated solid solution), b: initial aging (3.5 days/RT), c: intermediate aging (25 days/RT), and d: advanced aging (25 days/69 °C). The solid lines are the result of a linear fitting. (b) CDB data for defect-free Cu (solid circles), defect-free Mg (open circles), deformed Al (d-Al, solid line), deformed Cu (d-Cu, dashed line), deformed Mg (d-Mg, dash-dotted line). The horizontal line at ⊿=0 corresponds to the reference (defect-free Al) [40].

1.4.5 High-angle Annular Dark Field STEM (HAADF–STEM)

The scanning transmission electron microscope (STEM) works on the same principle as the normal scanning electron microscope (SEM), by forming a focused beam of electrons that is scanned over the sample while some desired signal is collected to form an image [85]. The difference with SEM is that thin specimens are used so that transmission modes of imaging are also available. STEM observation contains two types of methods of a bright-field (BF)

STEM image and a dark-field (DF) STEM image. The BF-STEM technique uses an electron beam passing through the sample. The DF-STEM technique uses an electron beam scattered from the sample. The HAADF (high-angle scattering annular dark field) is an imaging method which uses an annular detector to detect transmission electrons scattered at a high angle [**Fig. 1.13 (a)**]. Unlike the HRTEM images, the HAADF-STEM image is formed by incoherent electron waves. The fraction of electrons which are high-angle scattered depends strongly on the atomic number (Z) of the elements contained in the specimen. There is an approximate power-law relation between the intensity I and the atomic number Z:

$$I \propto Z^{\alpha}$$

Pure Rutherford scattering predicts $\alpha = 2$, but the addition of thermal diffuse scattering and the imaging conditions in HAADF–STEM yields $\alpha = 1.3\text{-}1.8$, depending on the specimen thickness and the thermal vibrations of each element, amongst other things [86]. An element having large atomic number is scattered at a higher angle [**Fig. 1.13 (b)**] and seen brightly in the HAADF-STEM images. Thus, the contrast of HAADF-STEM images can be simply interpreted by the atomic number differences, so-called "z-contrast" [86]. With state of the art STEM instruments, even single atoms or small clusters consisting of few atoms can be resolved [87]. HAADF-STEM imaging can distinguish solute clusters and GP zones [88] as shown in **Fig. 1.14**. The images directly reflect the distributions of heavier constituent, Cu atoms which shows a bright contrast.

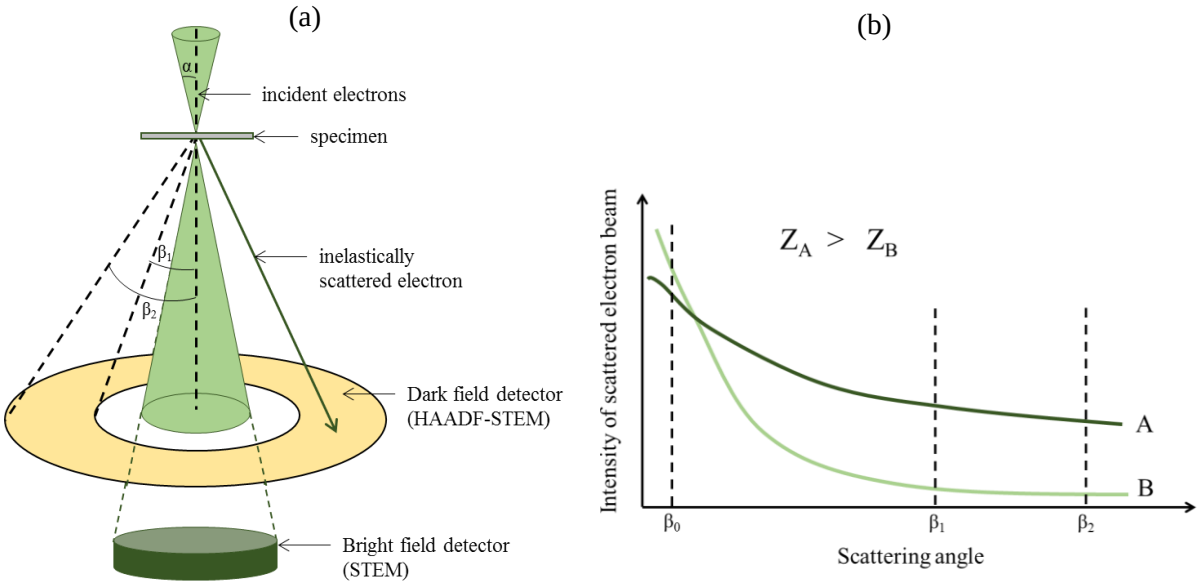

Fig. 1.13 (a) Schematic illustration of the STEM showing the geometry of the annular dark-field detector, and the bright-field detector for phase-contrast imaging. (b) Relationship between the intensity of scattered electron beam and scattering angle. Z_A and Z_B is atomic number of atom A and B, respectively.

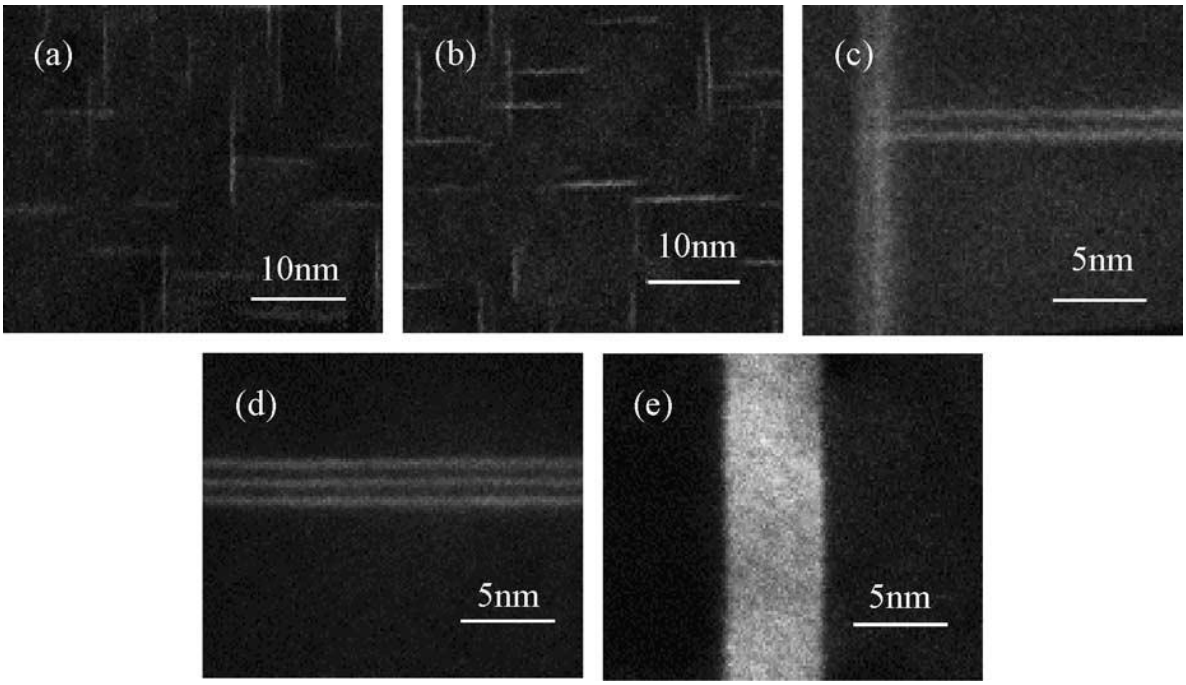

Fig. 1.14 HRTEM images obtained from an Al-1.94 Cu (at %) aged at 403 K for (a) 6.0 $\times 10^2$ s, (b) 6.0×10^4 s, (c) 3.0×10^6 s, (d) 1.8×10^7 s and (e) 3.6×10^7 s, respectively [86].

1.5 Objectives of Present Thesis

The present thesis aims to achieve a more precise understanding of the age-hardening behavior in Al-Mg-Cu alloys which lie in (α+S+T) phase field, with particular attention to the rapid age-hardening during the initial decomposition stage.

As described in the previous sections, the rapid age-hardening is related to the evolution of nanostructures. Quenched-in vacancies should also have an important role to form the nanostructure during the initial decomposition stage. Thus, several kinds of experimental techniques; hardness measurement, electrical resistivity measurement, differential scanning calorimetry (DSC), Transmission electron microscopy (TEM), three-dimensional atom probe tomography (3DAP) and positron annihilation spectroscopy (PAS) will be applied to investigate the rapid age-hardening behavior of Al-Mg-Cu alloys.

In addition to the Base alloy (Al-3Mg-1Cu (wt %)), alloys with different Cu/Mg compositions in (α+S+T) phase field will be used to make further understanding of the roles of Cu and Mg atoms during initial decomposition stage by using mainly PALS technique.

As described in the previous sections, microalloying of Ag has an great effect on the age-hardening response and microstructure of the ternary Al-Mg-Cu alloys. The effect of Ag addition on the evolution of nanostructure and will be investigated by mainly TEM and PAS technique. In addition, especially for the base Al-Mg-Cu and Ag-added alloys, microstructure evolution during aging for long time will be also investigated by using TEM technique.

1.6 Outline of Present Thesis

The schematic outline of the present thesis is shown in **Fig. 1.15**. The outlines of the present thesis are briefly summarized as follows.

Chapter 1 is ***"General Introduction"***. This chapter describes the backgrounds, basics of the strengthening mechanism of aluminum alloys, the characteristic age-hardening behavior of Al-Cu-Mg based alloys and the importance of the study on solute clustering and vacancy behavior. The objective of the present thesis is described based on the former introduction.

Characteristic age-hardening behavior of Al-3Mg-1Cu alloys which lie in (α+S+T) phase field is investigated in **Chapter 2** ***" Characteristic Age-hardening Behavior of Al-Mg-Cu Alloys"***. Rapid age-hardening response after short time aging as well as the formation of three types of precipitates after long time aging are discussed.

The evolution of nanostructure in the initial stage of aging is investigated in **Chapter 3** ***"Evolution of Nanostructures and Role of Vacancies During Initial Stage of Aging in an Al-Mg-Cu Alloy"***. Various techniques such as high-angle annular dark field STEM (HAADF-STEM), three dimensional atom probe tomography (3DAP), and positron annihilation spectroscopy (PAS) are applied to identify and characterize the nanostructures which form during initial stage of aging. Such nanostructures are responsible for the rapid age-hardening.

Age-hardening response of Al-Mg-Cu alloys with different Cu, Mg compositions which lie in (α+S+T) phase field is investigated in **Chapter 4** ***"Effect of Different Cu, Mg Compositions on Age-hardening Behavior in an Al-Mg-Cu Alloy"***. The role of Cu, Mg atoms and vacancy during the initial decomposition is discussed based on the results obtained by PALS technique. In addition,

The effect of Ag addition on the age-hardening response is investigated in **Chapter 5** ***"Effect of Small Addition of Ag on Age-hardening Behavior in an Al-Mg-Cu Alloy"***. The improvement of the rapid age-hardening response by Ag addition is discussed in terms of the roles of Ag atoms and vacancies in the evolution of nanostructures.

Finally, the overall results are summarized in **Chapter 6** ***"General Conclusions"***.

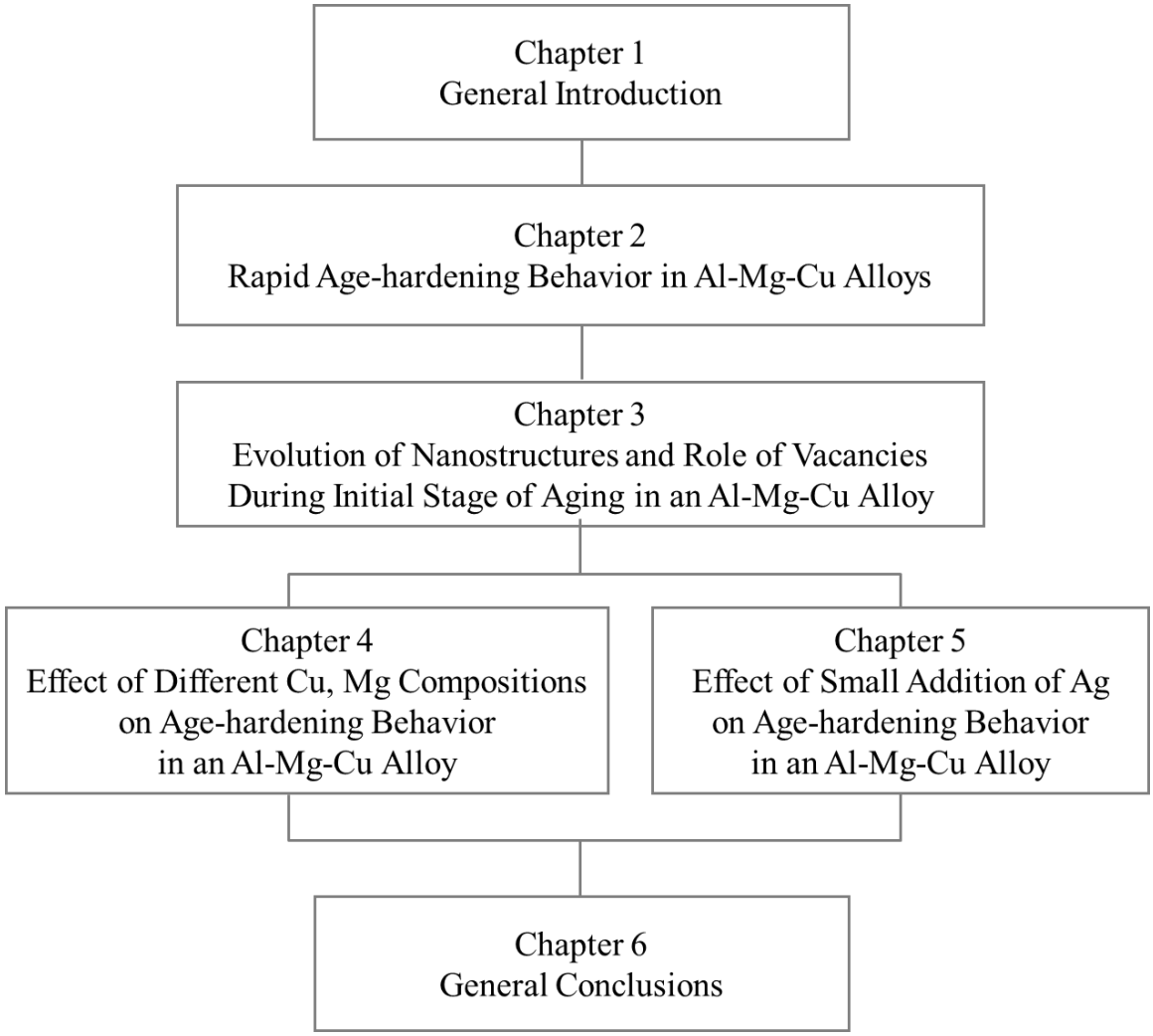

Fig. 1.15 Schematic outline of the present thesis.

References

1) U.S. Geological Survey, 2015, Aluminum; World mine production, by country, in Matos, G.R., comp., Historical global statistics for mineral and material commodities (2015 version): U.S. Geological Survey Data Series 896, 4 p., accessed March 2, 2015, at http://dx.doi.org/10.3133/ds896

2) Norsk Hydro ASA. (2013). Aluminium in transportation, Retrieved from http://www.hydro.com/en/About-aluminium/Benefits/Transportation/

3) P. Ratchev, B. Verlinden, P. Van Houtte, Scripta Metall. Mater. 30 (1994) 599.

4) P. Ratchev, B. Verlinden, P. De Smet, P. Van Houtte, Acta Mater. 46 (10) (1998) 3523.

5) S.P. Ringer, K. Hono, I.J Polmear, T. Sakurai, Acta Mater 44 (1996) 1883-1898.

6) S.P. Ringer, S.P. Hono, T. Sakurai, I.J. Polmear, Scripta Mater. 36 (5) (1997) 517-521.

7) S.P. Ringer, T. Sakurai, I.J. Polmear, Acta Mater. 45 (10) (1997) 3731.

8) S.P. Ringer, S.K. Caraher, I.J. Polmear, Scripta Mater. 39 (1998) 1559–1567.

9) A.M. Zahra, C.Y. Zahra, C. Alfonso and A. Charai, Scr. Mater. 39 (1998) 1553-1558.

10) Reich L, S.P. Ringer, K. Hono, Philos Mag Lett 79 (1999) 639-648.

11) Y. Nagai, M. Murayama, Z. Tang, T. Nonaka, K. Hono, M. Hasegawa, Acta Mater 2001;49:913-920.

12) A.M. Zahra, C.Y. Zahra, Philosophical Magazine Letters 82 (2002) 9-12.

13) M.J. Starink, N. Gao, J. Yan, Materials Science and Engineering A 387 (2004) 222-226.

14) M.J. Starink, N. Gao, Davin L, J. Yan, A. Cerezo, Philosophical Magazine 85(13): (2005) 1395-1417.

15) S.C. Wang, M.J. Starink, International Materials Reviews 50 (2005) 193-215.

16) A.M. Zahra, C.Y. Zahra, B. Verlinden, Philosophical Magazine Letters 86 (2006) 235-242.

17) R.K.W. Marceau, R. Ferragut, A. Dupasquier, M.M. Iglesias, S. P. Ringer, Materials Science Forum, 519-521 (2006) 197-202.

18) R.K.W. Marceau Ph.D. thesis. The University of Sydney; 2008.

19) M. Starink and S. Wang, Acta Materialia, 57 (2009) 2376–2389.

20) P.I. Gouma, D.J. Lloyd, M.J. Mills, Materials Science and Engineering A319–321 (2001) 439–442.

21) S. Hirosawa, T. Omura, Y. Suzuki, T. Sato, Materials Science Forum 519-521 (2006) 215-220.

22) C. Macchi, A. Somoza, R. Ferragut, A. Dupasquier, and I. J. Polmear, Phys. Status Solidi C 6, 11 (2009) 2322–2325

23) C. Li, G. Sha, B. Gun, J.H. Xia, X.F. Liu, Y.Y. Wu, N. Birbilis and S.P. Ringer, Scripta Materialia 68 (2013) 857–860.

24) Zhiguo Chen, Jishuai Zhang, Jun Shu, Gang Sha, Junhai Xia, Shiyong Wang and S.P. Ringer, Philosophical Magazine Letters, 93 (2013) 648–654.

25) C. Macchi, A. Tolley, R. Giovachini, I.J. Polmear, A. Somoza, Acta Materialia 98 (2015) 275–2.

26) H.K. Hardy, J Inst Metals, 82 (1953-54) 236-238.

27) I.J. Polmear, K.R. Sargant, Nature 200 (1963) 669-670.

28) I.J. Polmear, Trans. Met. Soc. AIME 230 (1964) 1331.

29) J.T. Vietz, I.J. Polmear, J. Inst. Met. 94 (1966) 410–419.

30) N. Sen, D.R.F. West, Monograph and Report Series, No. 33, Institute of Metals, London (1969).

31) I. J. Polmear, Light Alloys, Fourth Edition: From Traditional Alloys to Nanocrystals United Kingdom (2005).

32) S. Pogatscher, H. Antrekowitsch, H. Leitner, T. Ebner, and P. Uggowitzer, Acta Materialia, 59 (2011) 3352 –3363.

33) S. P. Ringer and K. Hono, Materials Characterization, 44 (2000) 101 –131.

34) H. Degischer, W. Lacom, A Zahra, and C. Zahra, Zeitschrift fur Metallkunde 71 (1980) 231–238.

35) A. Guinier, Nature 142 (1938) 569–570.

36) G. D. Preston, Nature 142 (1938) 570.

37) D Turnbull, H. S. Rosenbaum, and H. N. Treaftis, Acta Metallurgica, 8 (1960) 277-295.

38) Y. Komiya, S. Hirosawa and T. Sato, J. Jpn. Inst.Journal of Light Metals, 56 (2006), 662−666.

39) A. Kelly and R. B. Nicholson, 10 (1963) 151–391.

40) A.Somoza, M.P. Petkov and K.G. Lynn, Physical review B, 65 (2002) 094107.

41) L. Girifalco and H Herman, Acta Metallurgica 13 (1965) 583-590.

42) H. Kimura and R. Hasiguti, Acta Metallurgica 9 (1961) 1076 –1078.

43) S. Hirosawa, T. Sato, J. Yokota, and A. Kamio, Japan Institute of Metals, 39 (1998) 139–146.

44) H. W. Wiley, “Applications of chemistry to public welfare,” Journal of the Franklin Institute, vol. 171, no. 1, pp. 47 –54, 1911.

45) S. Esmaeili, D. J. Lloyd, and W. J. Poole, “Modeling of precipitation hardening for the naturally aged Al–Mg–Si–Cu alloy AA6111,” Acta Materialia, vol. 51, no. 12, pp. 3467 –3481, 2003.

46) A. Melander and P. A. Persson, “The strength of a precipitation hardened AlZnMg alloy,” Acta Metallurgica, vol. 26, no. 2, pp. 267 –278, 1978.

47) D. L. Douglass and T. W. Barbee, “Spinodal decomposition in Al–Zn alloys,” Journal of Materials Science, vol. 4, no. 2, pp. 121–129, 1969.

48) M. Hennion, D. Ronzaud, and P. Guyot, “Kinetics of unmixing in Al–Zn single crystals studied by neutron small angle scattering,” Acta Metallurgica, vol. 30, no. 2, pp. 599 –610, 1982.

49) N. Luiggi, J. P. Simon, and P. Guyot, “Residual resistivity during clustering in Al–Zn solid solutions,” Acta Metallurgica, vol. 28, no. 8, pp. 1115 –1122, 1980.

50) R.W. Balluffi, P.S. Ho, Diffusion metals park, Am Soc Metals, OH (1973), p. 83.

51) L.F. Mondolfo, Aluminum alloys: structure and properties, Butterworth, London (1976).

52) C. Wolverton, Acta Materialia, Volume 55, Issue 17, October 2007, Pages 5867–5872.

53) Brook GB. Precipitation in Metals, Special Report No. 3. Fulmer Research Institute: UK, 1963.

54) Y.A. Bagaryatsky, Dokl. Akad. SSSR87(1952)397–401.

55) J.M. Silcock, J.Inst.Met.89 (1960-61) 203–210.

56) B. Heying, R.-D.Hoffmann, R.Pöttgen, Z. Naturforsch. 60B (2005)491–494.

57) Z.R. Liu, J.H. Chen, S.B. Wang, D.W. Yuan, M.J. Yin, C.L. Wu, Acta Mater. 59 (2011)7396–7405.

58) H. Perlitz, A.Westgren, Ark. Kemi Mineral Geol.16B (1943) 1–5.

59) P. Ratchev, B.Verlinden, P. van Houtte, Scr.Met.Mater. 30 (1994) 599–604.

60) S. Hirosawa, T. Omura, Y. Suzuki, T. Sato, J. Jpn. Inst. Light Met.56 (2006) 673–679.

61) J.H. Auld,J.T. Vietz, I.J. Polmear, Nature 209(1966)703–704.

62) G. Bergman, J.L.T. Waugh, L. Pauling, Acta Cryst.10 (1957) 254–259.

63) X. -M.Li, M.J. Starink, Mater. Sci. Technol.17 (2001) 1324–1328.

64) L. Kovarik, S.A. Court, H.L. Fraser, M.J. Mills, Acta Mater. 56 (2008) 4804–4815.

65) L. Kovarik, M.J. Mills, Scr. Mater. 64 (2011) 999–1002.

66) L. Kovarik, M.J. Mills, Acta Mater. 60 (2012) 3861–3872.

67) R.K.W. Marceau, G. Sha, R. Ferragut , A. Dupasquier, S.P. Ringer, Acta Materialia 58 (2010) 4923–4939.

68) K. Hono, T. Sakurai, and I. J. Pomear, Scripta Metall. Mater. 30:695–700 (1994).

69) N. Sano, K. Hono, T. Sakurai, and K. Hirano, Scripta Metall. Mater. 25, 491 (1991).

70) K. Hono, N. Sano, S.S. Babu, R. Okano and T. Sakurai, Acta metall. mater. 41, 829 (1993).

71) H.D. Chopra, K.J. Liu, B.C. Muddle and I.J. Polmear, Philos. Mag. Lett. 71 (1995) 319-324.

72) H. D. Chopra, B. C. Muddle, and I. J. Polmear, Philos. Mag. Lett. 73 (1996) 351-357.

73) S.P. Ringer, Q.C. Quan, T. Sakurai, Mater. Sci. Eng. A 250 (1998) 120.

74) I. J. Polmear, Light Alloys, 4th ed, Elsevier / Butterworth-Heinemann, Amsterdam (2006).

75) A. Kelly and R. B. Nicholson, 10 (1963) 151–391.

76) S. Abis, M. Massazza, P. Mengucci and G. Riontino, Scripta Materialia 45 (2001) 685-691.

77) A.K. Jena, A.K. Gupta and M.C. Chaturvedi, Acta metall. 37 885 (1989).

78) A. Luo, D.J. Lloyd, A. Gupta and W.V. Youdelis, Acta metall. 41 769 (1993).

79) M.K. Miller, Atom probe tomography: Analysis at the atomic level. New York. Kluwer Academic/Plenum Publisher (2000).

80) D. E. Laughlin and K. Hono, Physical Metallurgy Fifth edition. Elsevier (2014).

81) A. Dupasquier, G. Ko¨gel, A. Somoza, Acta Materialia 52 (2004) 4707–4726.

82) R. Lumley, Fundamentals of Aluminium Metallurgy: Production, Processing and Applications. Woodhead Publishing (2011).

83) R.K.W. Marceau, R. Ferragut, A. Dupasquier, M.M. Iglesias and S.P. Ringer, Materials Science Forum 519-521 (2006) 197-202.

84) A. Somoza, A. Dupasquier, I.J. Polmear, P. Folegati and R. Ferragut: Phys. Rev. B 61 (2000) 14454-14463.

85) A. V. Crewe, J. Wall, and J. Langmore, Science, 168 (1970) 1338.

86) P. D. Nellist and S. J. Pennycook, The principles and interpretation of annular dark-field Z-contrast imaging, in Advances in Imaging and Electron Physics, edited by B. Kazan, T. Mulvey and P. Hawkes, 113, Elsevier (2000) 147–203.

87) O. L. Krivanek, M. F. Chisholm, V. Nicolosi, T. J. Pennycook, G. J. Corbin, N. Dellby, M. F. Murfitt, C. S. Own, Z. S. Szilagyi, M. P. Oxley, S. T. Pantelides and S. J. Pennycook, Nature, 2010, 464, 571.

88) S.K. Son, M. Takeda, K.S. Park, M. Mitome, Y. Bando, K.W. Nam and C.Y. Kang, Materials Transactions, 47 (2006) 3001 - 3006.

Chapter 2

Age-hardening Behavior and Precipitation Sequence in Al-Mg-Cu Alloys

2.1 Introduction

In this chapter, general study of aging process in an Al-3Mg-1Cu (wt %) alloy will be conducted. Numerous studies exist concerning age-hardening behavior of the Al-Cu-Mg alloys with higher Cu/Mg ratios. However the Al-Mg-Cu alloys with lower Cu/Mg ratios which are in focus here are much less investigated. The composition of the investigated alloy is located within the (α+S+T) phase field. One of the characteristic feature of the age-hardening response of the Al-Cu-Mg alloy system is the rapid age-hardening phenomena. As described in the previous chapter, the rapid age-hardening has been considered to be attributed to the formation of solute clustering, however there is still no unified interpretation. In this chapter, the rapid age-hardening response will be investigated by means of hardness, electrical resistivity and DSC measurements. DSC is a useful technique to detect small clusters and analyze precipitation sequences. There are many DSC studies on Al-Cu-Mg alloy, however DSC studies on alloys with a composition located within the (α+S+T) phase field are still lucking.

The phase diagram indicates that both S phase and T phase could form in the Al-Mg-Cu alloys. T phase is regarded as isomorphous with the cubic T-$Mg_{32}(Al, Zn)_{49}$ phase which forms in Al-Zn-Mg alloys. However the T phase was not observed in some previous studies [1-3]. Careful TEM observation will be conducted to clarify the precipitation phenomena in an Al-Mg-Cu alloy.

The age-hardening behavior of Al-Cu-Mg alloy system is greatly affected by microalloying elements such as Ag, Si and Zn. However, it is unclear whether other impurity elements such as Fe will affect the age-hardening behavior. In this chapter, an Al-3Mg-1Cu alloy with some impurity elements at industry level will be discussed first, and then a high purity Al-3Mg-1Cu

alloy will be used for the further investigation in order to clarify the age-hardening process occurring in magnesium-rich Al-Cu-Mg alloys.

2.2 Experimental Procedure

2.2.1 Alloy Compositions

The chemical composition of the alloys utilized in this chapter is listed in **Table 2.1**. The Al-3Mg-1Cu alloys lie in the (α+S+T) phase field (**Fig. 2.1**) [4]. These alloys were casted and homogenized at 773 K for 10 h. After the facing work, the billets were rolled to plates with 3 mm in thickness at 683 K. Finally, the plates were cold rolled to 1.2 mm in thickness. The whole manufacturing process was carried out at Furukawa sky (now, UACJ Corporation).

2.2.2 Heat Treatment

Samples were solution treated in a salt bath at 793 K and kept for 3.6 ks with the composition 50 % KNO_3 and 50 % $NaNO_3$, followed by quenching in ice-water and held for 60 s. The as-quenched condition is abbreviated as "A.Q.". The aging treatment was carried out in an oil bath at various temperature.

2.2.3 Micro Vickers Hardness Measurement

The samples of 10 × 10 × 1.2 mm^3 for the hardness measurement were prepared. Micro-Vickers hardness was measured with a load of 500 g for 15 s using a Mitsutoyo HM-102 micro-hardness tester. A value is based on a series of seven indentations. The maximum and minimum values were discarded and the average of the remaining five was used.

2.2.4 Electrical Resistivity Measurement

Specimens for the electrical resistivity measurement were prepared as wires with the diameter of 1.0 mm and the gage length of 300 mm by drawing. Electrical resistivity was measured at 77 K using liquid nitrogen by a four-probe method with 120 mA direct current. Electrical resistivity is calculated using the following equation.

$$\rho = \frac{V_m}{I_{st}} \cdot \frac{A}{L} \ [\Omega m] \qquad (2.1)$$

These symbols ρ, I_{st}, A, V_m and L represent resistivity, constant current (120 mA), cross section of a specimen, potential deference and gage length, respectively.

2.2.5 Differential Scanning Calorimetry (DSC)

DSC measurement was carried out using a Rigaku equipment of DSC8230 under an purified argon atmosphere after heat treatment. The reference material for a DSC analysis were made by pure Al with 99.99 % purity disc shapes with 40 mg in weight. The Al-Mg-Cu samples were made with the same weight as the reference material. The range of temperature for the DSC measurement was set from 223 to 773 K using a liquid nitrogen controller. The starting temperature was always set as 223 k in order to detect thermal reaction at low temperature. The heating rate was 10 K/ min.

2.2.6 Energy Dispersive Spectroscopy (EDS)

Energy Dispersive Spectroscopy (EDS) JXA - 8200 was used to carry out the composition analysis on the samples aged at 443 K for 0.06 ks. The top surface of each sample was prepared by grinding and polishing using increasingly finer grades of SiC paper (320 to 4000 grid) followed by diamond particle suspension (μm) sprayed on to buffer pads.

2.2.7 Transmission Electron Microscopy (TEM)

Specimens for TEM measurement were prepared by electro-polishing with a Tenupol 5 machine (Struers). The electrolyte consisted of 1/3 HNO_3 in methanol and the solution was kept at a temperature between 238 and 253 K. The precipitate microstructure was initially investigated by a conventional TEM in the bright-field mode using a Philips CM30 and a JEOL 3010 operated at 150 kV and 200 kV, respectively. The selected area diffraction patterns (SADP) were taken from the interior of grains. Precipitate structures were investigated by high-resolution HAADF-STEM using a spherical aberration (Cs) probe-corrected JEOL ARM 200F STEM operated at 200 kV. The nominal probe size was 0.08 nm

and the inner collector angle was 50 mrad. In order to reduce contamination, all specimens were treated for a few minutes in a plasma cleaner (Fischione 1020) before HAADF-STEM observations. To enhance contrast, high frequency noise of the HAADF-STEM images were removed by the fast Fourier transform (FFT) filtering using a circular band pass mask.

2.3 Results

2.3.1 Age-hardening Behavior of an Al-3Mg-1Cu Alloy at Various Aging Temperature and the Influence of Impurity Elements

I. Hardness and Electrical Resistivity Changes During Aging at Various Temperatures

The results of hardness changes during aging for an Al-3Mg-1Cu with the industry level impurity elements at various temperatures are shown in **Fig. 2.2**. When the aging temperature is above 373 K, a rapid increase of the hardness occurs in the initial stage followed by a hardness plateau. The rapid hardening contributes as much as 60 % of the total hardening. After the plateau stage, the hardness reaches at the peak. When the aging temperature is below 373 K, the characteristic incubation stage at which no clear hardness increase appears in the initial, and then the hardness increase to reach plateau stage. **Figure 2.3** shows the electrical resistivity increment, $\triangle\rho$, during aging at 443 K and 323 K together with the hardness change. The electrical resistivity, ρ, of alloys containing solute elements, GP zones or precipitates is generally described by the following equation [5].

$$\rho = \rho_0 + \rho_S + \rho_P \qquad (2.2)$$

ρ_0 is the contribution to the electrical resistibility due to the phonon scattering in aluminum. ρ_s is the residual resistance of the solute atoms in the matrix. ρ_p is the contribution to the electrical resistivity due to the formation of solute aggregates. Since ρ_0 is originated in the lattice vibration of aluminum, it depends on temperature and does not change during

isothermal aging treatment. ρ_s is dependent on the solute concentration in the matrix. Since solute concentration decreases with the progress of the phase decomposition, this value decreases with aging time, and it will turn into a certain value by reaching the balanced solute concentration at the temperature. ρ_p is 0 in a perfect supersaturated solid solution. It changes with the formation of solute clusters and is given by the product of function of the number density *N* and size *D* , *G* (*D*).

$$\rho_P = N \cdot G(D) \qquad (2.3)$$

Since the contribution by the increase in the number density of solute clusters and GP zones is large in the early stage of the phase decomposition, electrical resistivity increases and then, the number density of GP zones markedly decreases resulting in the decrease in the resistivity even the average size becomes increased. Finally, the resistivity generally shows a maximum by those balances.

In both aging temperatures, the change of the electrical resistibility during aging corresponds to that of hardness. During aging at 443 K, electrical resistibility goes up rapidly, passing the maximum and decreases gradually at the plateau stage, and finally, decreases rapidly. The rapid increase of the electrical resistibility indicates the formation of solute clusters after short term aging. The plateau at which no resistivity changes is considered to be the incubation period for the precipitation. The rapid fall of the electrical resistibility after long term aging is due to the formation and growth of precipitates.

During aging at 323 K, the incubation stage for a long term is observed as shown in **Fig. 2.3**. After the incubation stage, the electrical resistibility gradually increases and goes up rapidly, and then becomes a certain value. In consistent with the rapid increase of the resistivity during aging at 443 K, the increase during aging at 323 K might come from the formation of solute clustering. In order to investigate the formation behavior of solute clusters during aging at 443 K and 323 K, DSC technique will be applied in the next section.

II. Evolution of Peak A in DSC Curves

A DSC result for the A.Q. specimen of the investigated alloy is shown in **Fig. 2.4**. There is a large exothermic peak A at around 380 K. The peaks at 570 and 610 K could be associated with the precipitation of the S and the T phase respectively since the composition of the investigated alloy is located within the (α+S+T) phase field. Peak A is the first thermal effect detectable during the DSC scan. It refers to a precipitation process taking place during the scan. When the aging treatment at 443 K is applied, peak A is disappeared (**Fig. 2.5 (a)**), indicating the precipitates giving rise to the peak A during the scan is already formed after aging treatment at 443 K. According to the electrical resistivity results, solute clusters might be formed after short term aging at 443 K and the peak A is attributed to the formation of the solute clusters.

When the aging treatment at 323 K is applied, peak A doesn't change during the incubation stage before the hardness and resistivity start to increase. After aging for 345.6 ks, the peak A disappeared, suggesting that the solute clusters form during aging to increase the hardness and resistivity.

III. Influence of Impurity Elements on the Age-hardening Response

Characteristic age-hardening behavior such as the rapid age-hardening and the incubation stage in low-temperature aging has been investigated by hardness, electrical resistivity and DSC measurements. In this section, a high-purity Al-3Mg-1Cu is used in order to investigate the effect of impurity elements such as Mn, Fe and Si on the age-hardening response. **Figure 2.6** shows the hardness and electrical resistivity changes during aging at 443 K for the high purity Al-3Mg-1Cu alloy together with the Al-3Mg-1Cu alloy which was used in previous sections. In the high purity Al-3Mg-Cu alloy, the hardness value at A.Q. state is larger than that of the Al-3Mg-Cu alloy. The plateau hardness of high purity alloy is consistently higher than that of the Al-3Mg-Cu alloy. The value of the peak hardness is almost the same among

two alloys however the time to reach the peak hardness is shorter in the high purity alloy. The change of the electrical resistivity corresponds to that of the hardness in both alloys. In the high purity alloy, the increment of the resistivity in the initial stage becomes large in the high purity alloy, and the resistivity falls more rapidly after plateau stage. It indicates that the age-hardening response of Al-3Mg-1Cu alloy is improved by reducing impurity elements. In the Al-3Mg-1Cu alloy with impurity elements, intermetallic compounds are confirmed as bright and dark contrast by EPMA analysis (**Fig. 2.7 (a)**). In the high purity alloy, much small amount of the intermetallic compounds was confirmed as dark contrast (**Fig. 2.7 (b)**). Results of the EDS analysis for the intermetallic spots and matrix are shown in **Table 2.2**. The qualitative analysis for the composition and volume fraction of the intermetallic compounds are not discussed here, however the analysis reveals that the bright and dark particles are consists of Mg_2Si and Fe intermetallic compounds, respectively. It is suggested that Si contains as an impurity element in the Al-3Mg-1Cu alloy causes the formation of Mg_2Si intermetallic compounds. It might cause the decrease of the solid solubility of Mg atoms into matrix, hence the hardness value of A.Q. state becomes smaller than that of the high purity alloy. However, Chen et al. [6] reported that 0.25 wt% Si addition is effective to improve the age-hardening response of an Al-1.5Cu-4.0Mg (wt %) alloy, despite the low solid solution temperature (773 K) comparing to that of current study (793 K). In their paper, the hardness value of A.Q. state is increased and the time taken to peak hardness is reduced by the addition of Si. Thus, the Fe intermetallic compounds can be considered as the primary factor for the suppression of the age-hardening response in the current investigated Al-3Mg-1Cu alloy.
In order to clarify the age-hardening response of an Al-Mg-Cu alloy, the high purity Al-3Mg-1Cu alloy will be used for the further investigation in the following section. The high purity Al-3Mg-1Cu alloy is renamed as the Base alloy.

2.3.2 Age-hardening Behavior of a High Purity Al-3Mg-1Cu Alloy

I. Microstructural Evolution During Aging at 443 K

The microstructural evolution observed by TEM from the A.Q. condition for the Base alloy (high purity Al-3Mg-1Cu alloy) is shown in **Fig. 2.8**. Dislocation loops and helices are the only microstructural feature and there are no evidence of fine-scale precipitation. The size of the loops increases with aging time (**Fig.2.9**). Vacancies are tend to attract together to form vacancy clusters which can subsequently cause the collapse of the lattice and formation of small dislocation loops [7]. Those loops grow in size due to the absorption of more vacancies. **Figure 2.10** shows TEM bright field images of the precipitates in the $<001>_{Al}$ orientation with corresponding SA diffraction patterns for the Base alloy aged at 443 K for 10.8 ks, 86.4 ks, and for 950.4 ks, which correspond to the middle of the plateau, the end of the plateau and the peak of the hardness respectively. At the middle of the plateau stage, no precipitates are directly detected, although weak spots are observed in the SADP demonstrating the existence of some precipitates as shown in **Fig. 2.10 (a)**. In a similar alloy (Al-3Mg-1Cu (wt %) alloy), Kovarik [8] showed that the weak spots defining small squares between Al reflections including a central spot on the 110_{Al} positions [as seen in **Figs. 2.10 (a)**] are consistent with scattering from GPB zones. At the end of the plateau stage, GPB zones together with heterogeneous precipitates of S' phase on dislocations are observed [**Fig. 2.10 (b)**]. Two arrows in Fig. 2.10 (b) show the GPB zones. In the SADP, weak fourfold arranged spots which indicates the existence of GPB zones are detectable SADP. For longer heat treatments the spots turn into the crosses as seen in **Fig. 2.10 (c)**, similarly centred, indicating the existence of the S' phase together with GPB zones (c.f. Ref. [9], Fig. 14). Thus, the microstructure at the end of the plateau stage should be expected to comprise rod-shaped GPB zones and some large particles of the S' phase, which are shown to nucleate heterogeneously on dislocations [**Fig. 2.10 (b)**]. What is inconsistent with the precipitation

sequence is the presence of a cubic phase having relatively large square cross section [**Fig. 2.10 (c)**] with diffraction patterns incompatible with both the S' and the T phases. The precipitates observed after aging at 443 K for 950.4 ks [**Fig. 2.10 (c)**] will be further investigated in next section by HAADF-STEM.

II. HAADF-STEM Investigation for the Alloy Aged for 950.4 ks

As described in the previous section, three types of precipitates were observed after aging at 443 K for 950.4 ks (**Fig. 2.10(c), (i)-(iii)**).

(i) First, nanoscale thin, needle-like particles extending along $<001>_{Al}$ are observed by their cross-sections appearing as small dark dots. These precipitates are GPB zones. The atomic arrangement in the GPB zone structure is readily confirmed in the HAADF-STEM images. The zone cross-sections can be investigated in the $[001]_{Al}$ orientation. The atomic columns along $<001>_{Al}$ give rise to different intensities. By the atomic number contrast (Z-contrast) the intensity is proportional to $Z^{1.7\text{-}1.9}$ [10, 11]. A typical image of the cross-section of a GPB zone is given in **Fig. 2.11 (a)**. Individual columns are well resolved. The GPB zone and matrix have common (0.405 nm) periodicity in the viewing direction. A column is always associated with one of the two $(001)_{Al}$ planes over the 0.405 nm unit distance. The structure of the GPB zones was first identified by Kovarik et al. [8, 12-14]. The element map in **Fig. 2.11 (b)** based on their work [7], shows that lateral periodicity is absent, and that the structure is defined in terms of similar groups / molecules of eight columns (composition $Al_2Mg_3Cu_3$) stacked in various manners along $<001>_{Al}$. The seven peripheral columns of such groups are marked by a semi-circle. Kovarik et al. defined the molecules of eight columns as "a half of unit" and pair of those units as "single unit" [12]. Therefore, GPB zones in **Fig. 2.10** is agglomerate of two single units. Notation for the structural units of the GPB zone is shown in **Table 2.3** [12]. The central Al-column of a half unit always takes the "wrong" height in the Al matrix, meaning its atoms are interstitial. This could be

caused by strain set up by the Mg-atom triples in the $(001)_{Al}$ planes (on each semi-circle). Mg atoms are considerable larger than Al atoms, and more space is appreciated in the plane. This is achieved if the central Al atom can move to the neighbour plane. Although this is an interstitial position, it is advantageous because the Al atom will now be surrounded by three small Cu-atoms. Even better accommodation of strain is probably achieved through the pairing of two such molecular groups related to two different $(001)_{Al}$ planes, as illustrated by the white and grey fill of the Al centres in **Fig. 2.11 (b)**.

(ii) Second, a class of larger precipitates, forming preferentially on dislocation lines was determined to be the S' phase (**Fig. 2.12**). It shows typical lath-like cross-sections with the particles extending all through the specimen. Similar images of S' can be found in a previous investigation [15]. The a-axis (viewing direction) is always along $<001>_{Al}$, while the two other bases point in mutually normal $<120>_{Al}$ directions. **Figure 2.12** also indicates that the c-axis is the normal of the main lath-plane. For the particles observed, the main interface (trace along $\boldsymbol{b}_{S'}$) appears to be coherent. This interface shows no deviation from the bulk structure, with Cu-columns lying on a straight line. The other interfaces can usually be defined to be periodically arrangements of triples / triangles of Cu columns, achieved by one or two additional outer Cu columns, which are not part of the normal bulk structure. A higher magnification of a section of an S' lath is shown in **Fig. 2.12 (c)**, with unit cell and atomic overlay suggesting the species of the interface columns. For example, **Fig. 2.12 (b)** shows that the columns of the buckled Al planes (marked by the dotted lines) running along the boundary match the particle columns periodically. The dimension of axis $\boldsymbol{b}_{S'}$ and $\boldsymbol{c}_{S'}$ is given as 0.927 nm and 0.713 nm, respectively [16, 17].

(iii) In addition to particles of the S' phase, square cross sections appeared in **Fig. 2.10 (c)-(iii)**. The cross sections belong to a much coarser rod-like phase in the $<001>_{Al}$ orientation (**Fig. 2.13**). In the orientation along the rods, a square cell is identified and its diffraction

pattern can fit two phases; T (a_T=1.416 nm) [18-20] and Z (a_Z=1.999 nm) [21] if indexed as a cubic structure, where $a_Z \approx a_T \sqrt{2}$. **Fig. 2.14** shows nano-beam electron diffraction patterns (a) along and (b) perpendicular to the rods. Evaluating other zone axes, it was found that the patterns correspond with the Z phase as first reported by Chopra et al. [21] in an over-aged Al-1.5wt% Cu-4.0wt% Mg-0.5wt% Ag alloy aged for 100 days at 170 °C. Chopra et al. [21] found two orientation relationships. It is clear that the particle in **Figs. 2.13** and **2.14** follows the primary relationship, i.e. where the cubic cells of Al and Z phase are parallel, i.e. $[100]_{Al} \parallel [100]_Z$, $(001)_{Al} \parallel (001)_Z$. Besides, the structure of Z phase was found to be easily damaged under electron beam, probably by oxidation. It prevented us to obtain good high-resolution images of Z phase.

III. DSC Analysis

Figure 2.15 shows DSC curves for the Base alloy aged at 443 K for various times. Heating rate is 10 K/ min. In a curve for A.Q. specimen, there is a large exothermic peak A at around 360 K. At around 510 K, 560 K and 620 K, there are three exothermic peaks named as peak B, C and D respectively. Peak B appears within two endothermic peaks (as black arrows shown in **Fig. 2.15**). Those two endothermic peaks are attributed to dissolution of precipitates whose formation give rise to peak A and B. In order to characterize the precipitation kinetics and determine the activation energy for the precipitation which corresponds to each peak, various heating rate are applied to DSC measurement. **Figure 2.16** shows DSC curves with different heating rate from 5 to 20 K/min. There are several methods to determine the activation energy for the precipitation process using peak temperature in DSC curves. Isoconversion methods for activation energy analysis with typical sources of error is shown in **Table 2.4** [22]. In this study, Kissinger's method which is considered as the most accurate one [23, 24] is applied. The Kissinger equation can be written as follows,

$$\ln\left(\frac{\gamma}{T_P^2}\right) = -\left(\frac{E_a}{R}\right)\left(\frac{1}{T_P}\right) + C \qquad (2.4)$$

where γ is the heating rate, T_P is the peak temperature of the given process, E_a is the activation energy, R is the universal gas constant and C is a constant. **Figure 2.17** shows $\ln(\gamma/T_P^2)$ versus $1000/T_P$ relationships. The activation energies for each peak are calculated from the slopes of the obtained relationships are summarized in **Table 2.5**.

(i) The activation energy for peak A is much smaller than the activation energies for diffusion of alloying elements, Cu and Mg in Al (133.9 kJ/ mol and 120.5 kJ/ mol, respectively) [25]. This difference is generally ascribed to the presence of excess vacancies. Since the specimens were quenched from the solution temperature, it involve substantial amounts of the quenched-in vacancies. If vacancies play a key role in helping solute clustering during the initial aging, the activation energy for migration of (mono) vacancies (about 60 kJ/mol in pure Al [26, 27]) can be determining the activation energy of the overall process. The presence of a large amount of excess vacancies can reduce the activation energy for diffusion of alloying elements since the activation energy for diffusion is the sum of the activation energy for creation of a vacancy and for the migration of the alloying element into the vacancy. The presence of excess vacancies cause the former (activation energy for creation of a vacancy) effectively zero. Therefore, the kinetics of the precipitation process which corresponds to peak A could be controlled by the migration of vacancies, in other words, Cu/Mg/vacancy solute clustering. Peak A is fully disappeared after aging for 0.06 ks, where the hardness and electrical resistivity increases rapidly. From the microstructural observation, no precipitates were directly detected in the initial stage of aging. Therefore, it is suggested that the precipitates responsible for peak A is solute clusters and is responsible for the rapid increase in the hardness and electrical resistivity.

(ii) Peak B remains during short term aging and it disappears gradually with aging proceeds. The activation energies for peak B is close to the activation energies for diffusion of alloying elements, Cu and Mg in Al (133.9 kJ/ mol and 120.5 kJ/ mol, respectively) [25]. Thus, precipitation kinetics which corresponds to peak B could be controlled by Cu and Mg diffusion in Al. Peak B was also obtained in Al-Cu alloys by Takeda et al.[28] and they determined that this peak is attributed to the formation of GP zone. For the present alloy, peak B is considered as the reaction of GPB zone formation according to the precipitation sequence in Al-Mg-Cu alloy system. This is in consistent with the result obtained by TEM that GPB zones were not observed in the early stage of aging however it appeared by aging proceeds.

(iii) In line with results from literature [29], peak C is attributed to the formation of S' phase. The activation energy for peak C is in fair agreement with the activation energies for diffusion of alloying elements, Cu and Mg in Al (133.9 kJ/ mol and 120.5 kJ/ mol, respectively). Thus, precipitation kinetics for S' phase could be controlled by Cu and Mg diffusion in Al.

(iv) The activation energy for peak D is large comparing to that of peak C and also that of Cu and Mg diffusion in Al. According to the microstructural observation, peak D could be associated with the precipitation of Z phase which appeared only after long term aging.

2.4 Discussion

2.4.1 Evolution of the Peak A in the DSC Curves

In the present study, a large exothermic peak A has been found in the DSC curves for the A.Q. specimen. The activation energy for this peak A was evaluated as 79.9 kJ/mol by Kissinger’s method. Since the peak A disappeared after aging for 10s, this peak is considered to be

attributed to the formation of solute clusters, probably Cu/Mg/Vac clusters. Peak A also appears in the DSC curves for the Al-4Cu and Al-4.2Cu-0.2Mg alloys at A.Q. state during heating (**Fig. 2.19**). For the Al-4Cu alloy, Somoza et al. reported that vacancy-Cu pairs are present immediately after quenching and vacancies are released when aging progresses with the formation of Cu clusters [30]. Thus, the peak A in the DSC curve for the Al-4Cu alloy is attributed to the formation of Cu/vacancy clusters. Takeda et al. observed Cu atom clusters of approximately 5 nm in size in an Al-1.94 Cu (at %) alloy aged at 403 K for 0.6 ks by high-resolution TEM [28]. This clusters are observed as Cu-rich (100) planes. During aging treatment, the cluster becomes mono-layer G.P. (I), bi-layer G.P. (II) and multi-layer θ", continuously. Considering the HRTEM images together with the DSC results, Takeda et al. [28] concluded that the exothermic peak appeared in a DSC curve at around 350 K is attributed to the formation of Cu atom clusters. If the alloy contains small amount of Mg (Al-4.2Cu-0.2Mg alloy), the peak A temperature is shifted to higher temperature and the peak area becomes larger. For the Al-4.2Cu-0.24Mg alloy, Cu/Mg/vacancy clusters might be formed during DSC scanning and the peak A temperature is shifted because of the different thermal stability of the cluster comparing to that of the Al-4Cu alloy. For the Base (Al-3Mg-1Cu) alloy, the peak A might be attributed to the formation of Cu/Mg/vacancy clusters based on the alloy composition. Further investigation for the formation behavior of solute clusters during initial stage of aging in the Base alloy will be conducted by means of HAADF-STEM and three-dimensional atom probe (3DAP) techniques in Chapter 3.

2.4.2 Incubation Stage in Low Temperature Aging

The incubation stage before the rapid age-hardening was found at lower aging temperatures in the present works. This is very different from the case of Al-Cu alloys [31] which show almost no incubation stage and the hardness increases rapidly at low temperature aging. This rapid increase of the hardness is designated as the fast reaction stage. The fast reaction stage

is generally observed in the age-hardening aluminum alloys such as Al-Cu-Mg, Al-Mg-Si, Al-Zn and Al-Zn-Mg alloys. **Figure 2.18** shows the hardness changes during natural aging (room temperature aging) for an Al-4Cu (wt %) alloy and an Al-4.2Cu-0.2Mg (wt %) alloy. For the comparison, the aging curve for the Base alloy (high purity Al-3Mg-1Cu alloy) is also shown. The fast reaction stage appears in both Al-4Cu and Al-4.2Cu-0.2Mg alloys. This stage appears due to the enhanced diffusion of solute atoms by the quenched-in excess vacancies. The activation energy for the fast reaction is determined as 50~80 kJ/mol in the Al-Cu alloy, in agreement with the migration energies of Cu (66.5 kJ/ mol) in Al.

It has been known that the activation energy for Mg diffusion in an Al alloy is lower than that for Cu diffusion. Thus, Mg-vacancy clusters are expected to be formed as the first type of solute clusters. The Cu composition of the present Al-Mg-Cu is very low compared to the Mg composition (Mg: 3.52 at %, Cu: 0.45 at %). Therefore, it must be difficult to meet Mg-Vac clusters and Cu atoms together and it takes time to form Mg/Cu/vacancy solute clusters at low temperature, resulting in the incubation stage. This is different from the Al-Cu-Mg alloys with high Cu/Mg composition. On the other hands, during aging at medium temperature (443 K), the hardness increases rapidly in Al-Mg-Cu. Thus, it is suggested that Mg/Cu/vacancy solute clusters form rapidly at 443 K and this clusters contributes the rapid hardening. The interaction between solute atoms and vacancies will be investigated by positron annihilation spectroscopy (PAS) technique in Chapter 3.

2.4.3 Precipitation After Long term Aging

The investigated alloy lies in the (α+S+T) phase field. However, T phase was not confirmed by TEM investigation. Instead of the T phase, large particles of Z phase were found in the Base alloy only after the longest aging time [**Fig. 2.10 (c)**]. Recently, Macchi et al. also reported that Z phase formed after long term aging in an Al-1.5Cu-4Mg (wt %) alloy [32]. In addition, they reported that there were no evidence that the Z phase is preceded by any pre-

precipitate or GP zones. Formation mechanism of the Z phase remains to be fully understood. However, it has been reported that trace additions of Ag enhance the strengthening during aging by promoting the precipitation of finely distributed Z phase and suppressing the precipitation of the S phase in Al-Cu-Mg ternary alloys [33-35]. Effect of the trace addition of Ag will be discussed in **Chapter 5**.

2.5 Conclusions

1. The Al-3Mg-1Cu alloy showed three stages of age-hardening reactions, the first hardening stage which occurs very rapidly (within 0.06 ks at 443 K), plateau stage where the hardness remain constant for a long time, and the second hardening stage. It is understood that the first, plateau and second stages are attributed to the formation of solute clusters, the incubation period for the precipitation of GPB and S', and the precipitation of those phases, respectively.
2. A large exothermic peak A was observed as the first reaction during DSC scanning. The peak A disappeared after short term aging (0.01 ks at 443 K). It was suggested that solute clusters were formed very rapidly and it contributed the rapid age-hardening response.
3. At low temperature aging, there was a characteristic stage where no hardness increase occurs before the rapid increase in the hardness. Considering the DSC results, it was suggested that this stage is an incubation stage for the formation of solute clusters. The existence of the incubation stage at low temperature aging is characteristic phenomena for the Al-Mg-Cu alloys which is different from the general age-hardenable aluminum alloys.
4. Longer aging led to combination of GPB zones, S' precipitates and Z phase. Z phase consists of large rods of square cross-sections extending along <100>Al directions. T phase was not observed. The GPB survived for long heat treatment times.

References

1) J.T. Vietz and I.J. Polmear, J. Inst. Metals 94 (1966) p.410.

2) P. Ratchev, B. Verlinden and P. Van Houtte, Scripta. Metall. 30 (1994) p.599.

3) P. Ratchev, B. Verlinden, R. De Smet and P. Van Houtte, Acta Mater. 46 (1998) p.3523.

4) G. B. Brook: Precipitation in Metals, Spec. Rep. No. 3, Fulmer Res. Inst., UK (1963).

5) K. Osamura, Y. Hiraoka and Y. Murakami: Philosophical Magazine 27 (1973) 809-825.

6) Z. Chen, J. Zhang, J. Shu, G. Sha, J. Xia, S. Wang and S.P. Ringer: Philosophical Magazine Letters 93 (2013) 648-654.

7) D. Kuhlmann-Wilsdorf and H. G. F. Wilsdorf: Jounal of Applied Physics 31 (1960) 516-525.

8) L. Kovarik, P.I. Gouma, C. Kisielowski, S.A. Court and M.J. Mills, *Acta Mater.* 52 (2004) 2509-2520.

9) S. C. Wang, M. J. Starink, Int. Mater. Rev. 50 (2005) 193-215.

10) S. J. Pennycook, S. D. Berger, R. J. Culbertson, *J. Microsc.* **144** (1986) 229-249

11) S. J. Pennycook, *Adv. Imag. Electr. Phys.* **123** (2002) 173-206

12) L. Kovarik, S. A. Court, H. L. Fraser, M. J. Mills, *Acta Mater.***56** (2008) 4804-4815

13) L. Kovarik, M. J. Mills, *Scripta Mater.* **64** (2011) 999-1002

14) L. Kovarik, M. J. Mills, *Acta Mater.* **60** (2012) 3861-3872

15) S. P. Ringer, T. Sakurai, I. J. Polmear, *Acta Mater.* **45** (1997) 3731-3744

16) B. Heying, R.-D. Hoffmann, R. Pöttgen, Z. Naturforsch. 60B (2005) 491-494.

17) Z. R. Liu, J. H. Chen, S. B. Wang, D. W. Yuan, M. J. Yin, C. L. Wu, Acta Mater. 59 (2011) 7396-7405.

18) G. Bergman, J. L. T. Waugh, L. Pauling, *Acta Cryst.* **10** (1957) 254-259

19) G. Bergman, J. L. T. Waugh, L. Pauling, Nature, 169 (1952) 1057-1058

20) M. Audier, P. Guyot, *Extended Icosahedral Structures*, San Diego: Academic Press (1989).

21) H. D. Chopra, B. C. Muddle, I. J. Polmear, *Phil. Mag. Lett.* **73** (1996) 351-357

22) M. J. Starink, International Materials Reviews, 49 (2004) 191-226.

23) H. E. Kissinger: J. Res. NBS. 57 (1956) 217–221.

24) A. S. Abdel-Halim, Y. K. Afifi and N. Afify: J. Ther. Anal. 32 (1987) 1071–1079.

25) Yong Du, Y.A. Chang, Baiyun Huang, Weiping Gong, Zhanpeng Jin, Honghui Xu, Zhaohui Yuan, Yong Liu, Yuehui He, F.-Y. Xie, Materials Science and Engineering A363 (2003) 140–151.

26) R. W. Siegel, J. Nucl. Mater., 69–70 (1978) 117–146.

27) W. DeSorbo and D. Turnbull, Acta Metall., 7 (1959) 83–85.

28) M. Takeda, S. K. Son, Y. Nagura, U. Schmidt, and T. Endo: Zeitschrift für Metallkunde 96 (2005) 870-873.

29) G. W. Smith: Thermochimica Acta 317 (1998) 7-23

30) A.Somoza, M.P. Petkov and K.G. Lynn, Physical review B, Vol. 65 (2002)

31) T. Sato, Y. Kojima and T. Takahashi: J. Jpn. Inst. of Light Metals. 27 (1977) 488.

32) C. Macchi, A. Tolley, R. Giovachini, I.J. Polmear, A. Somoza: Acta Materialia 98 (2015) 275–287.

33) R.K.W. Marceau, G. Sha, R. Ferragut, A. Dupasquier, S.P. Ringer: Acta Materialia 58 (2010) 4923–4939.

34) H. D. Chopra, B. C. Muddle, I. J. Polmear, Phil. Mag. Lett. 73 (1996) 351-357.

35) H. D. Chopra, L. J. Liu, B. C. Muddle, I. J. Polmear, Phil. Mag. Lett. 71 (1995) 319-324.

Table 2.1 Chemical compositions of the investigated alloys.

(wt %)

Sample	Mg	Cu	Si	Fe	Ti	Al
Al-3Mg-1Cu	3.04	0.97	0.09	0.07	0.01	Bal.
High purity Al-3Mg-1Cu (Base alloy)	3.04	1.01	0.01	0.01	0.00	Bal.
Al-4Cu	-	4.07	0.00	0.00	0.00	Bal.
Al-4.2Cu-0.2Mg	0.20	4.24	0.00	0.00	0.00	Bal.

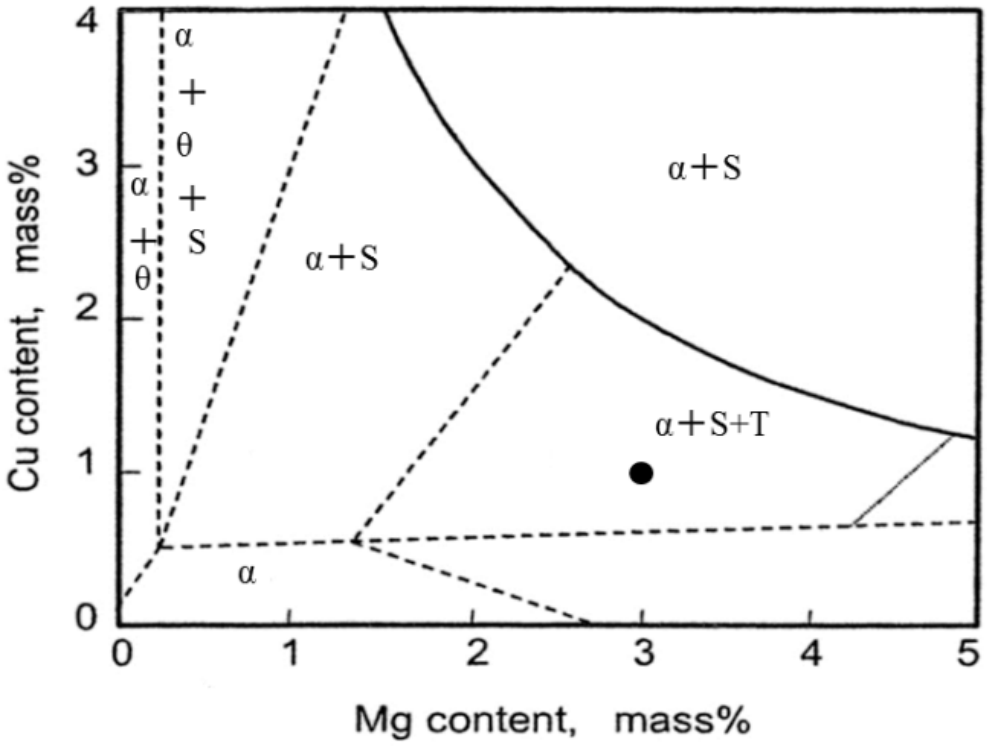

Fig. 2.1 Al-Cu-Mg phase diagram showing the composition of investigated alloys [4].

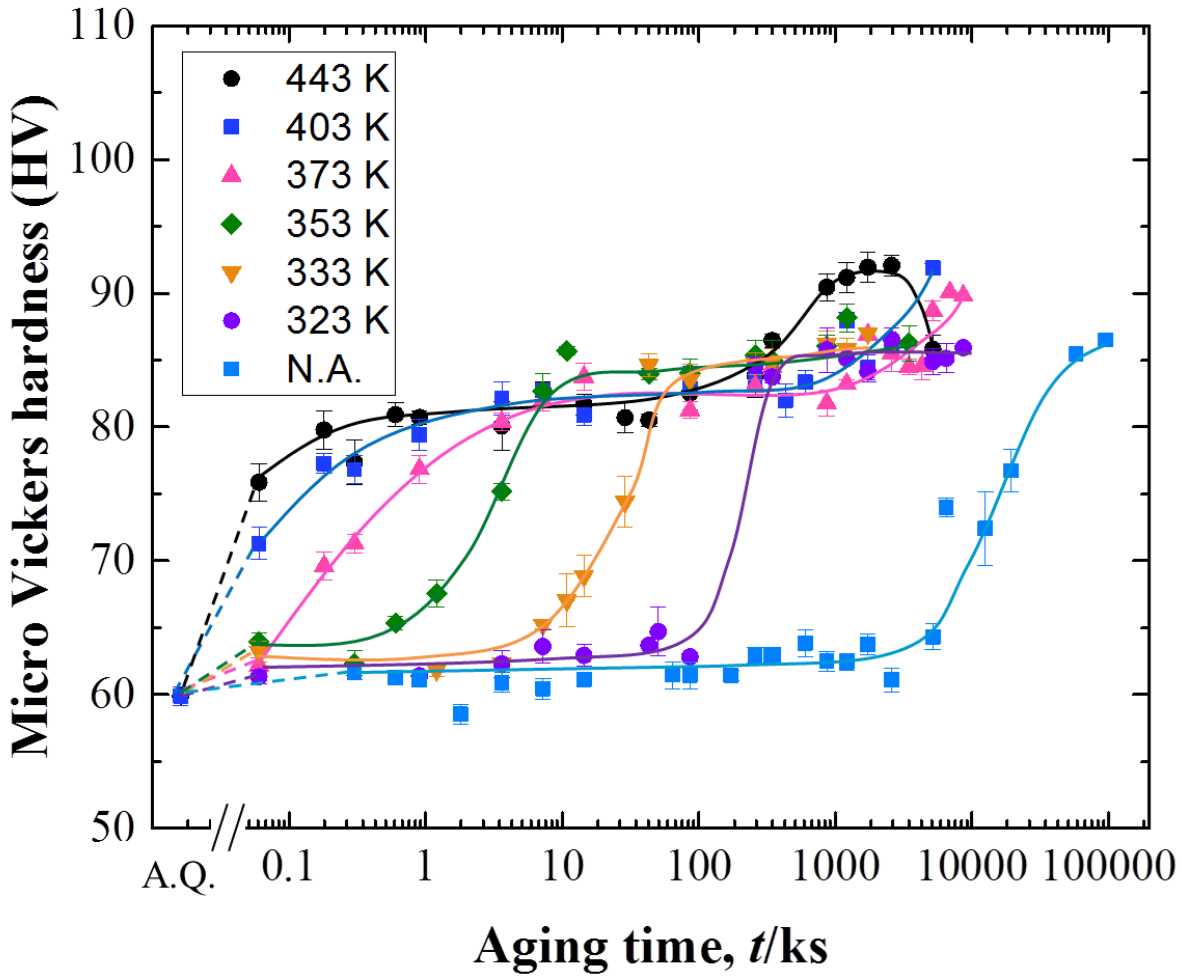

Fig. 2.2 Hardness changes during aging at various temperatures for the Al-3Mg-1Cu alloy.

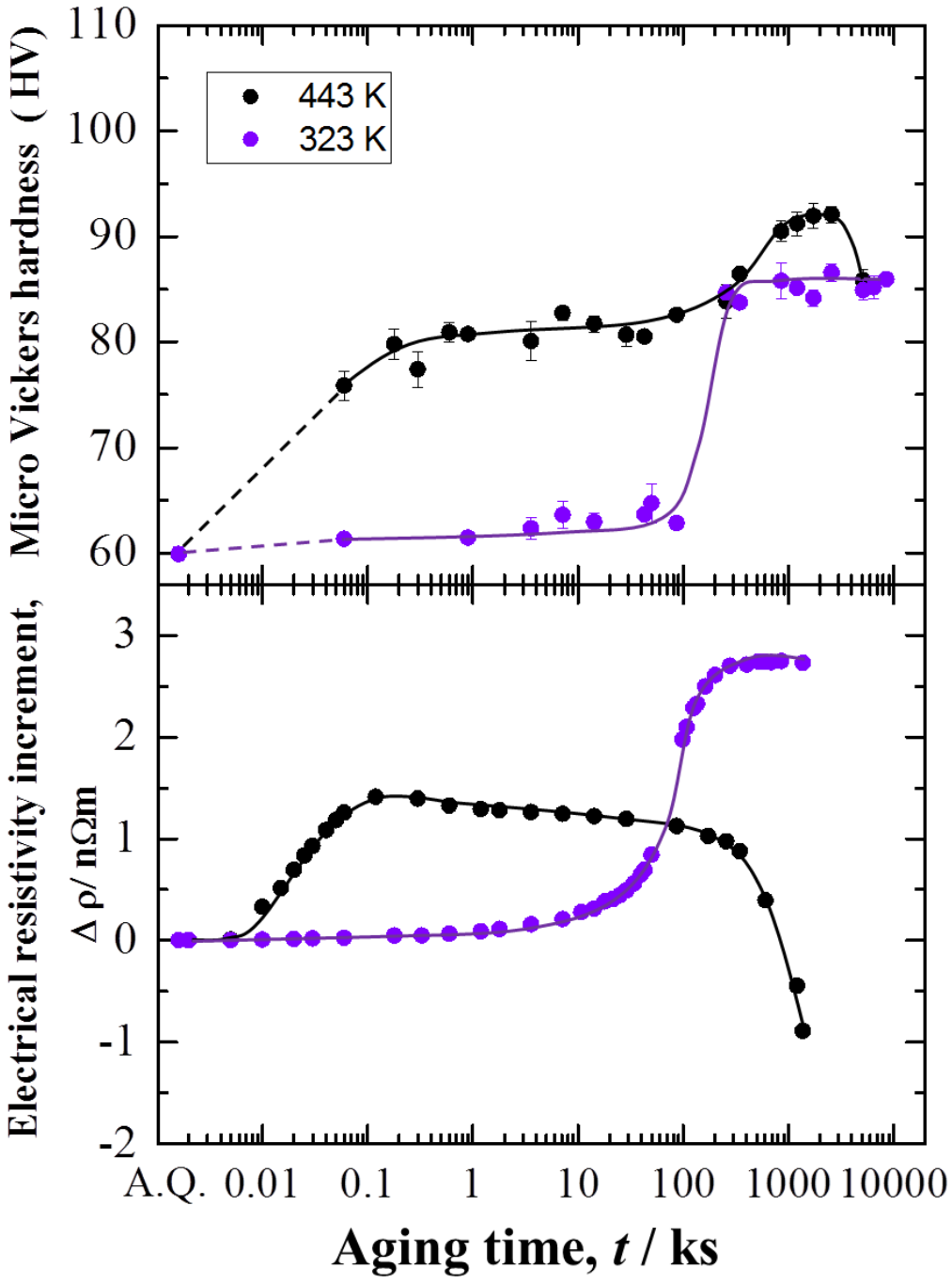

Fig. 2.3 Hardness and electrical resistivity changes for the Al-3Mg-1Cu alloy during aging at 443 K and 323 K.

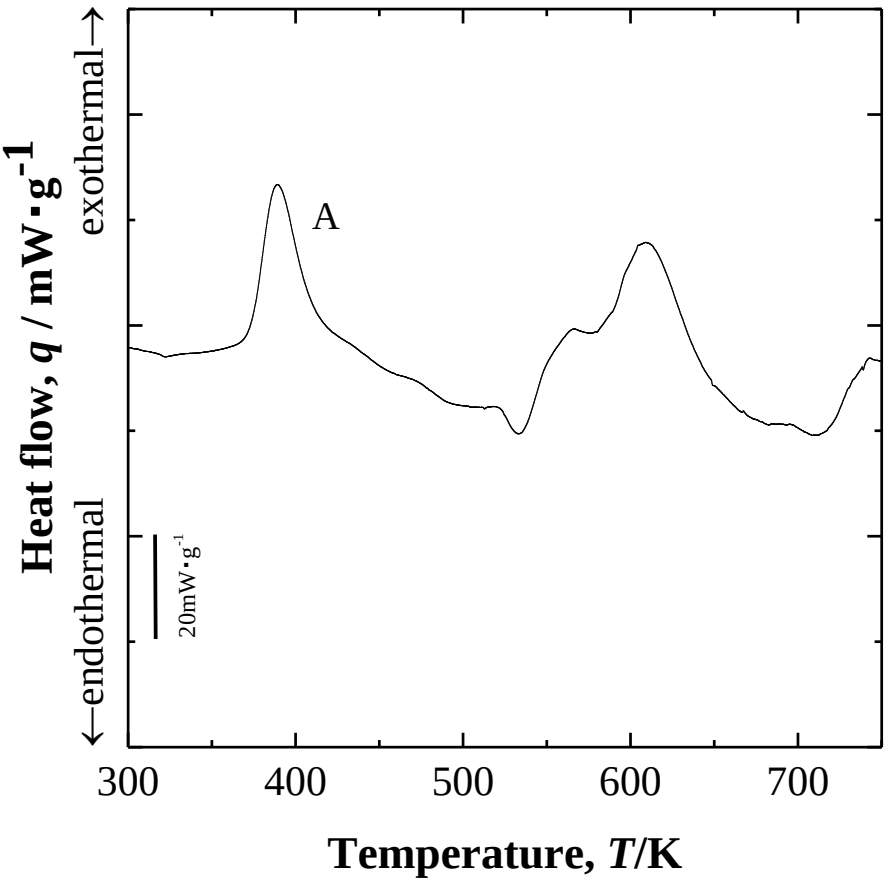

Fig. 2.4 DSC curve for the as-quenched Al-3Mg-1Cu alloy.

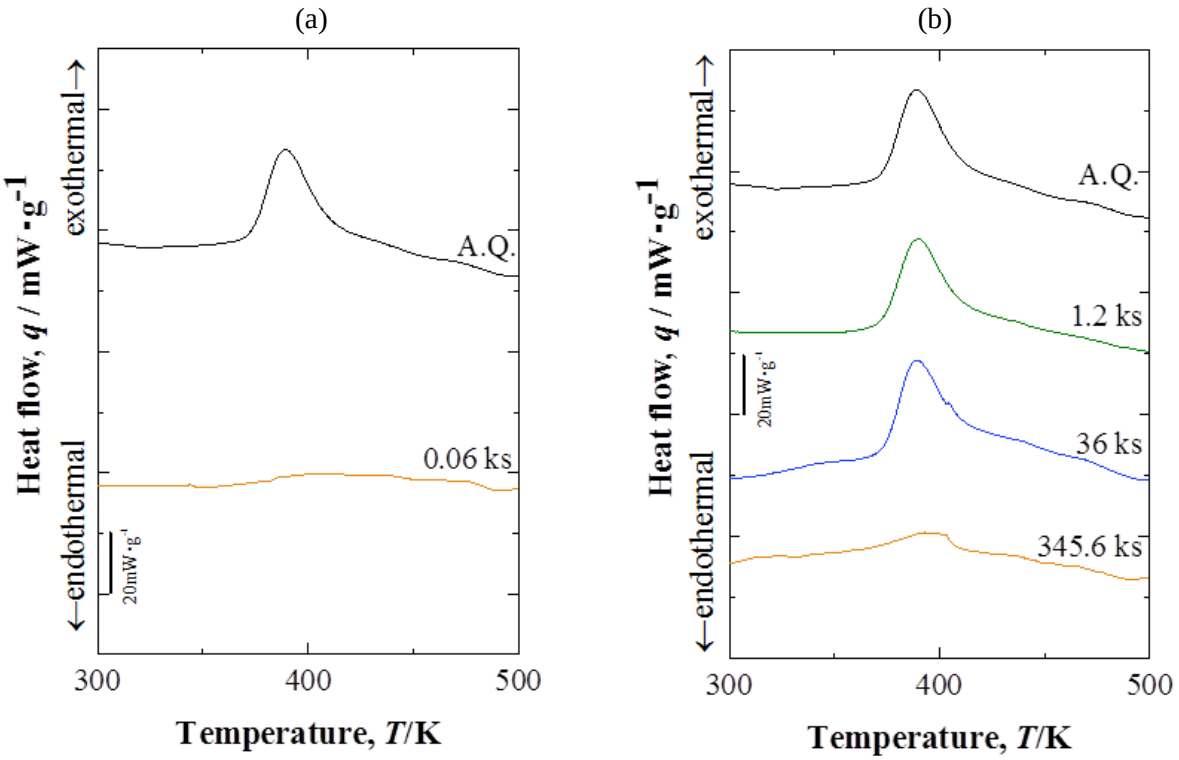

Fig. 2.5 DSC curves for the Al-3Mg-1Cu alloy aged at (a) 443 K and (b) 323 K. Heating rate is 10 K/ min.

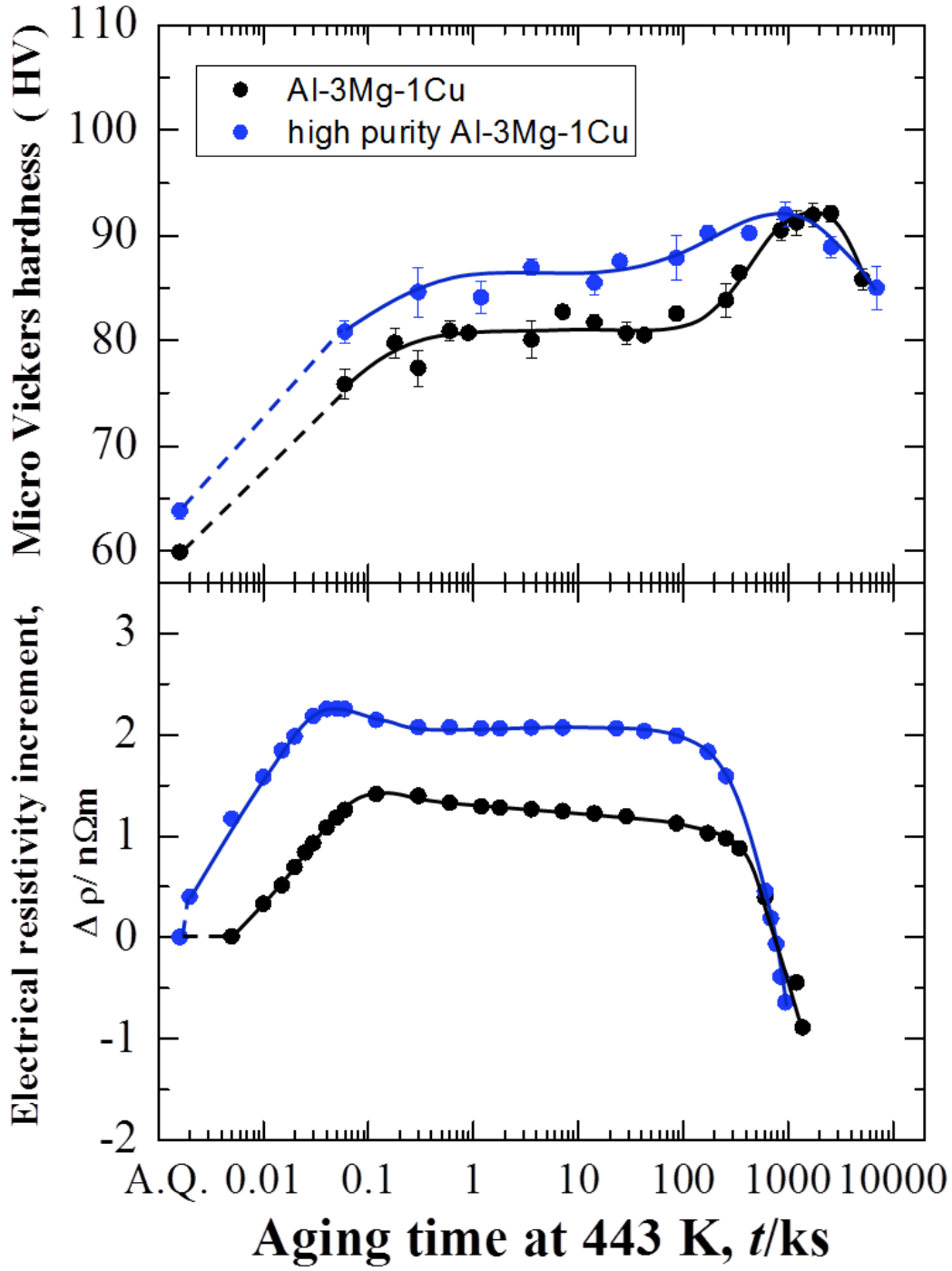

Fig. 2.6 Hardness and electrical resistivity changes for the Al-3Mg-1Cu and high purity Al-3Mg-1Cu alloys during aging at 443 K.

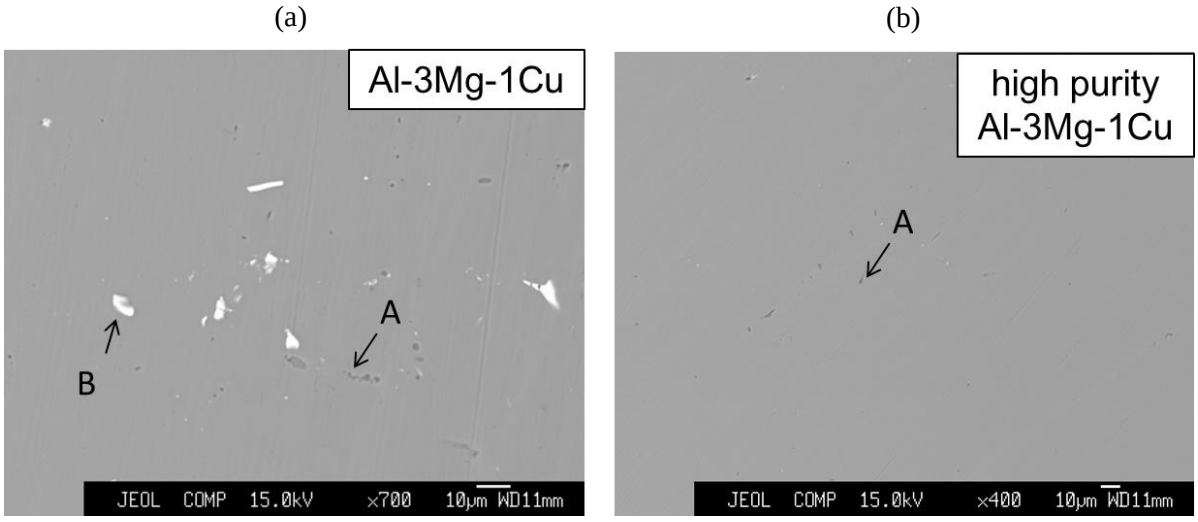

Fig. 2.7 Backscattered electron micrographs for the (a) Al-3Mg-1Cu alloy and (b) high purity Al-3Mg-1Cu alloy aged at 443 K for 0.06 ks.

Table 2.2 EDS results of the (a) Al-3Mg-1Cu alloy and (b) high purity Al-3Mg-1Cu alloy, taken on the A: black spot, B: white spot and matrix background.

(a)

(wt %)

Al-3Mg-1Cu	Mg	Cu	Si	Mn	Fe	Ni	Al
Matrix	4.614	0.855	0.027	-	0.024	-	94.980
A	19.133	0.654	**10.994**	0.007	0.071	0.017	69.124
B	1.034	1.257	0.014	0.025	**4.259**	0.224	93.187

(b)

(wt %)

high purity Al-3Mg-1Cu	Mg	Cu	Si	Mn	Fe	Ni	Al
Matrix	5.232	1.118	0.006	0.012	-	0.013	95.299
A	4.592	1.042	**0.148**	0.017	-	-	4.791

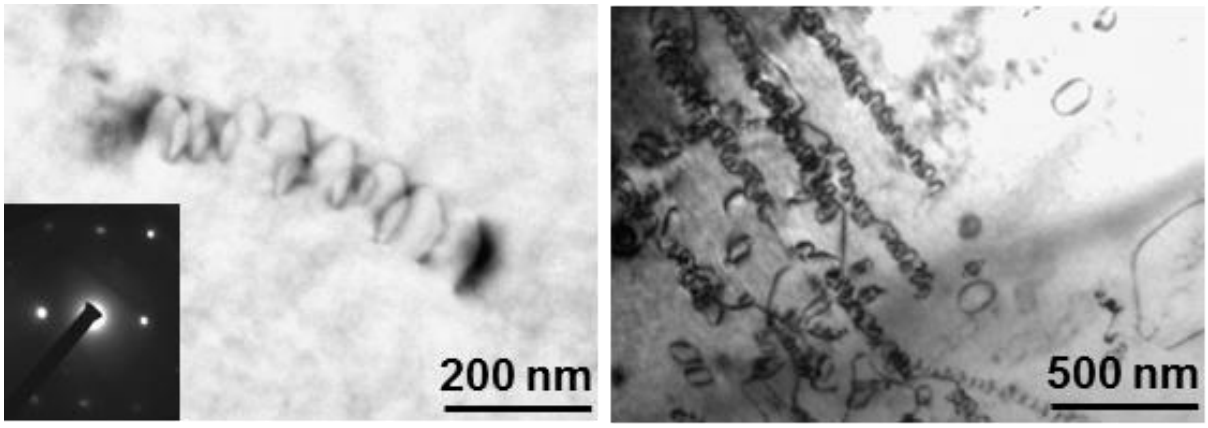

Fig. 2.8 Bright field TEM images with selected area diffraction patterns taken along $<112>_{Al}$ for the Base alloy at as-quenched state.

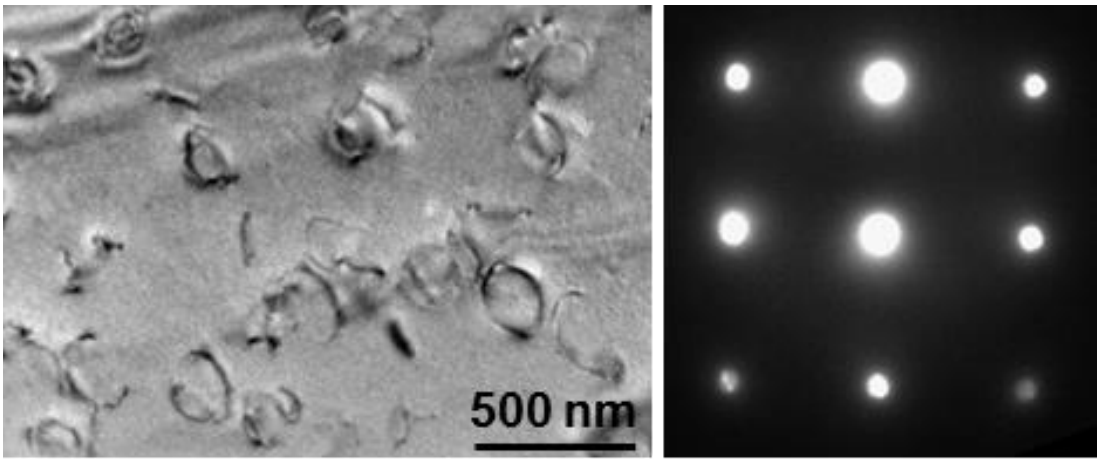

Fig. 2.9Bright field TEM images with selected area diffraction patterns taken along $<001>_{Al}$ for the Base alloy aged at 443 K for 0.06 s.

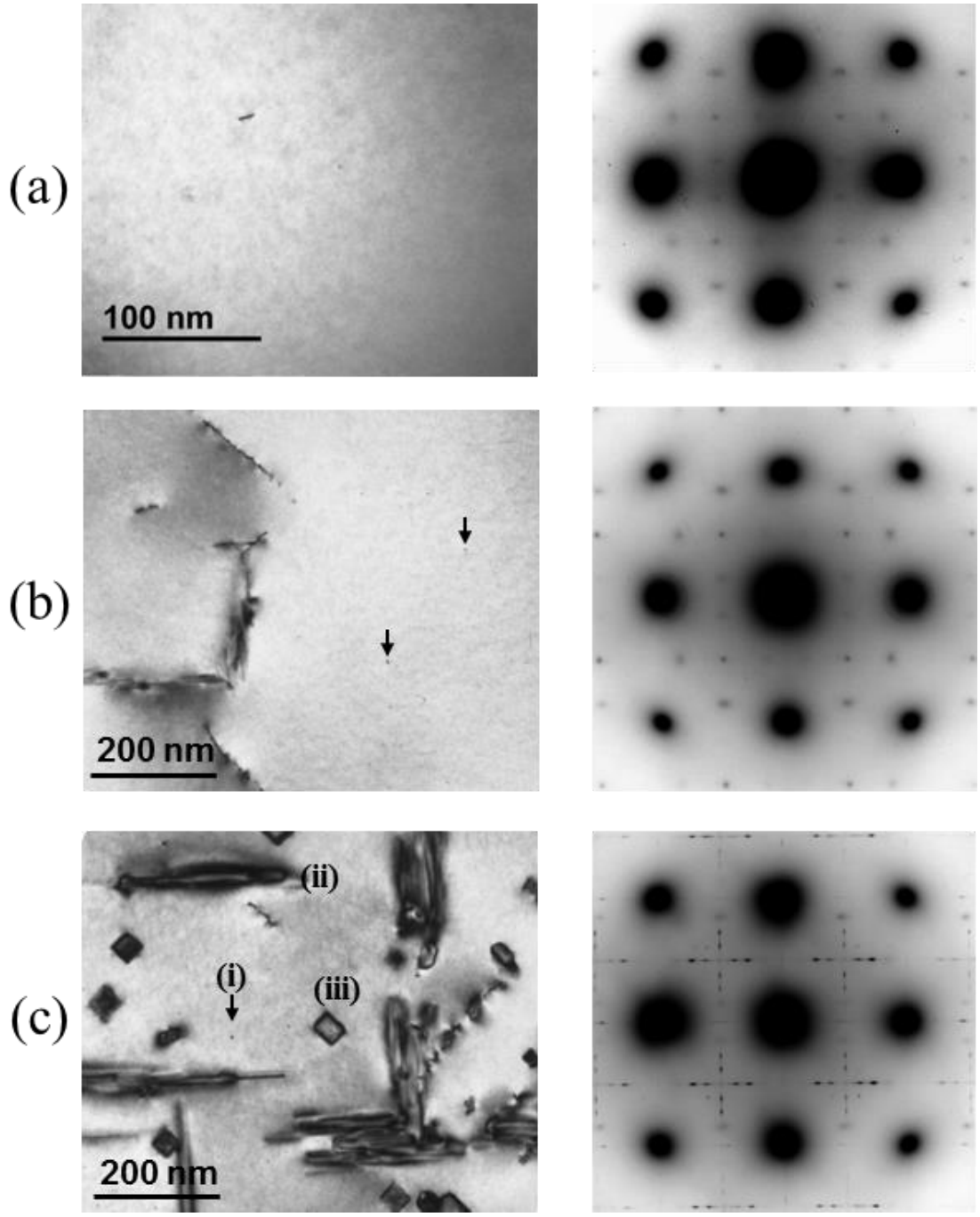

Fig. 2.10 Bright field TEM images with selected area diffraction patterns taken along $<001>_{Al}$ for the base alloy aged at 443 K for (a) 10.8 ks, (b) 86.4 ks, and (c) 950.4 ks corresponding to the hardness plateau, the second hardening increase, and the hardness peak, respectively. Weak fourfold arranged spots in the SADP (a-c) show the GPB zones surviving to long aging times. The typical cross-sections of (i) a GPB zone, (ii) S' laths, and (iii) a Z-phase rod are shown in (c).

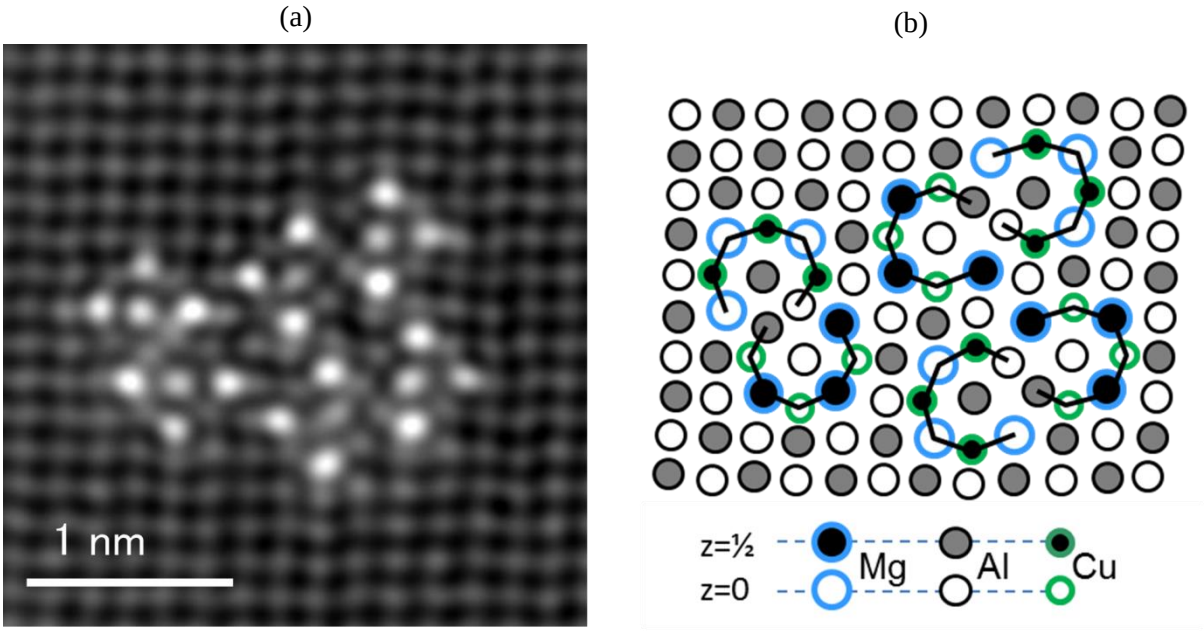

Fig. 2.11 (a) HAADF-STEM image along <001>$_{Al}$ and (b) deduced map of all elemental columns over the cross-section of a GPB zone in the Base alloy aged for 950.4 ks at 443 K. Columns correspond to the two Al planes z=0 and ½ (0.203 nm). Together with the center, a black curve defines the columns of the basic unit ($Al_2Mg_3Cu_3$). Units in a pair are on different heights.

Table 2.3 Notation for the "structural units" of the GPB zone. [12]

Half unit	Single unit	Double unit	Agglomerate of two single units
			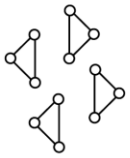

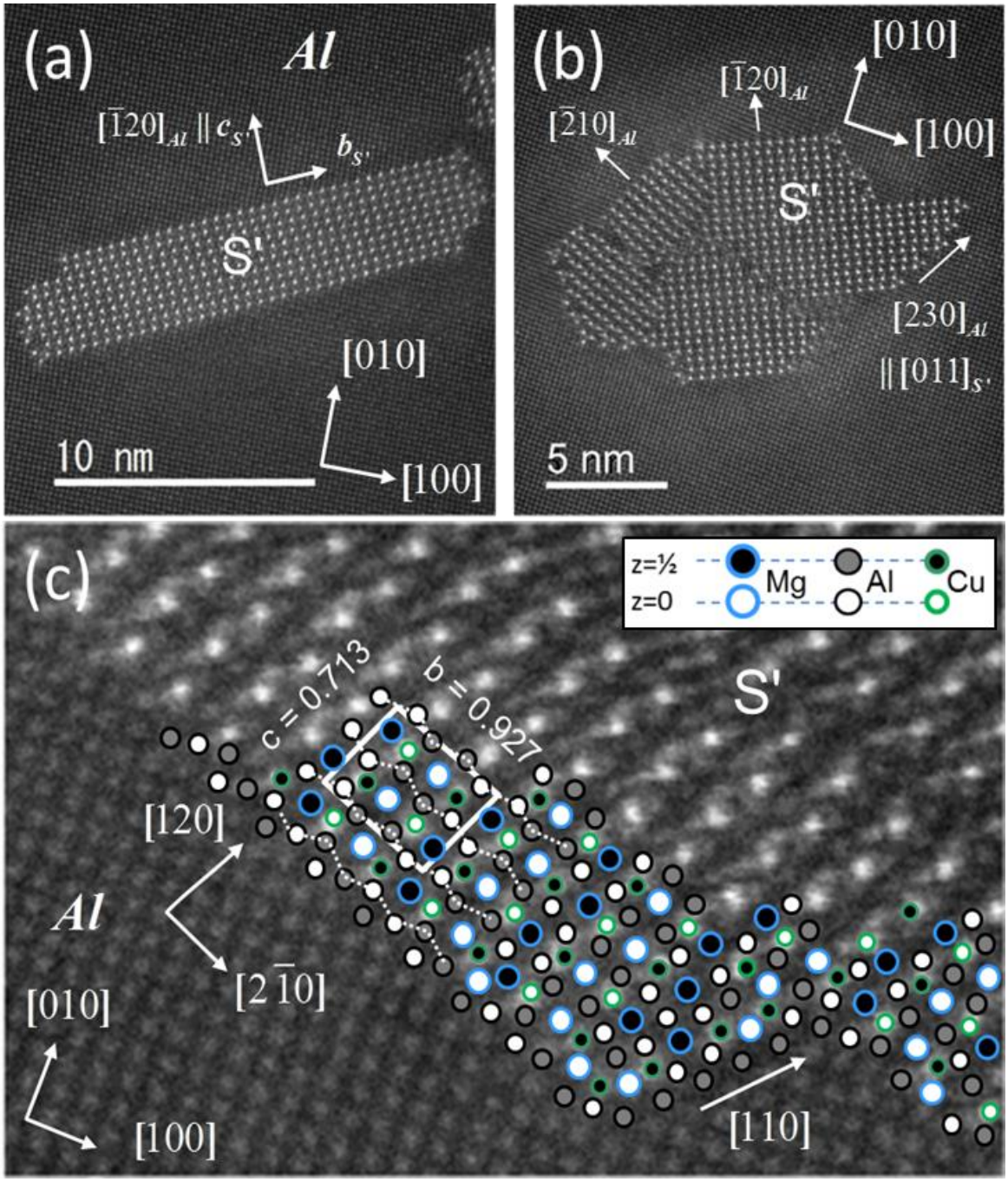

Fig. 2.12 HAADF-STEM images along $< 001 >_{Al} \| [100]_{S'}$ of S' laths in the Base alloy aged for 950.4 ks at 443 K showing (a) S' main interface has normal $\boldsymbol{c}_{S'} \| [1\bar{2}0]_{Al}$, (b) Cluster of laths where $\boldsymbol{b}_{S'}$ and $\boldsymbol{c}_{S'}$ take orthogonal $< 120 >_{Al}$ directions. Trace of $(230)_{Al} \| (011)_{S'}$ interface plane is indicated. (c) Detail of main interface along $\boldsymbol{b}_{S'}$ (and small step along $[100]_{Al}$) with unit cell and suggested map of atoms. The coherent main interface corresponds always with internal Al planes at z= 0, ½ in S' cell (buckled dotted lines). All distances are in nm.

(a)

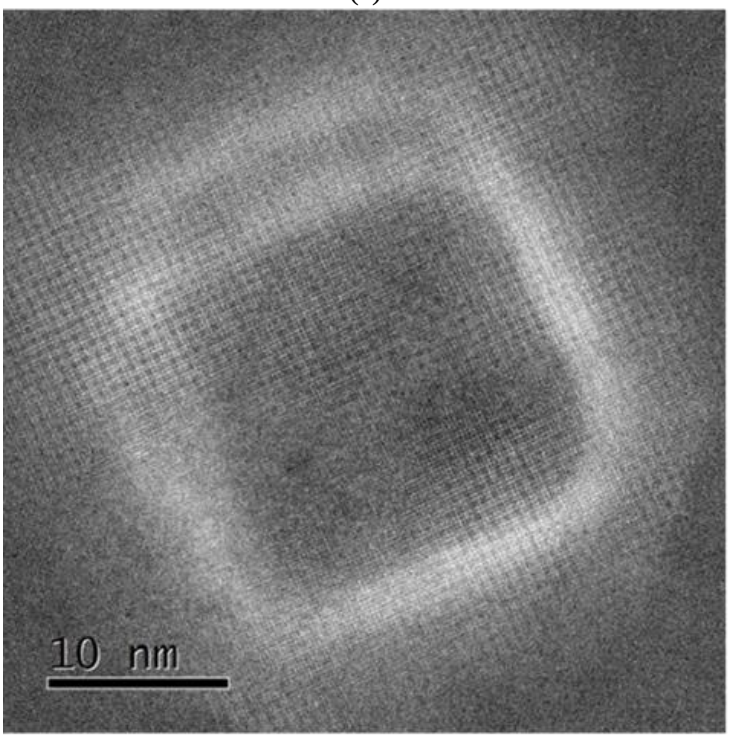

(b)

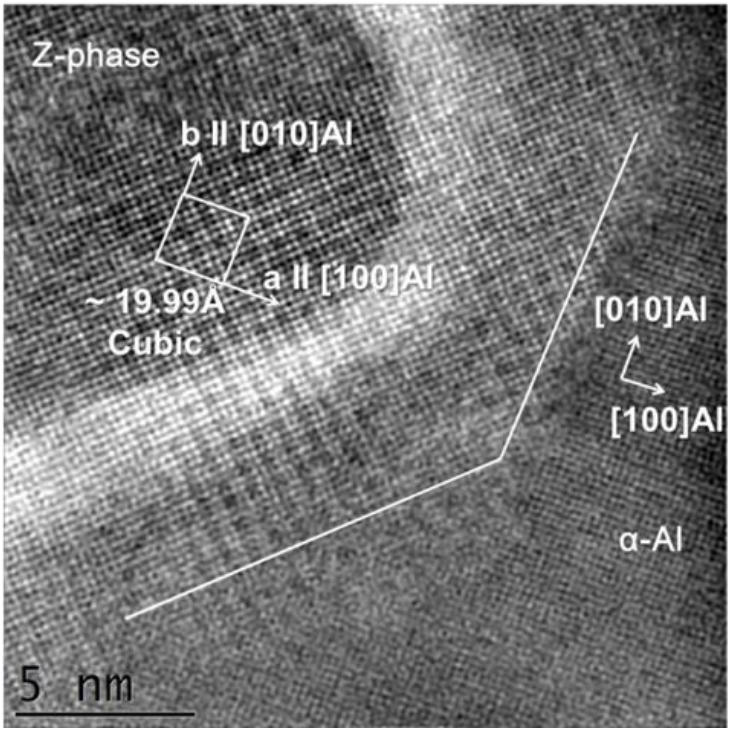

Fig. 2.13 HAADF-STEM images of the Z phase taken along $< 001 >_{Al}$ for the Base alloy aged for 950.4 ks at 443 K, showing that unit cells of Al and Z are parallel, i.e. $[100]_{Al}||[100]_{Z}$, $(001)_{Al}||(001)_{Z}$.

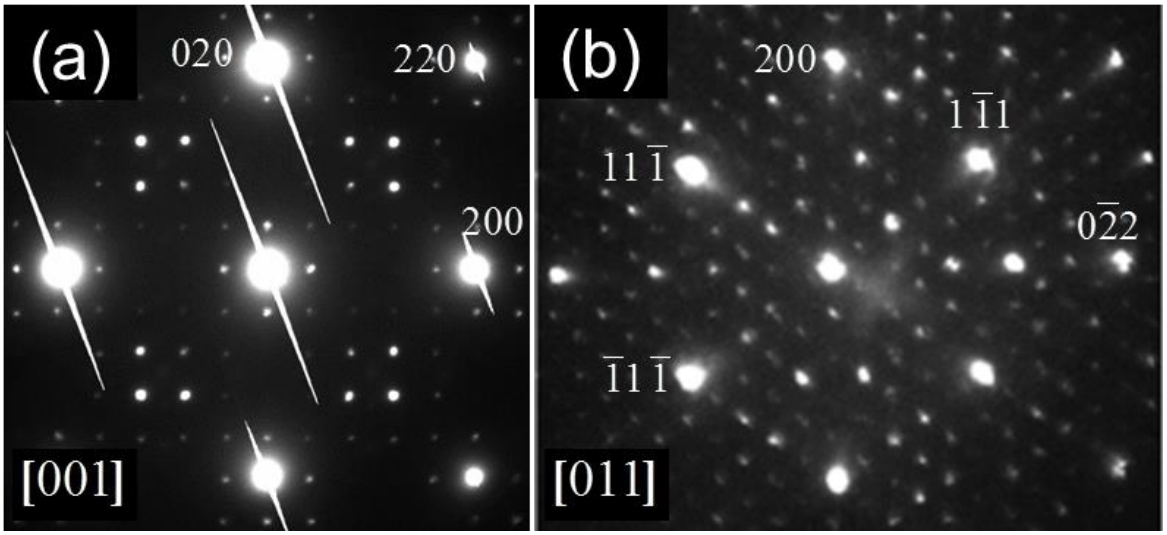

Fig. 2.14 Nano-beam diffraction patterns of large embedded rod-shaped fcc Z-phase in the Base alloy aged at 443K for 950.4 ks. The Z unit cell is parallel with Al, but 5 times larger: (a) $[001]_{Al,\,Z}$ projection along a rod, (b) $[110]_{Al,\,Z}$ projection perpendicular to rod.

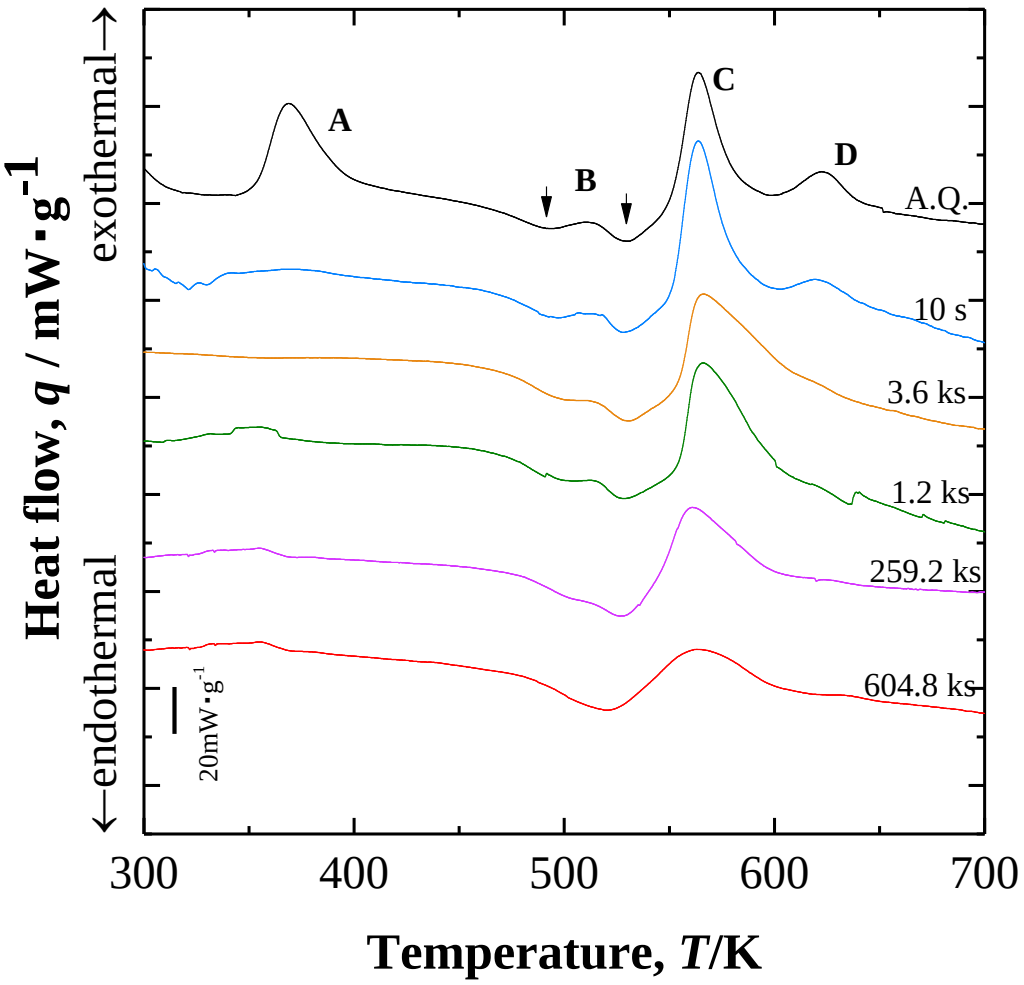

Fig. 2.15 DSC curves for the Base alloy aged at 443 K for various times. Heating rate is 10 K/ min.

Table 2.4 Isoconversion methods for activation energy analysis with typical sources of error [20.]

Method	Ref.	Expression	Main sources of error	Limit of accuracy, %†		Recommended use	Application
				Approx. (i) & (v)	Approx. (ii)–(iv)		
Ozawa	136, 137	$\ln \beta = -1{\cdot}0518 \frac{E}{RT_f} + C_2$	(i), (ii), (iv), (vi)	7	1	Not recommended due to inaccuracies; only to be used in conjunction with correction tables (*see* Flynn[150])	…
Boswell	138, 145	$\ln \frac{\beta}{T_f} = -\frac{E_a}{RT_f} + C_2$	(i), (ii), (iv), (vi)	4	1	Not recommended due to inaccuracies	…
Generalised Kissinger	131, 134	$\ln \frac{\beta}{T_f^2} = -\frac{E}{RT_f} + C_2$	(i), (ii), (iv), (vi)	0·7	1	Straightforward and popular method with good accuracy	E is slope of plot of $\ln(T_f^2/\beta)$ versus $1/RT_f$
Type B-1·95	120	$\ln \frac{\beta}{T_f^{1{\cdot}95}} = -\frac{E}{RT_f} + C_5$	(i), (ii), (iv), (vi)	0·4	1	Straightforward method with high accuracy	E is slope of plot of $\ln(T_f^{1{\cdot}95}/\beta)$ versus $1/RT_f$
Type B-1·92	120	$\ln \frac{\beta}{T_f^{1{\cdot}92}} = -1{\cdot}0008 \frac{E}{RT_f} + C_6$	(i), (ii), (iv), (vi)	0·25	1	Straightforward method with very high accuracy	E is slope of plot of $\ln(T_f^{1{\cdot}92}/\beta)$ versus $1{\cdot}0008/RT_f$
Starink	129	$\ln \frac{\beta}{T_f^{1{\cdot}8}} = -\frac{E_{slope}}{RT_f} + C_5$ $E = E_{slope}\left(1{\cdot}007 - \frac{1{\cdot}2E_{slope}}{10^5 \text{ kJ mol}^{-1}}\right)^{-1}$	(i), (ii), (iv), (vi)	0·2	1	Very high accuracy if T_f can be determined with very high accuracy (to about 0·1 K)	First obtain E_{sl} from slope of plots of $\ln(T_f^{1{\cdot}8}/\beta)$ versus $1/RT_f$; then obtain E from correction factor equation
Lyon method	122	$\frac{d(\ln \beta)}{d(1/T_f)} \cong -\left(\frac{E}{R} + 2T\right)$	(i), (ii), (iv), (vi)	0·7	1	An indirect method, with good accuracy	First obtain slope of plots of $\ln(\beta)$ versus $1/T_f$; then use average T to obtain E
Kissinger peak reaction rate	131, 133	$\ln \frac{\beta}{T_p^2} = -\frac{E_a}{RT_p} + C_2$	(i), (ii), (iv), (v), (vi)	1·2	0·5	Recommended if T_f values cannot be determined accurately due to overlapping heat effects. Good accuracy	E is slope of plots of $\ln(T_p^2/\beta)$ versus $1/RT_p$
Type B-1·95 peak	120	$\ln \frac{\beta}{T_p^{1{\cdot}95}} = -\frac{E}{RT_p} + C_2$	(i), (ii), (iv), (v), (vi)	1·1	0·5	Recommended if T_f values cannot be determined accurately due to overlapping heat effects. High accuracy	E is the slope of plots of $\ln(T_p^{1{\cdot}95}/\beta)$ versus $1/RT_p$
Friedman	139, 38	$\ln\left(\frac{d\alpha}{dT}\beta\right) = -\frac{E_a}{RT_f} + C$	(ii), (iv), (vi)	0	1·2	Recommended only if $d\alpha/dT\,(=q)$ values can be determined very accurately (typically an accuracy better than 0·2% is required[120])	E is the slope of plots of $-\ln(\beta d\alpha/dT)$ versus $1/RT_f$
Li and Tang	140	Integral formulation based on the Friedman method.	(ii), (iv), (vi)	0	1·2	Recommended only if $d\alpha/dT\,(=q)$ values can be determined very accurately	Numerical integration method (*see* Ref. 140)

*T_f is the temperature at a fixed amount transformed and T_p is the temperature at maximum reaction rate.
†Limit of accuracy assuming a quadratic summation of errors due to sources given; error calculations indicated in Refs. 120, 148, 149, 151, 152; error sources (i) and (v) are taken as the maximum encountered for $15<y<60$; error sources (ii)–(iv) are estimated by assuming 1% accuracy in determination of $d\alpha/dt$, 0·5 K accuracy in determining T_f, 0·25 K accuracy in determining T_p, range of T_f, T_p taken as 50 K, with reactions occurring around 500 K.

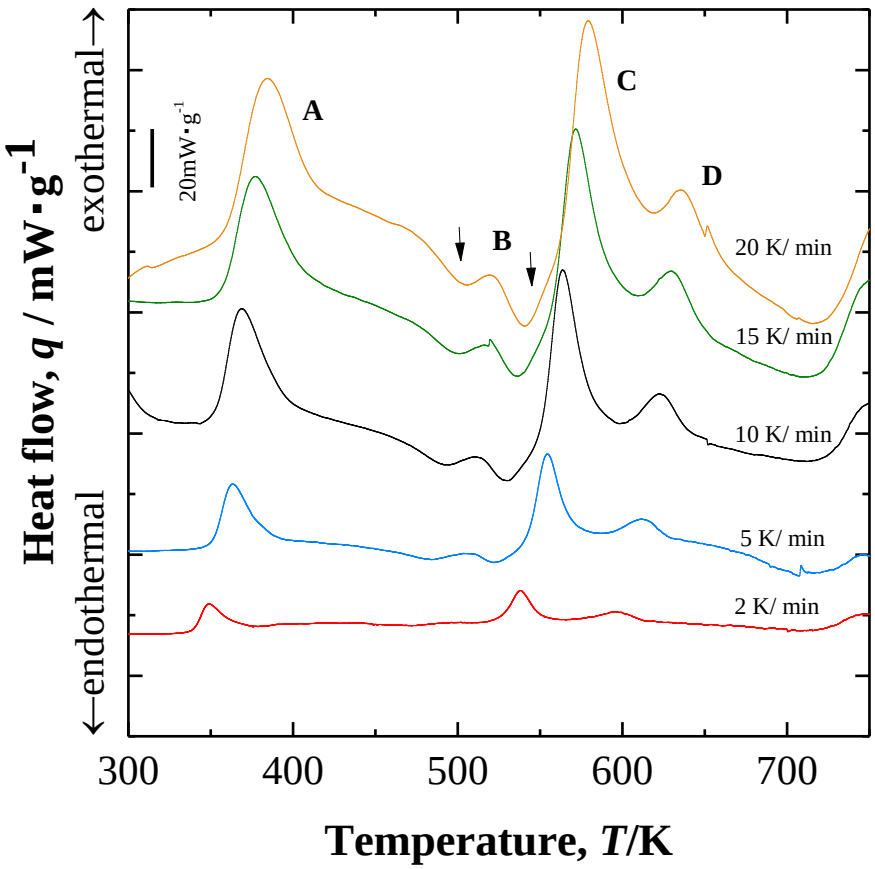

Fig. 2.16 DSC curves for the Base alloy with different heating rate from 5 to 20 K/min.

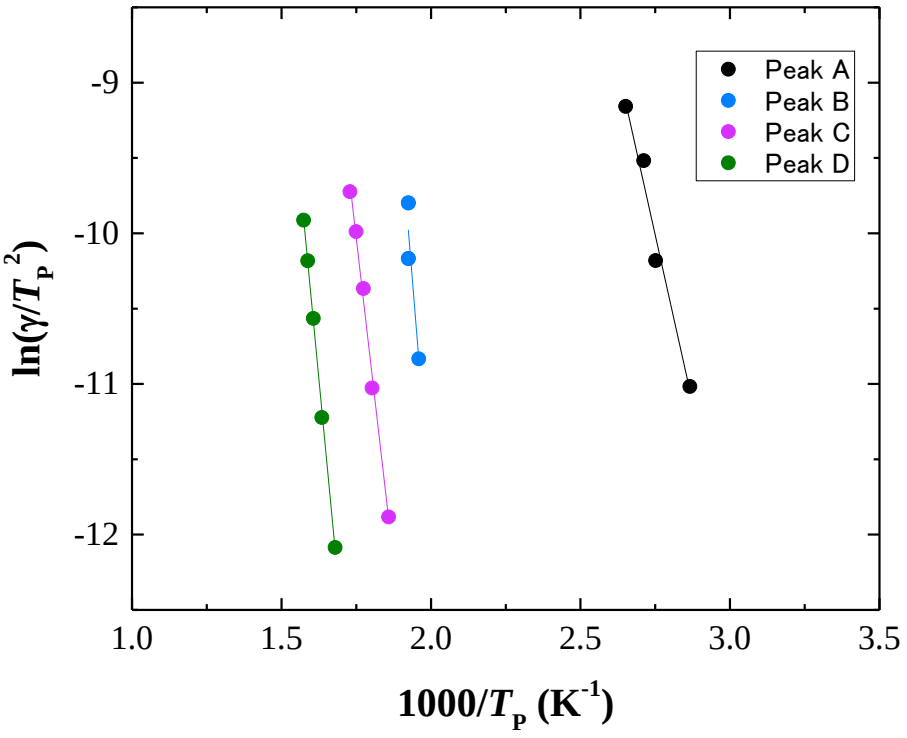

Fig. 2.17 $\ln(\gamma/T_P^2)$ as a function of $1000/T_P$ of exothermic peaks observed in DSC curves for the Base alloy showing the activation energy obtained by using Kissinger's method.

Table 2.5 Activation energy values obtained by Kissinger's method.

Activation energy, kJ/mol			
peak A	peak B	peak C	peak D
73.9	122.9	142.9	173.3

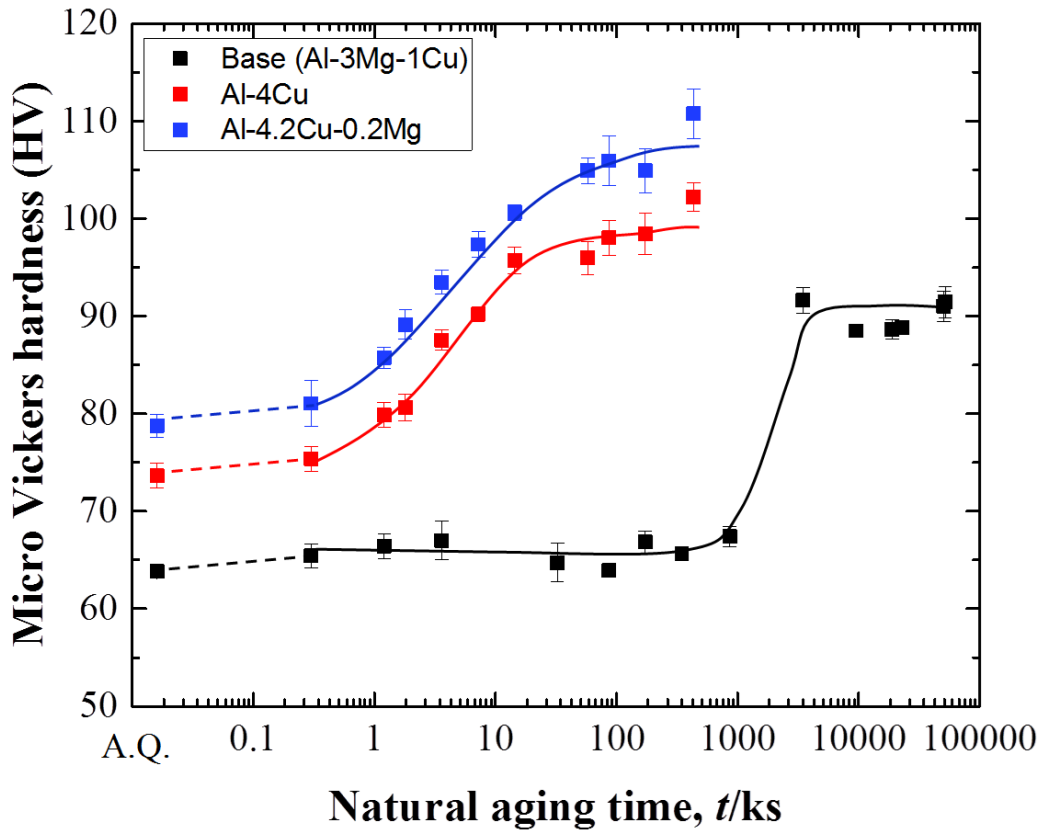

Fig. 2.18 Hardness changes during natural aging for the Base, Al-4Cu and Al-4.2Cu-0.2Mg alloys.

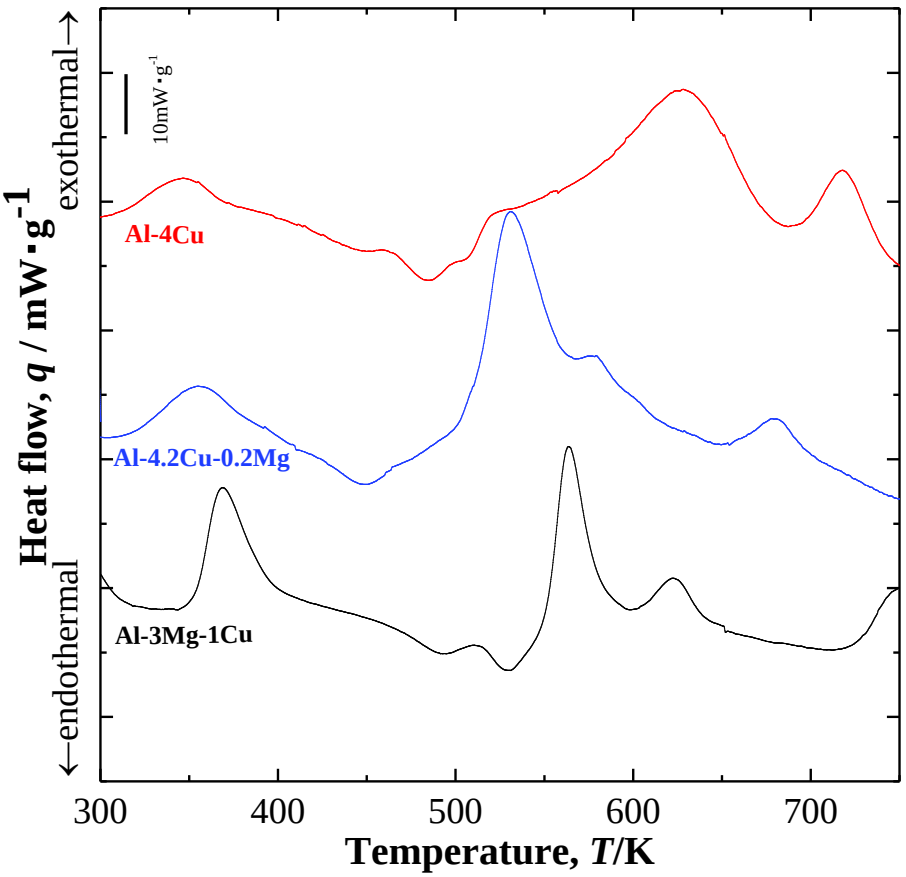

Fig. 2.19 DSC curves for the Base, Al-4Cu and Al-4.2Cu-0.2Mg alloys in the A.Q. state.

Chapter 3

Evolution of Nanostructures and Role of Vacancies During Initial Stage of Aging in an Al-Mg-Cu Alloy

3.1 Introduction

The early stage of the precipitation sequence is still under debate despite the number of papers dealing with the Al-Cu-Mg alloy system. During the initial decomposition, solute clusters form and the concentration of quenched-in vacancy control the rate of diffusion of solute atoms from the matrix to the clusters. As shown in the previous chapter, the hardness and electrical resistivity increases very rapidly during aging at 443 K in Al-Mg-Cu alloys. DSC results suggests that solute clustering occur very rapidly since the exothermic peak disappeared after aging at 443 K for 10 s. Therefore, the aim of this chapter is to clarify the formation behavior of solute clusters and the role of quenched-in vacancies during the initial decomposition.

In order to investigate the microstructural evolution and vacancy behavior in the high purity Al-3Mg-1Cu alloy (Base alloy), various techniques such as HAADF-STEM, three dimensional atom probe (3DAP), and positron annihilation spectroscopy (PAS) will be applied. By HAADF-STEM investigation, even single atoms or small clusters consisting of few atoms can be resolved. HAADF-STEM images directly reflect the distributions of heavier constituent such as Cu. Since the composition of investigated alloy contains Cu, Cu atoms will show a bright contrast in HAADF-STEM images. 3DAP can resolve both the three-dimensional position and chemical identity of individual atoms. Statistical analysis such as frequency distribution and contingency table method will be applied to analyze the obtained data. Through the statistical analysis, atoms are divided into small blocks containing a fixed number of atoms. The frequency distribution and contingency table analysis are used to investigate the single solute species interaction (like-atom clustering) and two solute species interaction (unlike-atom clustering), respectively. For PAS, the two main experimental techniques, positron annihilation lifetime spectroscopy (PALS) and coincidence

Doppler broadening (CDB) will be conducted in order to detect vacancy and identify the chemistry of the environment in contact with vacancies.

3.2 Experimental Procedure

3.2.1 Alloy Composition

The chemical composition of the alloy utilized in this chapter is shown in **Table 3.1**. The composition is the same as the high purity Al-3Mg-1Cu alloy in the previous Chapter.

3.2.2 Heat Treatment

Samples were solution treated in a salt bath at 793 K and kept for 3.6 ks, followed by quenching in ice-water and held for 60 s. The aging treatment was carried out in an oil bath at 443 K.

3.2.3 HAADF-STEM

Precipitate structures for the Base alloy aged for 0.06 ks at 443 K were investigated by high-resolution HAADF-STEM using a spherical aberration (Cs) probe-corrected JEOL ARM 200F STEM operated at 200 kV. The nominal probe size was 0.08 nm and the inner collector angle was 50 mrad. In order to reduce contamination all specimens were treated for a few minutes in a plasma cleaner (Fischione 1020) before HAADF-STEM observations. To enhance contrast, high frequency noise of the HAADF-STEM images were removed by the fast Fourier transform (FFT) filtering using a circular band pass mask.

3.2.4 Three Dimensional Atom Probe (3DAP)

Specimens for APT analysis were prepared by cutting small rods and drawing (1mm×1mm ×50mm). The specimens were electropolished using the standard two-stage method. Initial electropolishing was performed using a double layer technique with a solution of 25% perchloric acid in acetic acid at 10–20 V DC at RT. This was followed by electropolishing in 2% perchloric acid and 98% 2 -butoxyethanol at 10V DC at RT. APT analysis was performed using a Local Electrode Atom Probe (LEAP^{TM}) manufactured by CAMECA instruments Inc..

The analyses were performed at a specimen temperature of 30K, a voltage pulse fraction (pulse voltage/steady-state voltage) of 20%, and a pressure in the specimen chamber below10^{-8} Pa. Reconstruction of APT data was carried out using IVAS software 3.6 (CAMECA Instruments Inc.). Two separate experimental runs were carried out for each condition, and consistent results were obtained between the runs. The obtained data was examined by following three methods, such as frequency distribution, contingency table and radial distribution function methods.

I. Frequency Distributions

Information on the distribution of solutes in the data can be determined with a frequency distribution. The frequency distribution is created by dividing the atoms into small blocks containing a fixed number of atoms [1]. A plot of the total number of data-blocks containing a given number of solute atoms is made against the atomic fraction of solute atoms present. The experimental frequency distribution can be compared directly to the binomial (random) distribution. The expected number of blocks with n solute atoms, $f(n)$, is given by

$$f(\mathrm{n}) = Np_B(n) = N\frac{n!}{n!(n_b-n)!}\, c_A^n\, (1-c_A)^{(n_b-n)} \qquad (3.1)$$

where, N is the total number of blocks, p_B is the probability of detecting n solute atoms in blocks containing n_b atoms, and c_A is bulk concentration. The binomial distribution, $f(n)$, is the theoretical distribution under the assumption that solute A atoms are randomly distributed throughout the obtained APT data and there is no interaction between atoms. Deviation from the theoretical distribution can suggest the incidence of nanostructure such as solute clustering. The deviation can be quantified by means of χ^2 statistics,

$$\chi^2 = \sum_{n=0}^{n_b} \frac{(e(n)-f(n))^2}{f\,(n)} \qquad (3.2)$$

where $e(n)$ is the number of blocks containing n solute atoms which is measured experimentally. The limitation for the χ^2 test is a dependence on the size of the data set. The

value of χ^2 will increase with increasing the total number of blocks ,*N*. In order to normalize χ^2 with respect to *N*, Pearsons coefficient [2], μ, can be used as a measure of association,

$$\mu = \sqrt{\frac{\chi^2}{N+\chi^2}} \qquad 0 \leq \mu \leq 1 \tag{3.3}$$

where μ=0 indicates a random distribution and 1 indicates a complete association. By utilizing μ, direct comparison of the solute-solute clustering in two different data sets can be possible.

II. Contingency Tables

The contingency table is a 2D frequency distribution charting coincident occurrences of two solute elements across small blocks of the data [2]. The composition of the two solute elements are compared with those expected from a random distribution. **Table 3.2** shows general form of a two-dimensional r × c contingency table.

The random table is created from the marginal totals of the experimental table where the estimates of the expected frequencies, e_{ij}, is given in dot notation by

$$e_{ij} = \frac{n_{i.}n_{.j}}{n_{..}} \tag{3.4}$$

where $n_{..}$ is the total number of observations and the row (r) and column (c) marginals are defined as

$$n_{i.}\sum_{j=1}^{c} \quad \text{and} \quad n_{.j}\sum_{i=1}^{r} \tag{3.5}$$

respectively. This approach is based on a χ^2 analysis, where the value of χ^2 is calculated from the divergence of the experimental contingency table from a random (expected) table of frequencies generated from the assumption of no association between the occurrences of the solute species.

$$\chi^2 = \sum_{i=1}^{r}\sum_{j=1}^{c}\frac{(n_{ij}-e_{ij})^2}{e_{ij}} \tag{3.6}$$

The chi-squared coefficient is used to normalize the N dependence of χ^2. While frequency distribution analysis is used to single solute species interaction (like-atom clustering), contingency table analysis is used to test for two solute species interaction (unlike-atom clustering).

III. Radial Distribution Function (RDF)

RDF analysis was carried out on the obtained APT data. RDF is a characterization of the average local arrangement of solute atoms within a solid solution to identify significant spatial- and chemical-correlations [3]. An RDF at a given radial distance, r, is defined as the average concentration distribution of component *i* around a given solute species, *X*, $< C_i^X \text{ (r)} >$, normalized to the overall concentration of *i* atoms, C_i^0, in the sampled volume,

$$\text{RDF} = \frac{< C_i^X \text{ (r)} >}{C_i^0} = \frac{1}{C_i^0} \sum_{k=1}^{N_X} \frac{N_i^k(r)}{N_{tot}^k(r)} \qquad (3.7)$$

where $N_i^k(r)$ is the number of *i* atoms in a radial shell around the *k*th *X* atom that is centered at *r*, $N_{tot}^k(r)$ is the total number of atoms in this shell, and N_X is the number of *X* atoms in this volume. **Figure 3.1** shows the schematic illustration of the concept of radial distribution function [3]. Only the RDFs for $r \geqq 0.2$ nm will be presented since physical interpretation at smaller r is difficult due to possible ion trajectory effects.

3.2.5 Positron Annihilation Spectroscopy (PAS)

The two main experimental techniques of PAS, positron annihilation lifetime spectroscopy (PALS) and coincidence Doppler broadening (CDB) were utilized to investigate the decomposition phenomena during aging, especially evolution of the vacancy-like defects.

I. Positron Annihilation Lifetime Spectroscopy (PALS)

The samples for the PALS were prepared as 1 cm × 1 cm and 1.3 cm thickness. The surface of these samples were roughly polished with SiC paper. One pair of samples were prepared

for the PALS measurements since the technique is non-destructive and the experiments can be repeated on the same pair of the samples after necessary heat treatment. A 0.74 MBq sealed source of ^{22}NaCl deposited onto two Kapton foils (7.5 μm thick) was sandwiched between the pair of samples. The lifetime spectra were taken at room temperature with a fast-fast coincidence system (~250 ps FWHM time resolution) to gather about 10^6 counts. The obtained data was analyzed with the Positronfit program [4]; after subtracting the source + Kapton contribution, good fitting was always obtained with a single component. The positron mean life τ can be an average over two or more unresolved components. The change in the average value of τ occurring in an alloy after a heat treatment may be due either to a change in the concentration of vacancies or to a modification of the average chemical environment of the vacancies.

II. Coincidence Doppler Broadening (CDB)

More specific data regarding the local chemical composition can be obtained by CDB spectroscopy. CDB measurements were taken at room temperature by means of two hyperpure Ge gamma detectors (90% of relative efficiency) coupled to a multiparametric pulse analyzer. The samples were arranged in the sample-source-sample sandwich geometry. Background rejection was achieved by requiring time coincidence within a window of 300 ns and fulfillment of the energy conservation condition $|E_1 + E_2 - 2m_0c^2| < 2.1$ k eV, where E_1 and E_2 are the energies measured by the two detectors, respectively. The component along the axis joining the two detectors of the momentum of the annihilating pairs is given by

$$p_L = \frac{E_1 - E_2}{c} \tag{3.8}$$

Ten million counts were collected in each spectrum. The analysis of the momentum spectra ρ was carried out [5,6], by fitting a linear combination of momentum spectra measured in the same experimental condition for pure elements, as given by the following function:

$$\rho_{fit} = (1 - F_{trap})\rho_{Al}^{bulk} + F_{trap}(C_{Al}^{v}\rho_{Al}^{v} + C_{Mg}^{v}\rho_{Mg}^{v} + C_{Cu}^{v}\rho_{Cu}^{v}) \quad (3.9)$$

where F_{trap} is the trapping fraction (relative number of positrons that are trapped and annihilated in vacancy-like defects) and C_{Al}^{v}, C_{Mg}^{v} and C_{Cu}^{v} are the fractional concentrations. ρ_{Al}^{bulk} is the momentum distribution for free positrons annihilating in the alloy matrix. ρ_{Al}^{bulk} is the experimental momentum distribution measured in well-annealed pure Al. $\rho_{Al}^{v}, \rho_{Mg}^{v}$ and ρ_{Cu}^{v} are the distributions for positrons annihilated in the alloy constituents (Al, Cu and Mg) as measured with severely cold worked samples after subtracting the contribution of annihilations with free positrons [7]. The momentum spectra of the annihilation radiation will be described in terms of the ratio-difference function:

$$\Delta = \frac{1-\rho_{Al}^{bulk}}{\rho_{Al}^{bulk}} \quad (3.10)$$

ρ_{Al}^{bulk} is the CDB spectrum measured for bulk Al (well-annealed pure Al). The ratio CDB differences curves relative to a reference material is called Δ curves. This representation is used in order to enhance the details of the spectra in the high-momentum region, which is most important for the identification of the chemical species in contact with vacancy-like defects. The symmetrical experimental curves have been folded around $p_L = 0$. The statistical noise has been reduced by averaging groups of three subsequent points from about 0.7 to 1.4 atomic momentum units and of six points above 1.4 atomic units. **Figure 3.2** shows the reference momentum spectra obtained for pure well-annealed Al, Mg and Cu [8]. These spectra were obtained under the condition of saturated positron trapping and used as reference spectra when the fitting procedure was applied through **Eq. (3.9)**. The main contribution to p_L comes from the electron motion. For pure Cu, a strong contribution from annihilation with fast electrons (3d and core), giving rise to the broad peaks at ±2 atomic units. The depression of Δ at low momentum is due to the smaller probability of annihilation with free electrons as compared to Al. On the other hands, Mg shows enhanced free-electron

annihilation with respect to Al in spite of the identical ($1s^2 2s^2 2p^6$) core structure. Positrons have a less opportunity to interact with the core electron of Mg. The peaks at ±1-1.5 atomic units are attributed to the different Fermi momentum of Mg (0.72 atomic unit) and Al (0.93 atomic unit) [9]. Thus, the shape of the "wings", broadened annihilation line is the "fingerprint" of the annihilation with alloy components, which can be used for evaluating the relative contribution of alloy components to annihilation in an alloy.

3.3 Results

3.3.1. HAADF-STEM Investigation for the Alloy Aged for 0.06 ks

Figure 3.3 shows a HAADF-STEM image for the Base alloy aged at 443 K for 0.06 ks. FFT of the HAADF-STEM image (**Fig. 3.3**) shows the same spots as the SADPs obtained for the specimen aged for 10.8 ks and 86.4 ks [**Fig. 2.10 (a), (b)**]. The spots in the FFT (**Fig. 3.3**) demonstrates the existence of some precipitates. As described in Chapter 2, Kovarik et al. [10] showed that the weak spots defining small squares between Al reflections including a central spot on the 110_{Al} positions as seen in **Fig. 3.3** are consistent with scattering from GPB zones. Based on the investigation for the GPB zones formed in an Al-3Mg-1Cu (wt %) alloy aged at 453 K for 86.4 - 345.6 ks, they concluded that GPB zones can be understood in terms of an agglomerate form comprising structural units arranged in up to four different orientations [11]. The notation for the structural units of the GPB zones are shown in **Table 2.3** in **Chapter 2**. The enlarged HAADF-STEM images for the Base alloy aged at 443 K for 0.06 ks are shown in **Fig. 3.4**. The microstructure seems to consist of a multitude of the unit of the GPB zone (yellow circles). Most of them are identified as half units of GPB zone (**Fig. 3.5**). An example of a single unit observed in **Fig. 3.4** is shown in **Fig. 3.6(a)**. Based on the atomic number Z-contrast which is proportional to $Z^{1.7\text{-}1.9}$, Cu atoms are identified easily in

Fig. 3.6(a). A red triangle defines a half of the unit of GPB zone. It is hard to identify the position of Mg atoms by Z-contrast, however an element map for the single unit can be deduced according to the [11] (**Fig. 3.6 (b)**). Columns correspond to the two Al planes z=0 and ½ (0.203 nm). A single unit (two half units) has a composition $Al_4Mg_6Cu_6$. Sometimes the center of a half unit can be occupied by Cu instead of Al, and in this case the composition becomes $Al_2Mg_6Cu_8$. The structure of the units are close to fcc-based structure of Al matrix. In the present study, the microstructure of the Base alloy after aging at 443 K for 0.06 ks consists of a multitude of the unit of the GPB zone and most of them are half of units (**Fig. 3.5**). The composition of those half units is possibly $Al_2Mg_3Cu_3$. This is the first direct observation of the structural units of GPB zone formed in the very early stage of aging. **Figure 3.7** is an example of the HAADF-STEM image of structural units of GPB zone with a dislocation line running from up left to down right. This figure indicates that those units might act as obstacles to dislocation motion and cause the rapid age-hardening in the initial aging stage.

3.3.2 3DAP Analysis

Figure 3.8 shows the 3DAP maps for the Base alloy aged at 443 K for (a) 0.06 ks and (b) 3.6 ks. Mg, Cu and Al atoms are rendered green, orange and blue respectively. The total number of atoms detected by 3DAP measurements are shown in **Table 3.4**. Since fine scale structures such as solute clusters have only subtle differences from the arrangement of solute atoms in matrix, the 3D reconstruction of the elemental maps are not useful to visually detect them. In **Fig. 3.8** it is not obvious that there is solute clusters of Cu and Mg atoms. Statistical analyses is conducted on the APT data sets in the following sections.

I. Frequency distributions

The ideal block size was chosen to be n_b=300 atoms per block using the method described in [2] with a minimum observation of 5 blocks per class. The observed frequency distributions

together with binomial (random) distributions for the investigated alloy aged for 0.06 ks are shown in **Fig. 3.9**. The observed distribution for Mg atoms is close to the random distribution [**Fig. 3.9 (b)**], however for Cu atoms [**Fig. 3.9 (a)**] the distribution is slightly different from random distribution. After aging for 3.6 ks, it becomes more clear that the number of blocks which has no Cu atoms (0 % Cu concentration) increases concomitant with the increase of the number of blocks with higher Cu concentration [**Fig. 3.10 (a)]**, while changes in the number of blocks for Mg atoms is small [**Fig. 3.10 (b)**]. It is suggested that there is a higher degree of Cu-Cu than Mg-Mg interactions. χ^2 values and degrees of freedom for Cu-Cu and Mg-Mg interactions obtained by frequency distribution analysis are shown in **Table 3.5**.

II. Contingency tables

The ideal block size was chosen to be n_b=300 atoms per block with a minimum observation of 5 blocks per tables, same as the frequency distribution analysis. χ^2 value and degree of freedom for Cu-Mg interactions obtained by contingency table analysis are shown in **Table 3.5**. As shown in **Table 3.4**, the total number of the blocks for each sample is different since the total number of the blocks depends on sample size (the total number of atoms detected). The value of χ^2 will increase with increasing the total number of blocks , *N*. In order to normalize χ^2 with respect to *N*, Chi-squared coefficient, μ, was calculated by using Eq. (3.3) (**Fig. 3.11**). The results indicates that significant Cu-Cu clustering compared to random distribution in both aging conditions. The levels of Mg-Mg and Cu-Mg clustering are similar and slightly increased as aging proceeds.

Fig. 3.12 demonstrates the effect of block size on μ value for Cu-Mg clustering. A small block size such as 50 or 100 seems to cause a loss of the finer aspects of the nanostructure. Since Cu content in the investigated alloy is small (Cu: 0.45 at %, Mg: 3.52 at %), the solute ordering present in this alloy is emphasized best by partitioning the data into large blocks

(n_b>200). As block size increases, the solute ordering in the investigated alloy seems to be overestimated. For this reason, in present study, the block size was chosen to be n_b=300.

III. Radial Distribution Function (RDF)

The result of RDF analysis is shown in **Fig. 3.13** and **Fig. 3.14**. Experimental values were standardized by using bulk concentration which is derived on the assumption that all atoms are randomly distributed and there are no correlation among the concentration distributions of solute species. Thus, the standardized RDF values become close to 1 if the atoms are uniformly distributed. **Figure 3.13** revealed that the Cu concentration around Cu atoms is apparently high in both aging conditions. It indicates the segregation of Cu atoms. On the contrary, the RDF value for the Mg concentration around Cu atoms is slightly above 1 and it increased a little as aging proceeds (**Fig. 3.13**). The segregation of Mg atoms is not remarkable in both aging conditions (**Fig. 3.14**). In consistent with the results obtained from the chi-squared coefficient, μ value, RDF results suggests that there is not strong correlation between Cu and Mg distributions comparing to strong Cu-Cu correlation.

3.3.3 Positron Annihilation

I. PALS

Figure 3.15 shows the evolution of the positron lifetime and hardness during aging at 443 K. The positron lifetime decreases rapidly in the initial, and then it remains almost constant for a long time. After the plateau stage, the positron lifetime increased again corresponding to the increase in hardness. A decrease in positron lifetime is generally observed during initial stage of decomposition of Al-Cu based alloys [12]. This phenomenon is attributed to the decrease of the fraction of positrons trapped in vacancies and also to the increasing concentration of Cu in contact with vacancies (Cu/vacancy clusters) [13]. The positron lifetime in pure Cu and Mg (v-Cu pairs and v-Mg pairs) amounts to 180 ps and 253 ps, respectively [14]. In **Fig. 3.15**, the lifetime values are higher than that of v-Cu pairs. Vacancy trapping at Mg would cause

the reduction of the lifetime drop. Thus, it is suggested that the presence of the Mg atoms associated with v-Cu complex during initial aging stage. The increase in positron lifetime after long term aging is due to the formation of incoherent or semi-coherent precipitates. Misfit interfaces provide new trapping sites where positrons can survive with small overlap to matrix [14].

II. CDB

Obtained Δ curves in **Fig. 3.16** show the CDB results presented as relative differences to the balk Al reference. For the A.Q. sample, a clear localization signal (± 1.3 atomic units) due to the positron confinement in vacancies and Cu fingerprint (wings at $|p_L| > 2$ atomic units) are observed, despite the low composition of Cu (0.45 at%) in the Base alloy. Mg fingerprint appears at ± 0.7 atomic units as sharp slopes. After aging for 0.06 ks and 3.6 ks, the Cu fingerprint becomes progressively stronger. In order to estimate the fraction of alloy components in contact with vacancies, the obtained curves are analyzed by fitting a linear combination of momentum spectra measured for the pure elements through Eq. (3.9). **Figure 3.17** shows the fitting results. There is an excellent agreement between the Δ curves corresponding to the fitting curves (red curves). **Table 3.6** summarizes the obtained fractional concentrations of the alloy components in contact with vacancies in the Base alloy for different aging conditions. F_{trap} is the trapping fraction of the positrons annihilated in the solute-vacancy clusters or nanoprecipitates. The complementary percentage (100 %- F_{trap}) represents the fraction of positrons annihilated into the matrix. According to the results, 54-60 % of positrons are trapped and annihilated in solute-vacancy clusters or nanoprecipitates in the Base alloy under the aging conditions. Fractional concentrations of the alloy components in contact with vacancies are also plotted in **Fig. 3.18**. The obtained results are summarized as follows,

(i) At A.Q. state, the amount of Cu is twice as large as that of Mg, suggesting the preferential attachment of the vacancies to Cu rather than Mg.

(ii) After aging for 0.06 ks, the amount of Al strongly decreases, the amount of Mg increases in about 50 % and the amount of Cu increases in 80 %.

(iii) After aging for 3.6 ks, the amount of Al slightly decreases, the amount of Mg stays constant, and the amount of Cu slightly increases.

It is revealed that the initial decrease in lifetime value (**Fig. 3.15**) is related to the strong increase in the Cu content and small increase of Mg surrounding vacancy-like defects. The vacancy-solute (Cu, Mg) complexes might be formed after short term aging.

3.4 Discussion

3.4.1 Evolution of Structural Units of GPB Zone

HAADF-STEM observation revealed that the microstructure of the Base alloy after aging at 443 K for 0.06 ks consists of a multitude of the structural units of the GPB zone and most of them are half of units. This is the first direct observation of those units formed in the early stage of aging. The weak fourfold arranged spots in the FFT (**Fig. 3.3**) are attributed to those structural units of GPB zone. As shown in **Fig. 3.5** and **Fig. 3.6**, the structure of observed structural units are close to fcc structure of the Al matrix. Recently, density functional theory (DFT) calculation for the GPB zone structure of the Base alloy [15] revealed that columns of GPB zones along $<100>_{Al}$ follows the simple arrangement principles. In order to create a half unit of GPB zone, only one vacancy is needed to change the height of the atomic column in the middle of the unit. Thus, it is favorable to form structural units of GPB zone for decomposition of the solute atoms. Solute clusters might be formed as the first forming solute inhomogeneities during aging. Formation of the structural units can be understood as

vacancy-induced rearrangement of solute atoms in clusters. The time required for the solute to travel some distance can be estimated by using a random walk equation,

$$t = x^2/6D \quad (3.11)$$

where D is diffusion coefficient, t is time and x is the diffusion distance. The diffusion coefficient can be calculated according to the following equation,

$$D = D_0 \exp(-Q/RT^{aging}) \quad (3.12)$$

where $D_0^{Cu} = 4.44 \times 10^{-5} m^2 s^{-1}$, $D_0^{Mg} = 1.49 \times 10^{-5} m^2 s^{-1}$, $Q^{Cu} = 133.9\ kJ/mol$, $Q^{Mg} = 120.5 kJ/mol$ [16]. For instance, the time to diffuse 1 nm for Cu and Mg atoms are only 23 s and 1.8 s, respectively. The size of a half unit of GPB zone is less than 1 nm. Thus, it is suggested that rearrangement of atoms, which means structural transition from solute clusters to the units, can be easily occurred within short term aging (0.06 ks at 443 K). Therefore, the exothermic peak A which was observed as the first thermal effect detectable during the DSC scan in the previous chapter (**Fig. 2.15**) is attributed to the formation of the structural units of GPB zone. However, according to the DSC investigation, the exothermic peak B which is associated with the formation of GPB zone appeared at around 510 K, which is far higher than that of the peak A (at around 360 K). The activation energy for the peak B (GPB zone) was obtained as 122.9 kJ/ mol (**Table 2.3**) which is close to the activation energies for diffusion of Cu and Mg in Al (133.9 kJ/ mol and 120.5 kJ/ mol, respectively). In contrast, the activation energy for the peak A was 73.9 kJ/ mol which is the activation energy for migration of (mono) vacancies (about 60 kJ/mol) in pure Al. Thus, it is suggested that the kinetics of the formation of the structural units of GPB zone is controlled by the migration of vacancies. The transition of the fcc-based structural units to the structure of GPB zones is controlled by the diffusion of solute atoms (Cu and Mg). The structural units of GPB zone observed in the present study can be identified as the structural units with one-dimensional translational periodicity. The GPB zone is an agglomeration of those units. It is indicated that

the formation of the structural units of GPB zone is energetically favorable to form from the solid solution, although it takes time to transform into the GPB zone, results in the plateau stage where the hardness, electrical resistivity and positron lifetime remain almost constant for the long time aging. According to the TEM investigation, no GPB zones were directly confirmed until the end of the plateau stage. Thus, the plateau stage can be understood as the transition period for the growth of the structural units.

Figure 3.19 shows the schematic illustration for the formation behavior of the structural units of GPB zone and zones during aging. Based on the obtained results, it is proposed that the rapid age-hardening is attributed to the formation of the structural units of GPB zone and the plateau stage is associated with the transition period from structural units to GPB zones.

3.4.2 Role of Vacancies, Cu and Mg Atoms

In many studies, it has been considered that the activation energy for Mg diffusion in an Al alloy is lower than that for Cu diffusion. It would indicate that Mg-Mg clusters are formed as the first type of solute clusters followed by Cu-Mg and Cu-Cu clusters. However, our 3DAP data clearly suggests that Cu aggregates are formed preferentially after short term aging. Although it is difficult to specify the actual composition of the structural units of GPB zone formed after aging at 443 K for 0.06 ks, it is undoubtedly true that nanostructures associated with Cu aggregates are formed after short term aging based on HAADF-STEM images. This result is in consistent with the formation of Cu aggregates indicated by 3DAP results.

In a fcc structure, one atomic site has 12 first neighbour atoms. Therefore, around a vacancy-like defect there are 12 first neighbor atoms. The results of the fractional concentrations of the alloy component in contact with vacancies C_i (**Table 3.6**) can be roughly interpreted as follows:

$$\left(C_{Al} = \frac{N_{Al}}{12}, C_{Mg} = \frac{N_{Mg}}{12}, C_{Cu} = \frac{N_{Cu}}{12} \right) \quad (3.13)$$

where, N_{Al}, N_{Mg} and N_{Cu} are the average number of Al, Mg and Cu atoms around a vacancy.

(i) Aging after 0.06 ks: Around a vacancy, there approximately are 2 Mg atoms, 5 Cu atoms and the rest are Al atoms.

(ii) Aging after 3.6 ks: Around a vacancy, there approximately are 2 Mg atoms, 6 Cu atoms and the rest are Al atoms.

Generally, PAS data give no direct information on the size or shape of the structural or chemical inhomogeneity associated with a vacancy [17]. However, the results above clearly indicates the formation of Cu-rich structures associated with a vacancy. The preferential attachment of the vacancies to Cu rather than Mg should be also noted.

Marceau et al. reported that in binary Al-1.1Cu (at %) alloy, the trapping fraction of the positrons annihilated in the solute-vacancy clusters or nanoprecipitates, F_{trap}, strongly decreased after aging for 0.06 ks at 150 ℃ [18], suggesting a substantial reduction in residual vacancy supersaturation. In the present study, F_{trap} stay constant during aging. Thus, the role of Mg atom is to retain the quenched-in vacancies and stabilize them during aging to promote the formation of vacancy-solute (Cu, Mg) complexes. 3DAP results suggested that Mg atom is a minority component of the nanostructure formed in the initial stage of aging, although HAADF-STEM identified the formation of the structural units of GPB zone consisted of Cu and Mg atoms.

In the next Chapter, the effect of the different Cu, Mg compositions on the age-hardening behavior will be investigated in order to characterize the role of Cu and Mg atoms during the initial decomposition.

3.5 Conclusions

1. HAADF-STEM investigation for the Base alloy age at 443 K for 0.06 ks revealed that the microstructure consists of a multitude of the unit of the GPB zone. Most of them were identified as half units of GPB zone. Those structural units of GPB zone might act as obstacles to dislocation motion and cause the rapid age-hardening during the initial aging stage. This is the first direct observation of the structural units of GPB zone which form in the initial stage of aging.
2. 3DAP data analysis clarified that there is not strong correlation between Cu and Mg distributions comparing to the strong Cu-Cu correlation. From RDF results, the Cu concentration around Cu atoms is apparently high after aging at 443 K for 0.06 and 3.6 ks.
3. PAS investigation clarified that the initial decrease in the lifetime value is related to the strong increase in the Cu content surrounding vacancy-like defects. There is a preferential attachment of the vacancies to Cu rather than Mg.

References

1) Miller MK. 2000. Atom probe tomography: Analysis at the atomic level. New York. Kluwer Academic/Plenum Publisher.

2) M. P. Moody, L.T. Stephenson, P.V. Liddicoat, and S.P. Ringer, Microscopy Research and Technique 70 (2007) 258–268.

3) M.K. Miller and R.G. Forbes, Atom-Probe Tomography: The Local Electrode Atom Probe. New York. Springer Science+Business Media (2014).

4) P. Kirkegaard, N.J. Pedersen and M. Eldrup: PATFIT-88 Risø Nat. Lab. (1989), M-2740.

5) R. Ferragut, A. Dupasquier, C.E. Macchi, A. Somoza, R.N. Lumley, I.J. Polmear, Vacancy–solute interactions during multiple-step ageing of an Al–Cu–Mg–Ag alloy, Scr. Mater. 60 (2009) 137–140.

6) M. Massazza, G. Riontino, A. Dupasquier, P. Folegati, R. Ferragut, A. Somoza, Secondary ageing in Al–Cu–Mg, Philos. Mag. Lett. 82 (2002) 495–502.

7) R. Ferragut, Atomic fraction around defects associated with nanoparticles in Al–Cu–Mg alloys, Physica B 407 (2012) 2676–2683.

8) C. Macchi, A. Tolley, R. Giovachini, I.J. Polmear, A. Somoza: Acta Materialia 98 (2015) 275–287.

9) N.W. Ashcroft and N.D. Mermin, Solid State Physics, Saunders College, Philadelphia (1976) 38.

10) L. Kovarik, P.I. Gouma, C. Kisielowski, S.A. Court and M.J. Mills, Acta Mater. 52 (2004) 2509-2520.

11) L. Kovarik, S. A. Court, H. L. Fraser, M. J. Mills, Acta Mater.56 (2008) 4804-4815.

12) A. Dupasquier, P. Folegati, N. de Diego, and A. Somoza, J. Phys.: Condens. Matter 10, 10 409 (1998).

13) A. Somoza, A. Dupasquier, I.J. Polmear, P. Folegati and R. Ferragut: Phys. Rev. B 61 (2000) 14454-14463.

14) G. Dlubek: Mater. Sci. Forum 13-14 (1987) 11-32.

15) S. J. Andersen, C. D. Marioara, J. Friis, R. Bjørge, Q. Du, I.G. Ringdalen, S. Wenner, E. A. Mørtsell, R. Holmestad, T. Saito, J. Røyset, O. Reiso, Materials Science Forum 461-470 (2016) 877.

16) Yong Du, Y.A. Chang, Baiyun Huang, Weiping Gong, Zhanpeng Jin, Honghui Xu, Zhaohui Yuan, Yong Liu, Yuehui He, F.-Y. Xie, Materials Science and Engineering A363 (2003) 140–151.

17) A. Somoza, M. P. Petkov and K. G. Lynn, Physical Review B 65 (2002) 094107.

18) R.K.W. Marceau, G. Sha, R. Ferragut , A. Dupasquier, S.P. Ringer, Acta Materialia 58 (2010) 4923–4939.

Table 3.1 Chemical composition of the investigated alloy.

(wt %)

Sample	Mg	Cu	Si	Fe	Ti	Al
Base alloy	3.04	1.01	0.01	0.01	0.00	Bal.

Table 3.2 General form of a two-dimensional r × c contingency table.[1)]

Experimental values

		Columns (Variable B)				
		1	2	•	c	total
Rows	1	n_{11}	n_{12}	•	n_{1c}	$n_{1\bullet}$
	2	n_{21}	n_{22}	•	n_{2c}	$n_{2\bullet}$
Variable	•	•	•	•	•	•
A	r	n_{r1}	n_{r2}	•	n_{rc}	$n_{r\bullet}$
	total	$n_{\bullet 1}$	$n_{\bullet 2}$	•	$n_{\bullet c}$	$n_{\bullet\bullet}$

Estimated values

		Columns (Variable B)				
		1	2	•	c	total
Rows	1	e_{11}	e_{12}	•	e_{1c}	$e_{1\bullet}$
	2	e_{21}	e_{22}	•	e_{2c}	$e_{2\bullet}$
Variable	•	•	•	•	•	•
A	r	e_{r1}	e_{r2}	•	e_{rc}	$e_{r\bullet}$
	total	$e_{\bullet 1}$	$e_{\bullet 2}$	•	$e_{\bullet c}$	$e_{\bullet\bullet}$

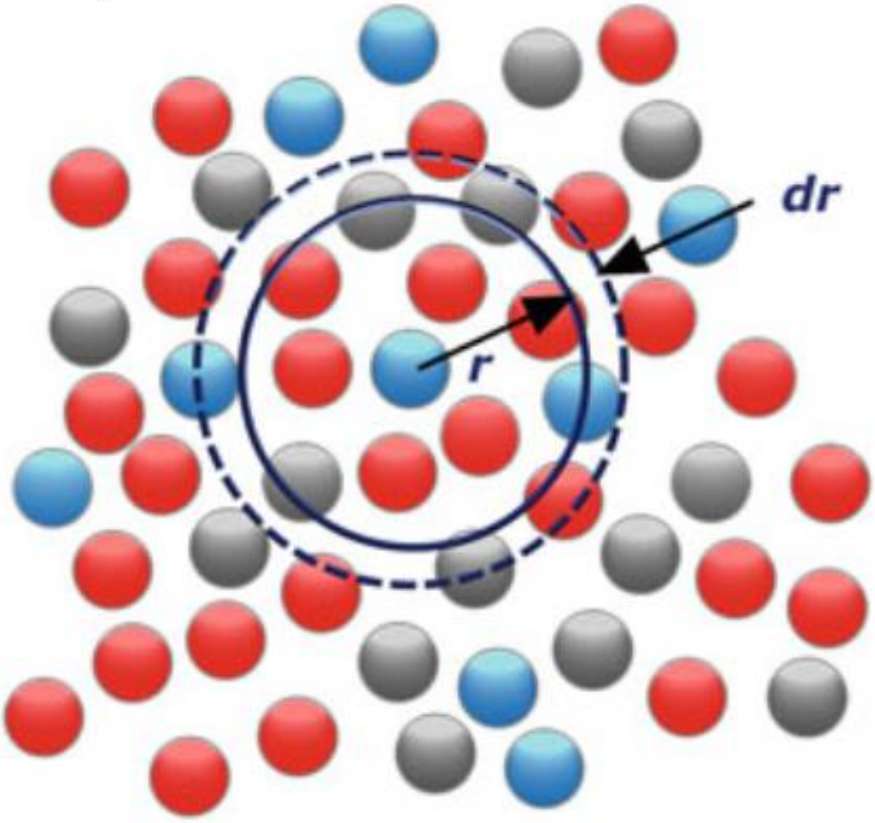

Fig. 3.1 Schematic illustration of the concept of radial distribution function.[3)]

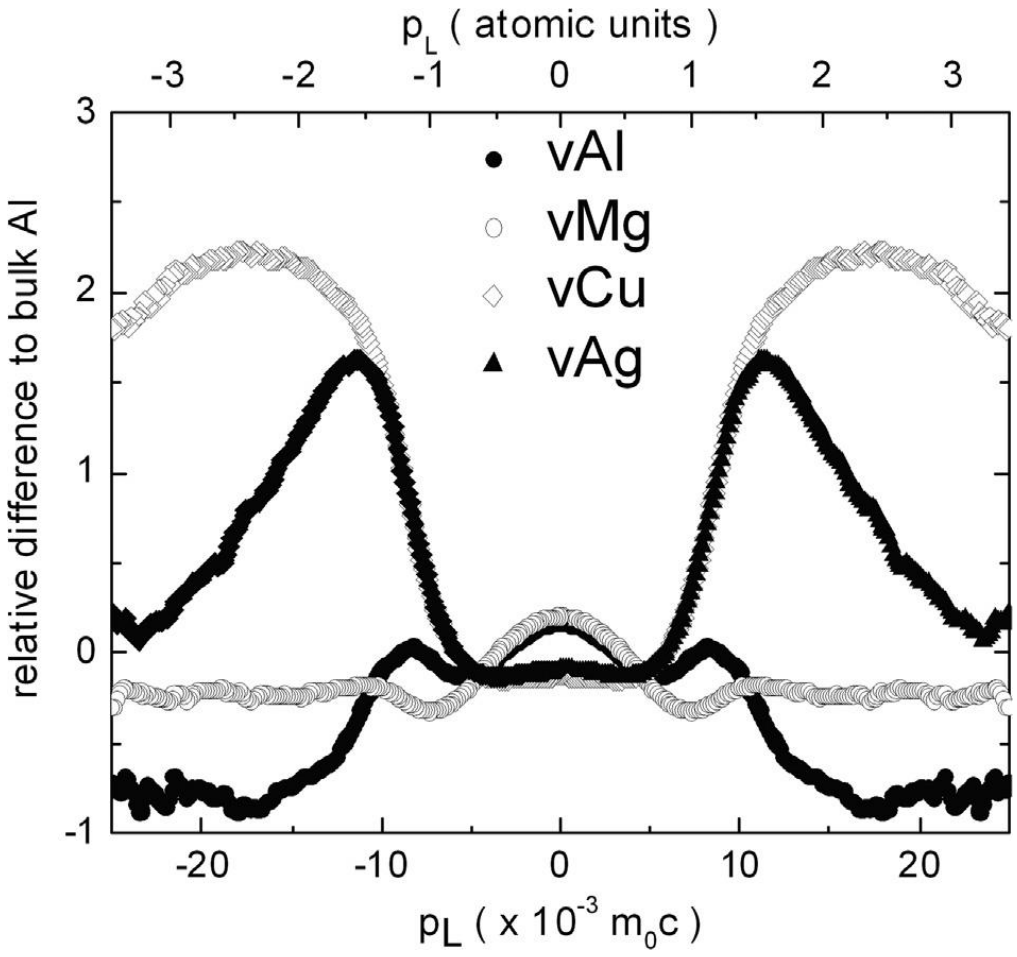

Fig. 3.2 The reference momentum spectra obtained for pure well-annealed Al, Mg and Cu.[8)]

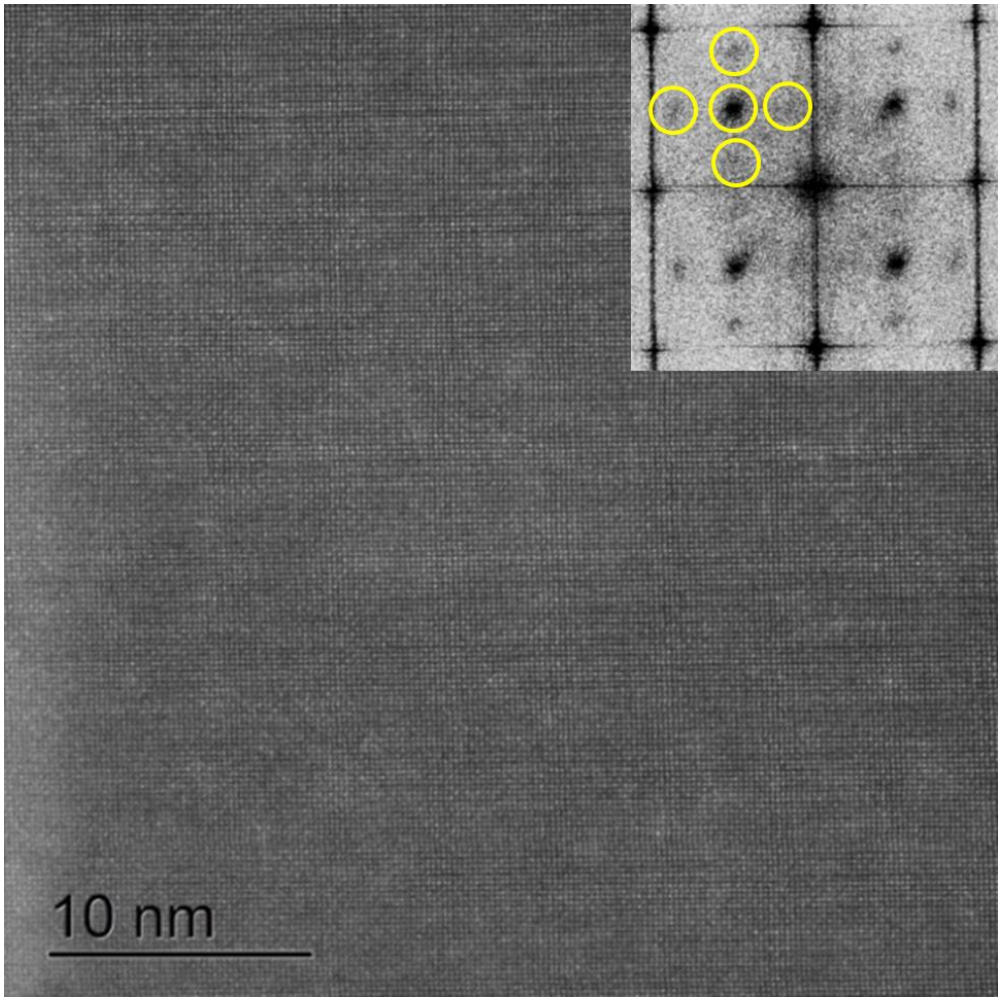

Fig. 3.3 HAADF-STEM image for the Base alloy aged at 443 K for 0.06 ks. FFT shows the same spots as the SADPs obtained for the specimen aged for 10.8 ks and 86.4 ks [Fig. 2.10 (a), (b)]

Table 3.3 Notation for the "structural units" of the GPB zone.[11)]

Half unit	Single unit	Double unit	Agglomerate of two single units
			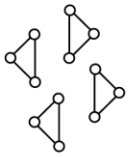

(a)

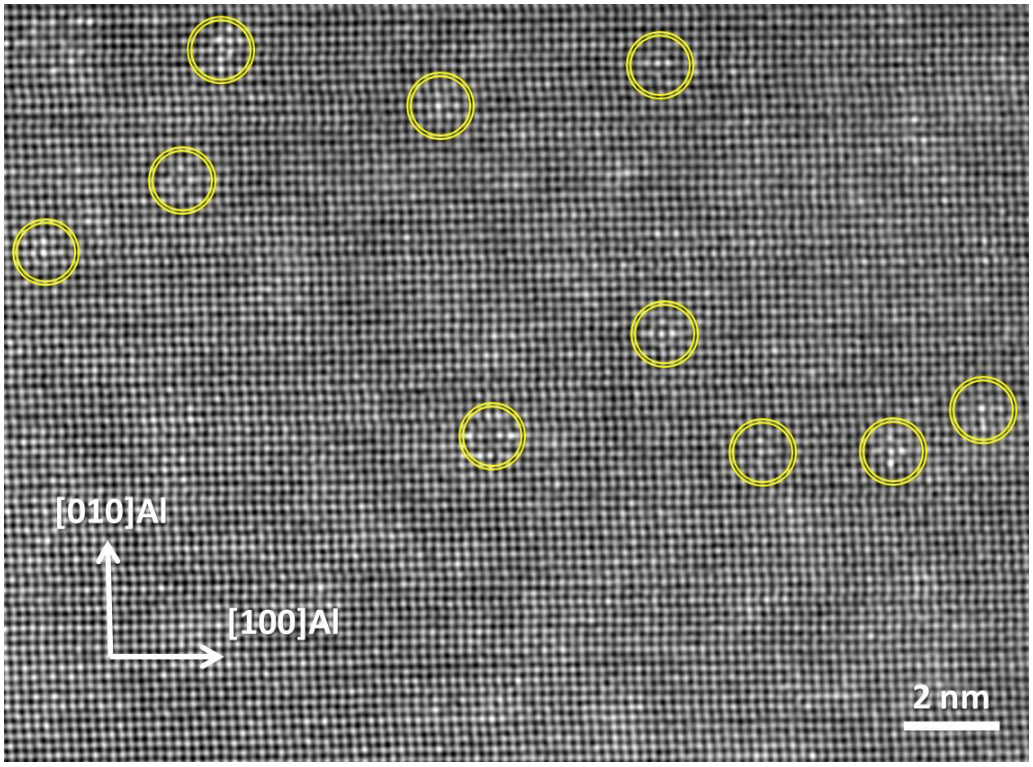

(b)

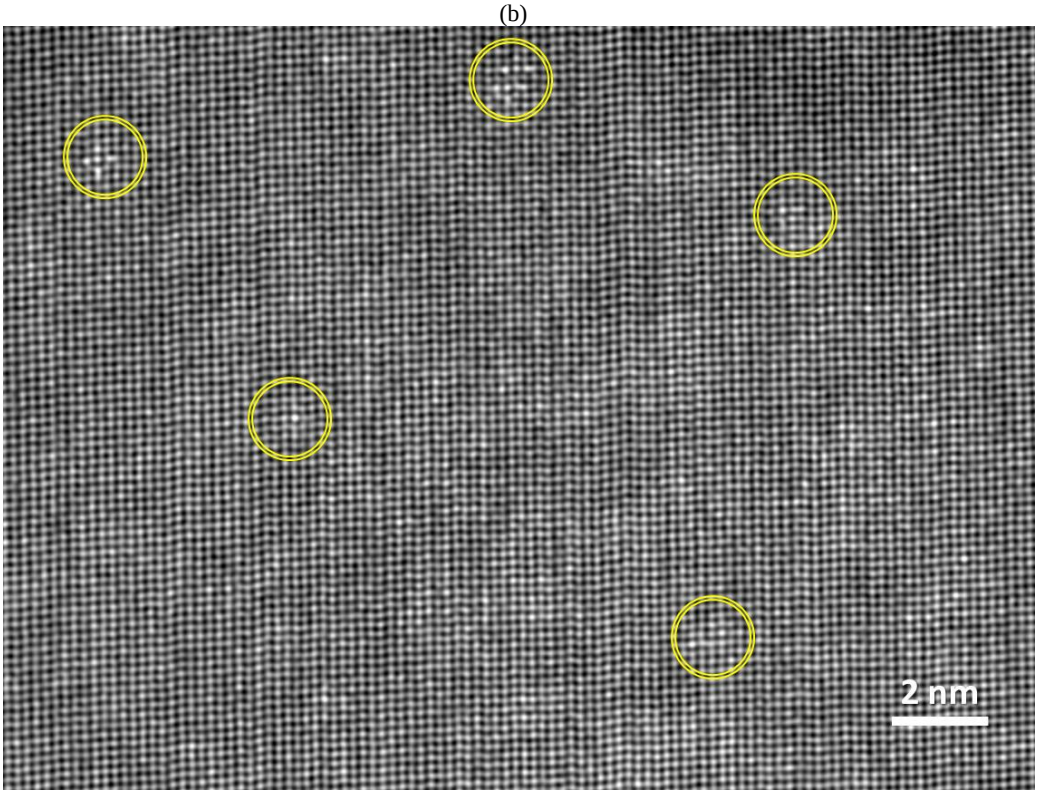

Fig. 3.4 Enlarged HAADF-STEM images for the Base alloy aged at 443 K for 0.06 ks. The microstructure consists of a multitude of structural units of GPB zone (yellow circles).

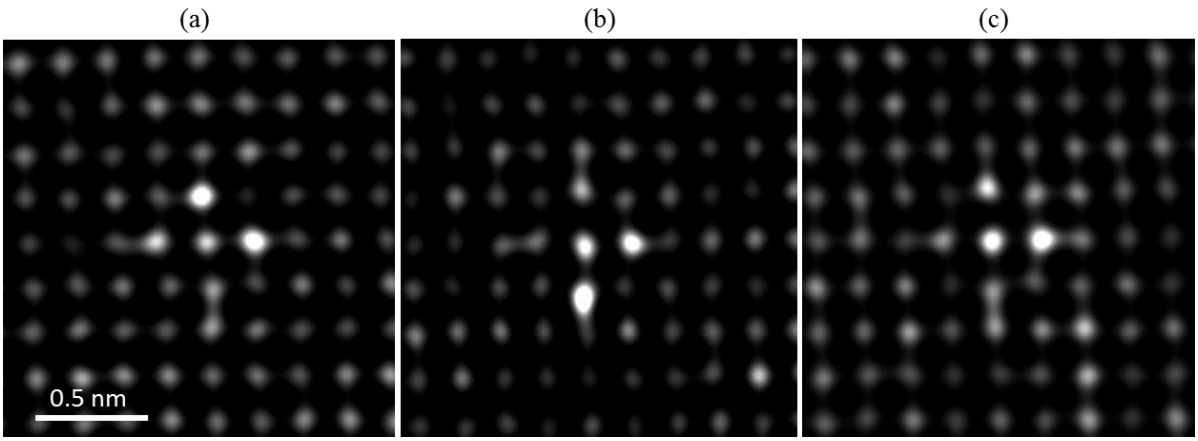

Fig. 3.5 Half unit of GPB zone in the Base alloy aged at 443 K for 0.06 ks.

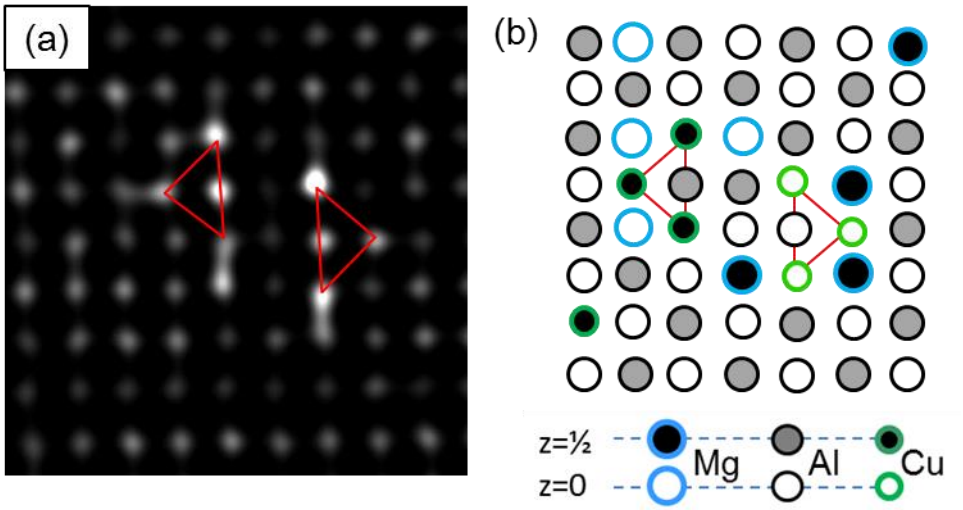

Fig. 3.6 (a) HAADF-STEM image and (b) deduced map of all elemental columns over cross section of a single unit of GPB zone for the Base alloy aged at 443 K for 0.06 ks. Columns correspond to the two Al planes z=0 and ½ (0.203 nm). A red triangle defines a half of the unit of GPB zone. The structure is close to fcc-based structure.

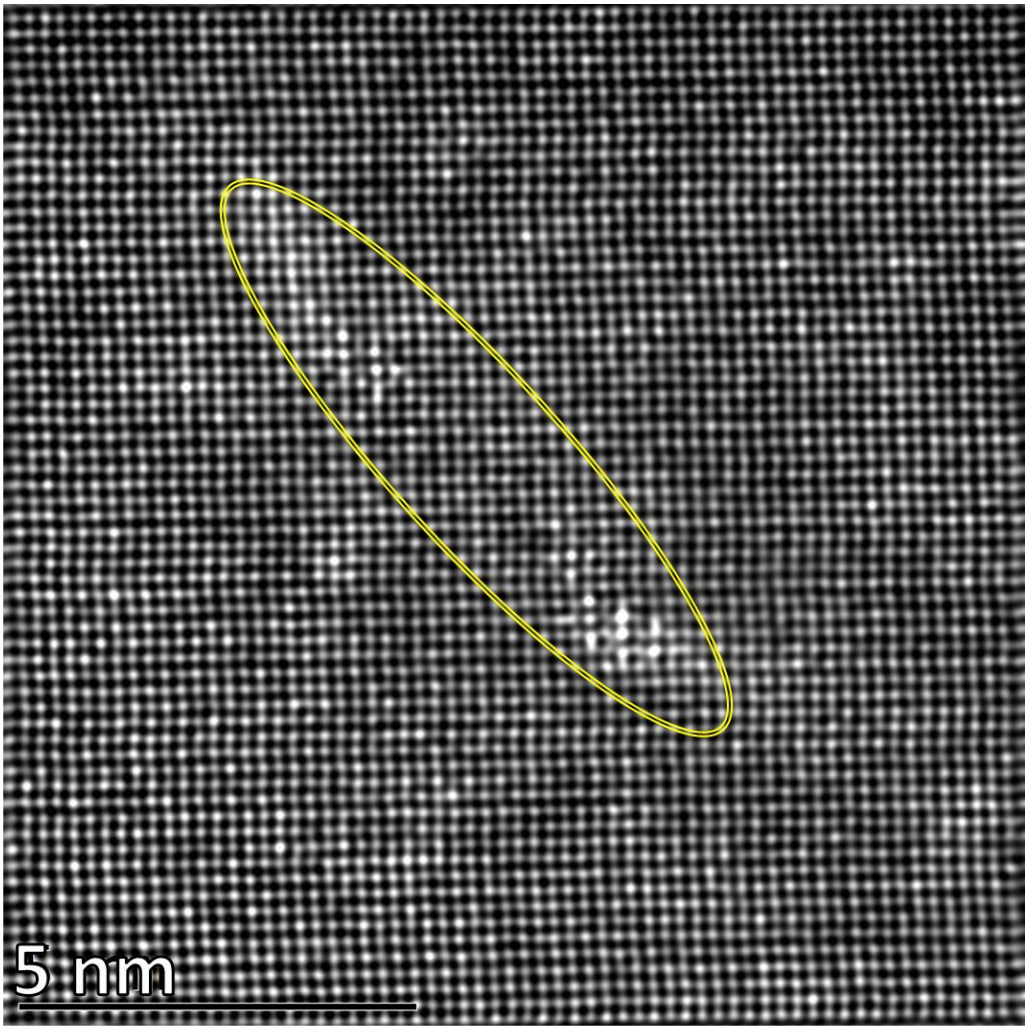

Fig. 3.7 HAADF-STEM image of structural units of GPB zone with a dislocation line running from up left to down right for the Base alloy aged at 443 K for 0.06 ks.

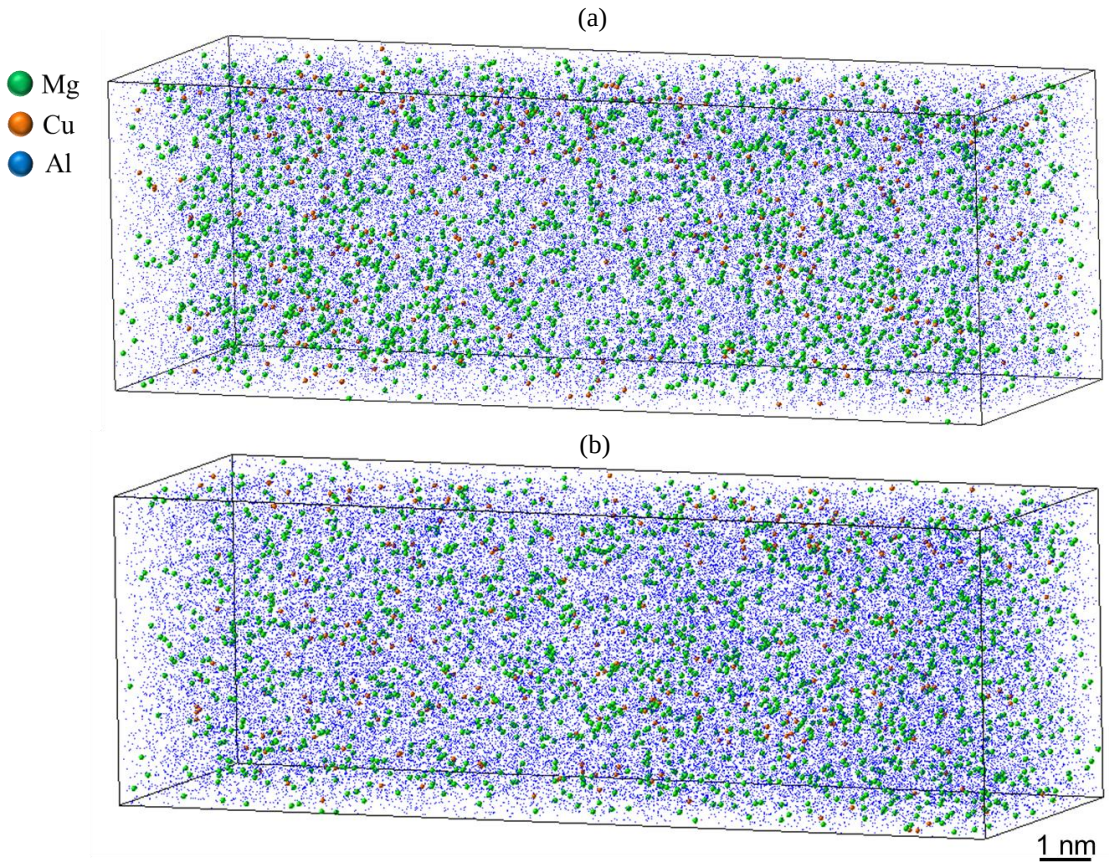

Fig. 3.8 APT reconstructed volumes for the Base alloy aged at 443 K for (a) 0.06 ks and (b) 3.6 ks.

Table 3.4 The total number of atoms detected by 3DAP measurements.

Aging time	number of atoms detected, $\times 10^6$	total number of the blocks
0.06 ks	6.5	22901
3.6 ks	0.5	2059

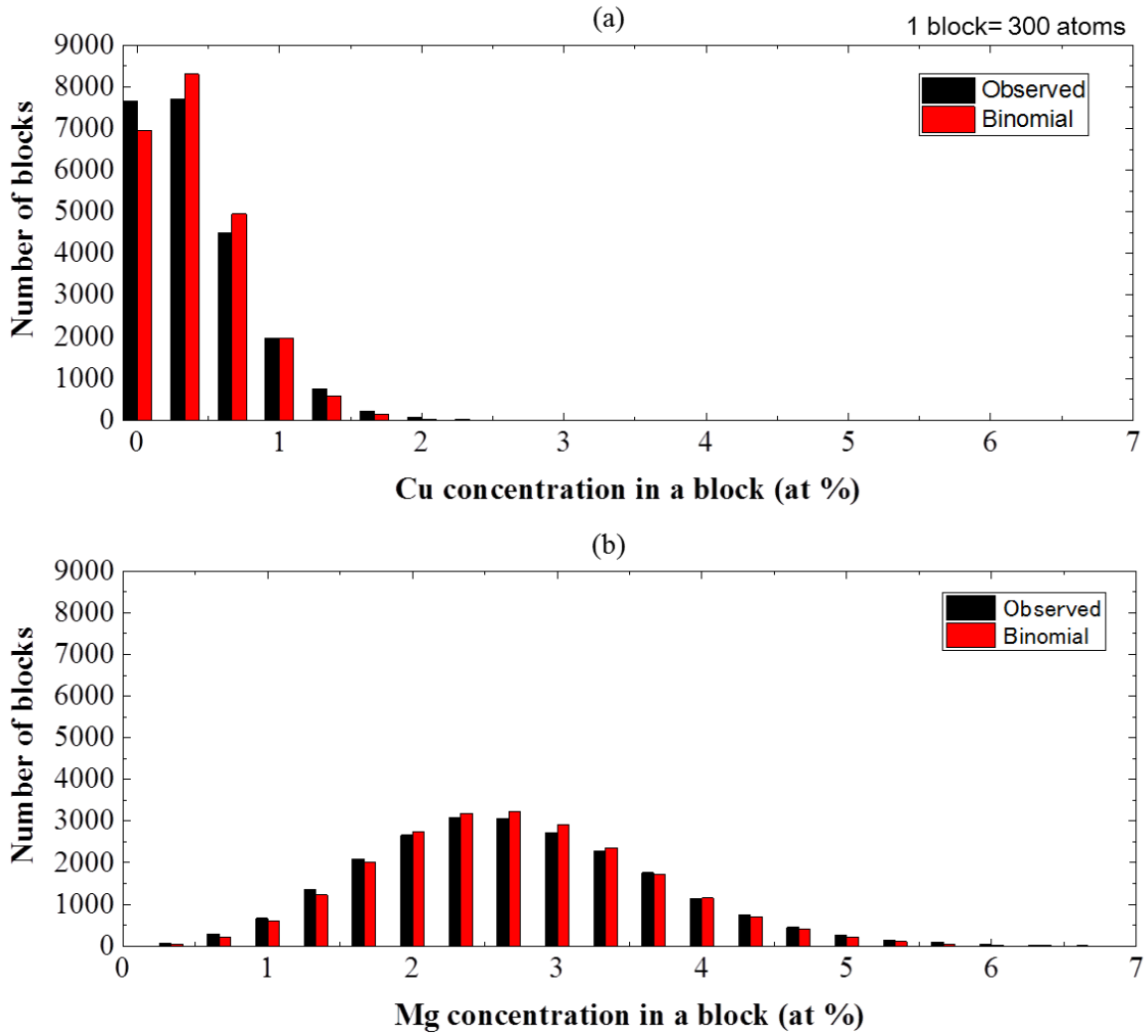

Fig. 3.9 The observed frequency distributions together with binomial (random) distributions for the investigated alloy aged for 0.06 ks

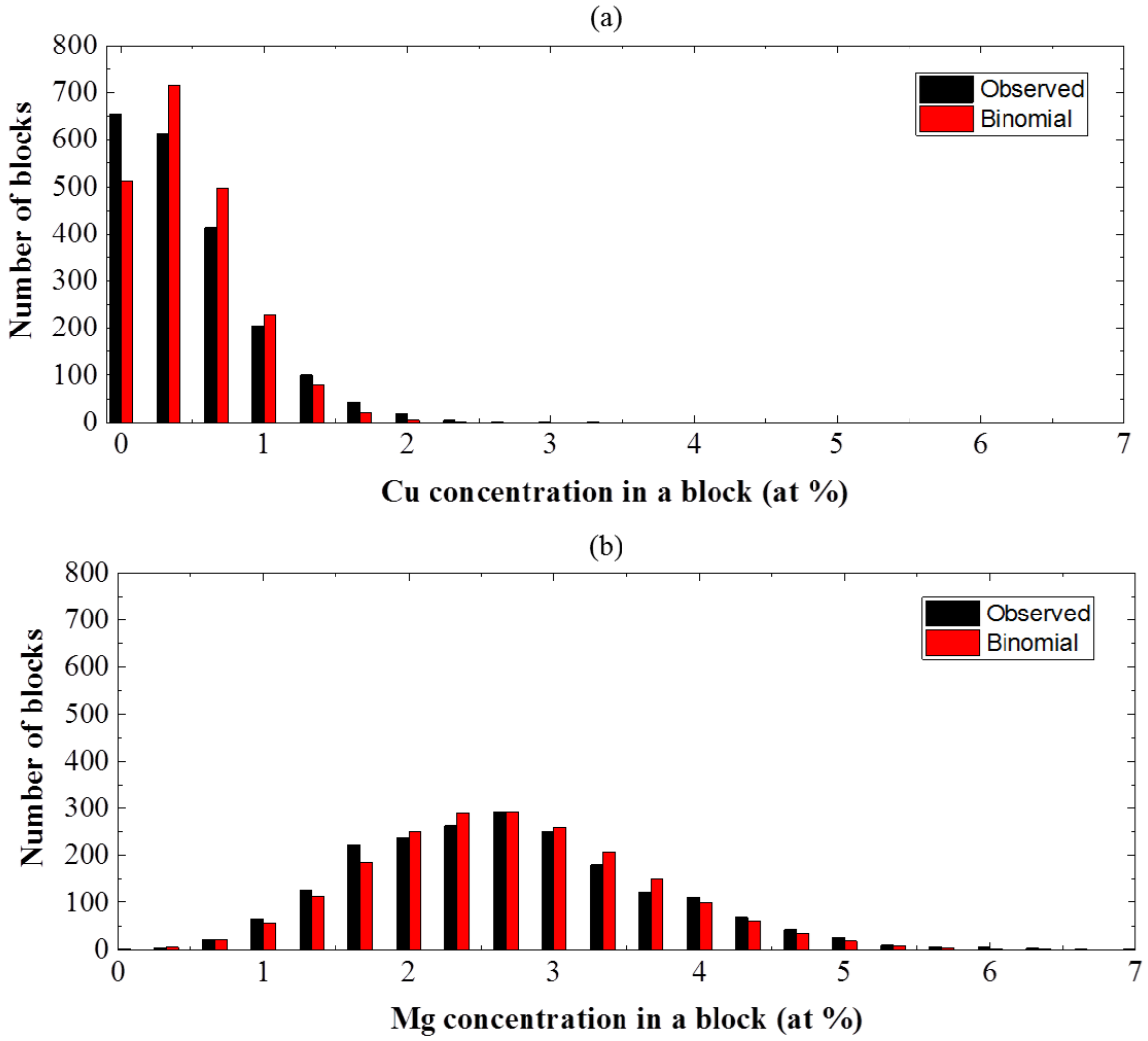

Fig. 3.10 The observed frequency distributions together with binomial (random) distributions for the investigated alloy aged for 3.6 ks

Table 3.5 χ^2 value and degree of freedom for Cu-Mg interactions obtained by contingency table analysis

(a)

	χ^2	degree of freedom
Cu-Cu	397	7
Mg-Mg	168	20
Cu-Mg	79	42

(b)

	χ^2	degree of freedom
Cu-Cu	174	16
Mg-Mg	44	6
Cu-Mg	41	35

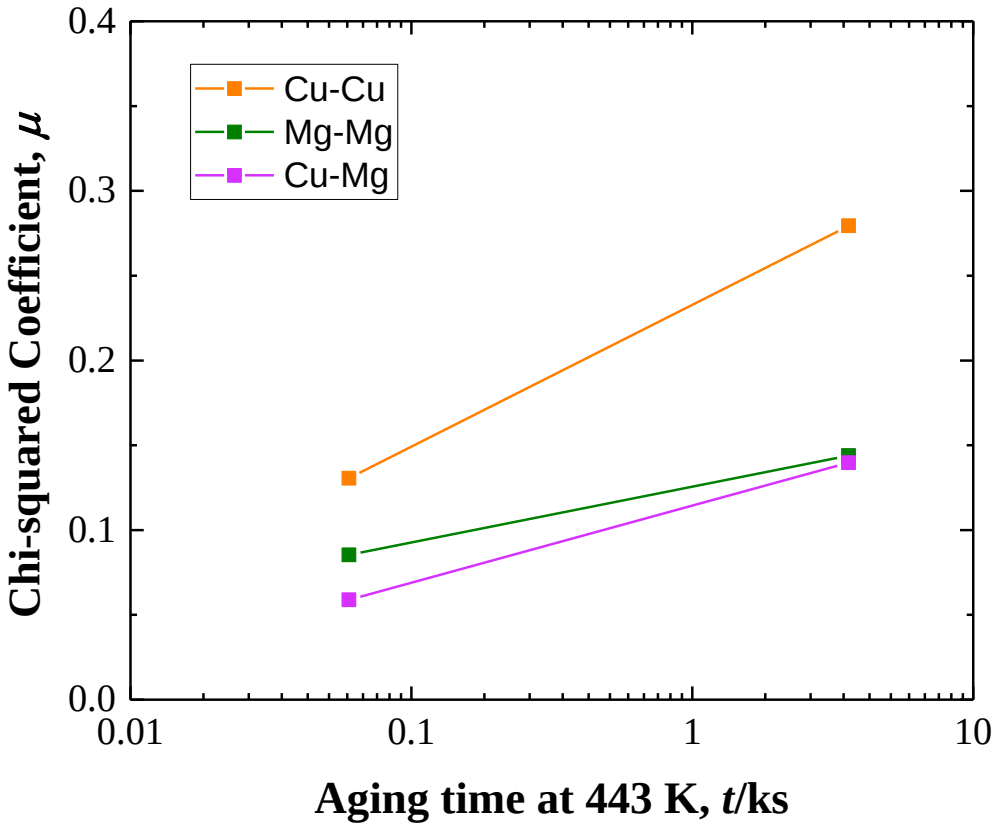

Fig. 3.11 Chi-squared coefficient calculated from APT data for Cu-Mg, Mg-Mg and Cu-Cu clustering for the Base alloy aged at 443 K.

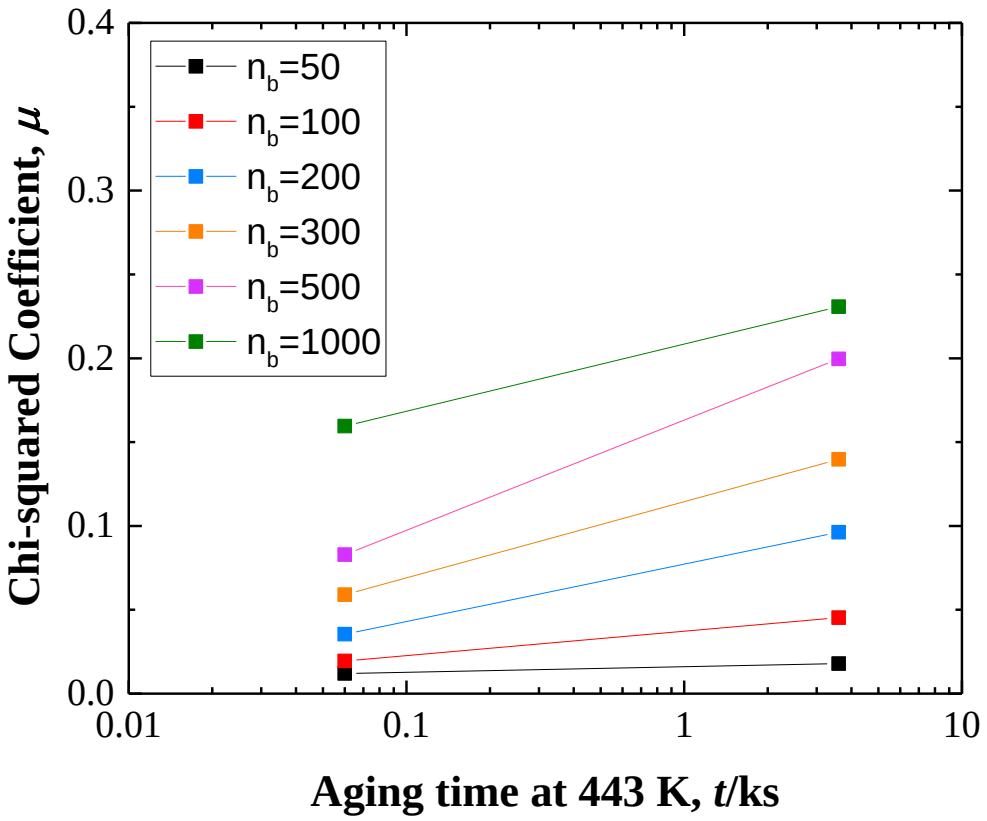

Fig. 3.12 Effect of the block size on the Chi-squared coefficient calculated from APT data for Cu-Mg, clustering for the Base alloy aged at 443 K.

(a)

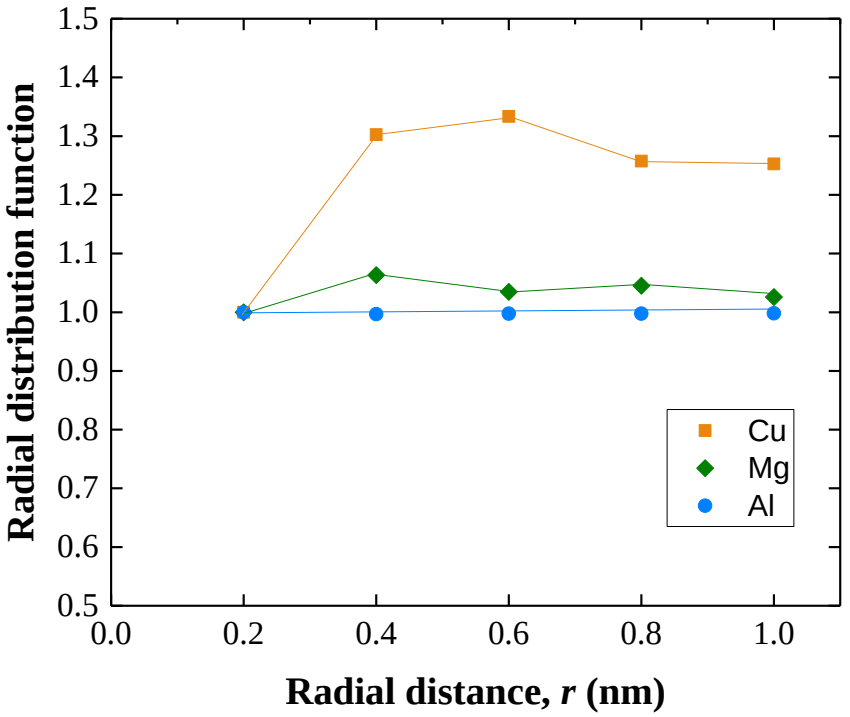

(b)

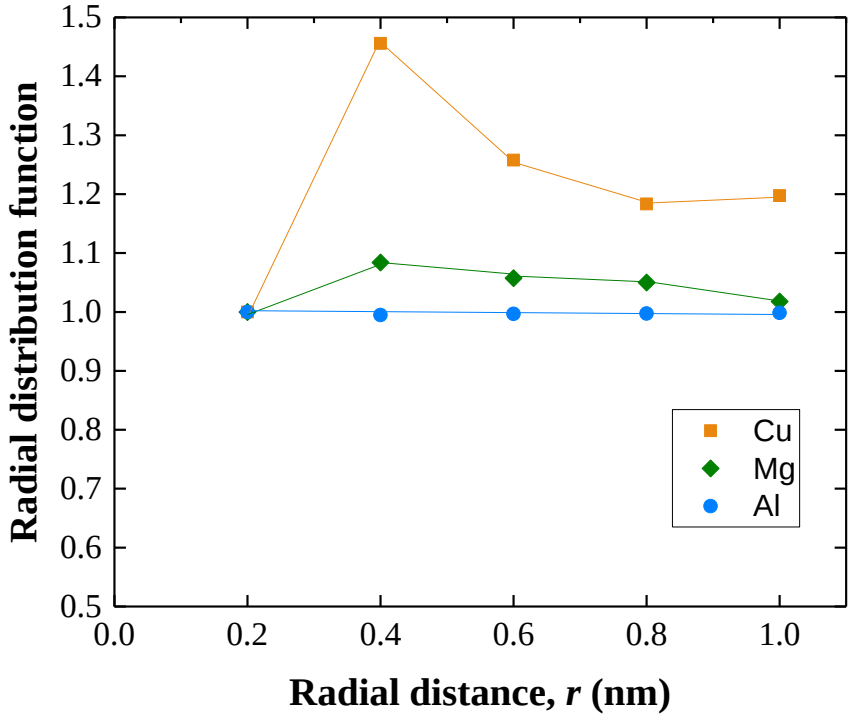

Fig. 3.13 Standardized radial distribution functions versus radial distance around Cu atoms in the Base alloy aged for (a) 0.06 ks and (b) 3.6 ks.

(a)

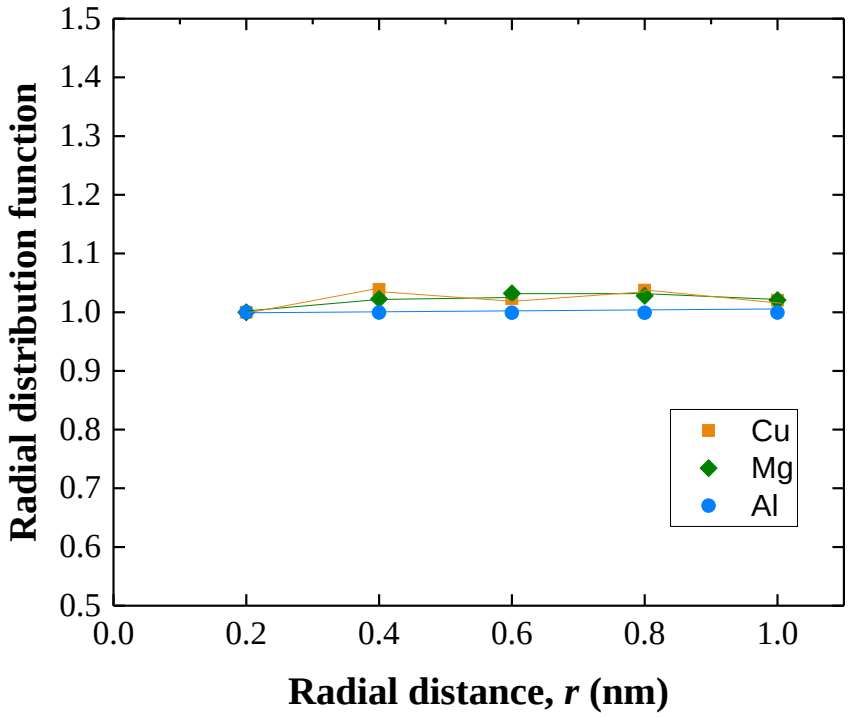

(b)

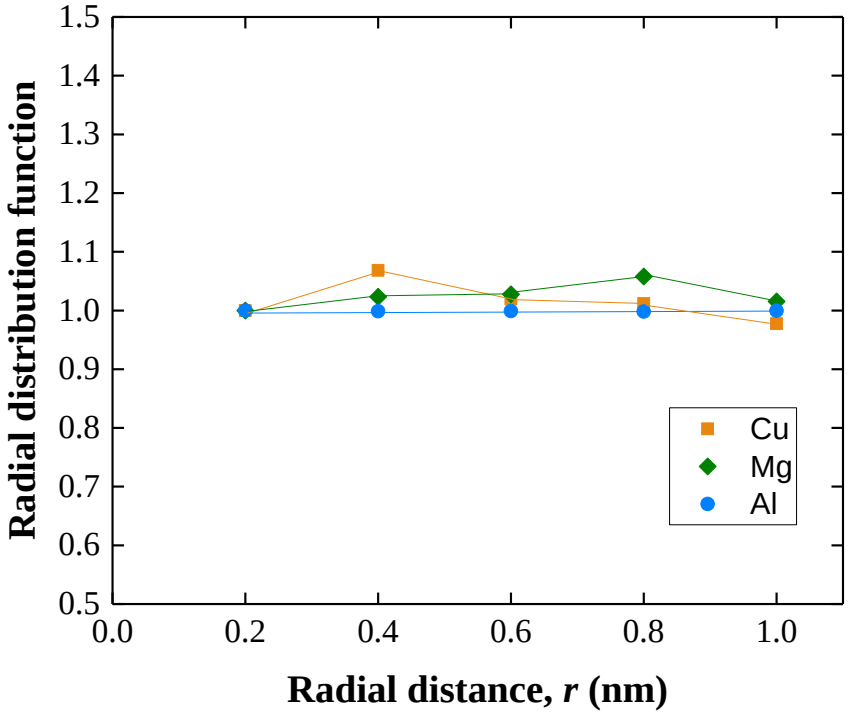

Fig. 3.14 Standardized radial distribution functions versus radial distance around Mg atoms in the Base alloy aged for (a) 0.06 ks and (b) 3.6 ks.

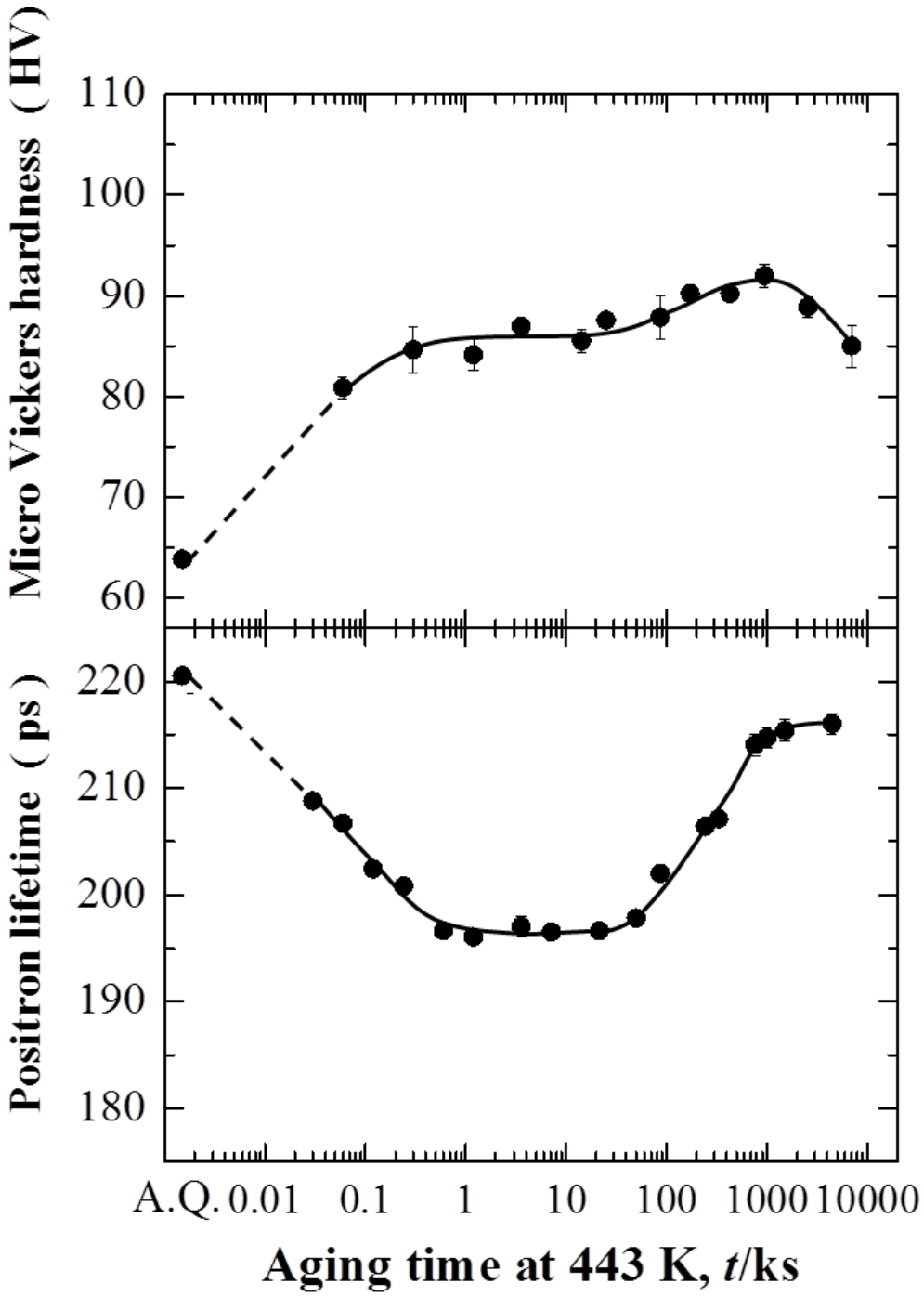

Fig. 3.15 Evolution of the hardness and positron lifetime during aging at 443 K.

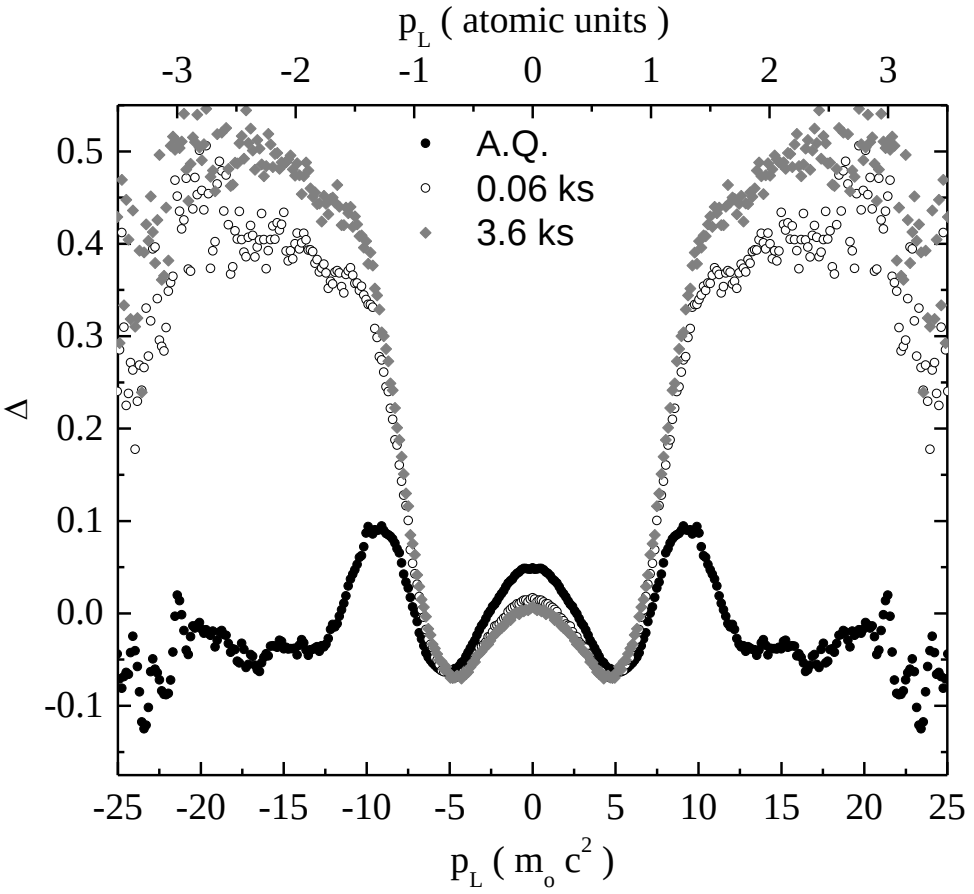

Fig. 3.16 CDB differences curves relative to well-annealed pure Al for the Base alloy aged at 443 K.

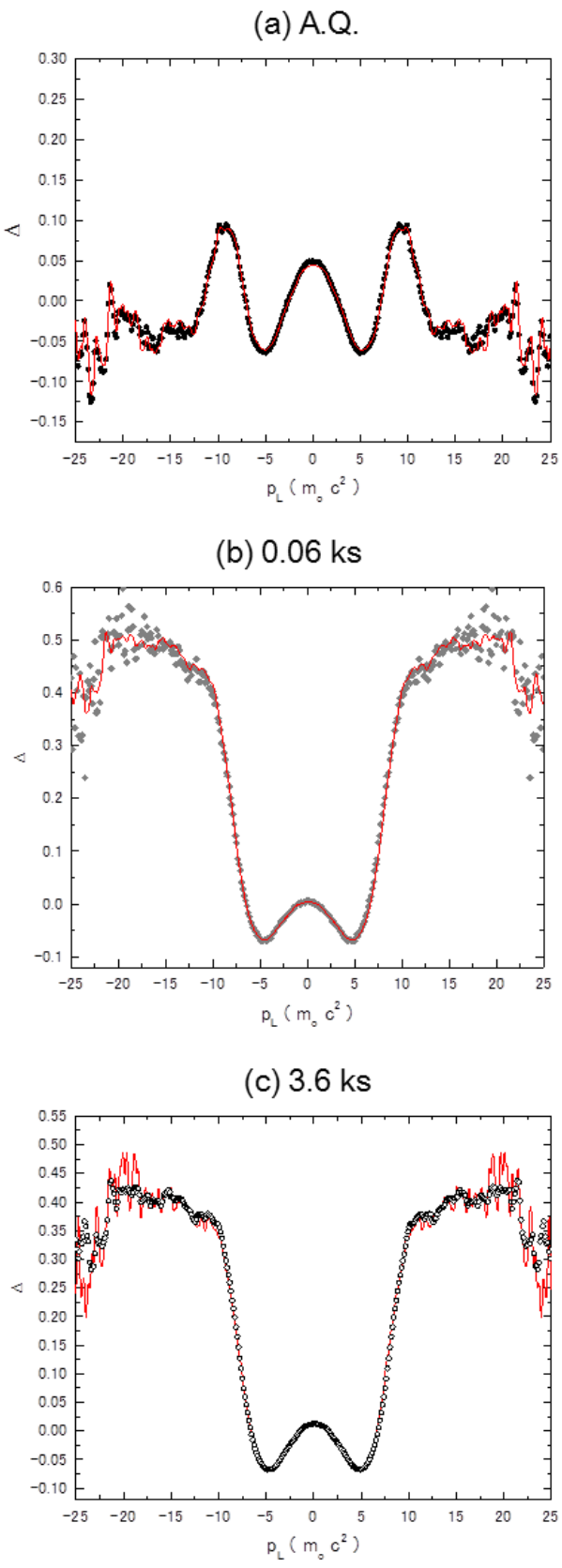

Fig. 3.17 Results of the fitting procedure for the curves in Fig. 3.15 using reference spectra.

Table 3.6 Fractional concentrations of the alloy components in contact with vacancies in the Base alloy for different aging conditions. These values were obtained by fitting the CDB curves using Eq.(3.9). F_{trap} is the trapping fraction of the positrons trapped and annihilated in vacancies under the aging conditions.

aging condition	F_{trap} (%)	C_{Al} (%)	C_{Mg} (%)	C_{Cu} (%)
A.Q.	54	64	11	25
0.06 ks	59	37	17	46
3.6 ks	60	32	15	53

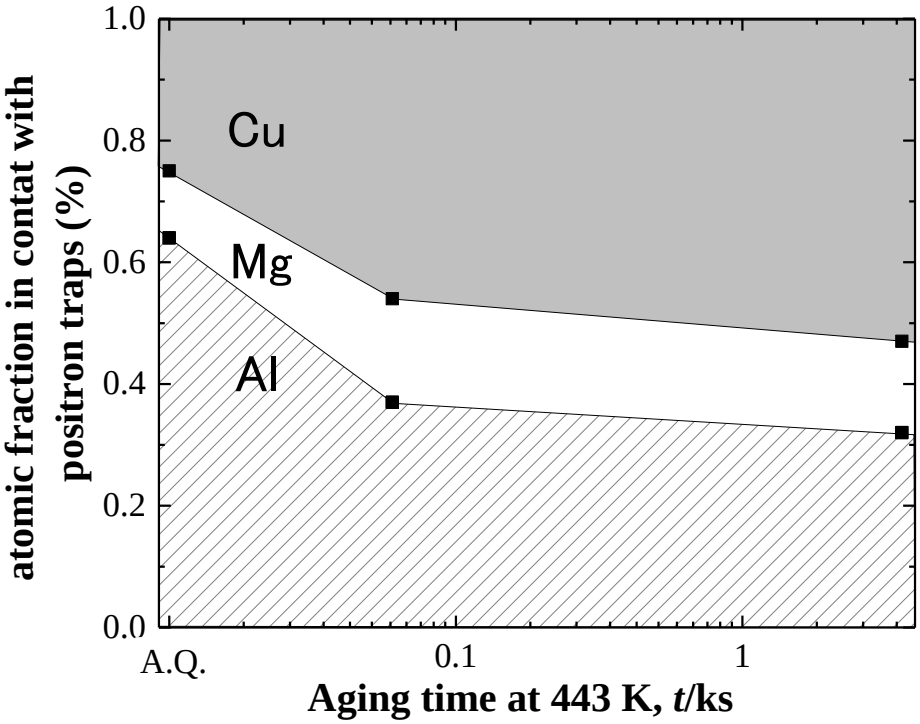

Fig. 3.18 Elemental fractions in contact with vacancies as a function of the aging time at 443 K for the Base alloy.

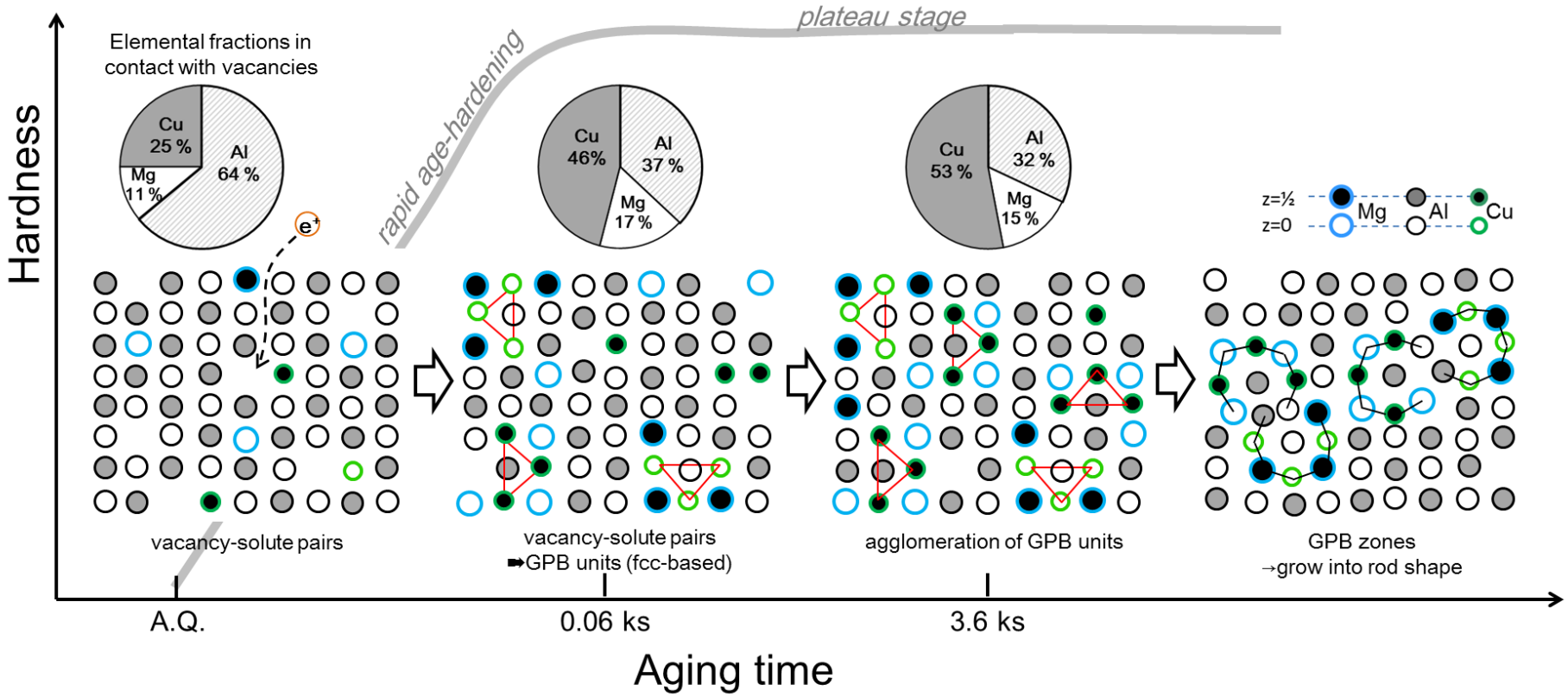

Figure 3.19 Schematic illustration for the formation behavior of structural units of GPB zone and zones during

.

Chapter 4

Effect of Different Cu, Mg compositions on Age-hardening Behavior in an Al-Mg-Cu alloy

4.1 Introduction

In the previous chapter, HAADF-STEM investigation revealed that structural units of GPB zone were formed after aging at 443 K for 0.06 ks in the Al-3Mg-1Cu alloy. Based on the 3DAP data analysis, it is apparent that there is strong Cu-Cu correlation. Furthermore, PAS investigation clarified that the concentration of Cu atoms in contact with vacancies increased rapidly in the initial decomposition. In order to deeply understand the role of Cu and Mg atoms during the initial decomposition, alloys with different Mg,Cu compositions will be used in this chapter. The vacancy behavior during the initial decomposition will be investigated by the evolution of positron lifetime during aging. In addition, tensile test will be applied in order to investigate the serrated yielding behavior during aging. The serrated yielding is characterized by the zigzag shape of the stress-strain curve. The serrated yielding is due to dynamic strain aging (DSA) during deformation which is called Portevin - LeChatelier (PL) effect, where mobile dislocations are repetitively locked and unlocked by solute atmospheres [1, 2]. Precipitates which are formed during aging before deformation might be responsible for the DSA by interacting the dislocations during deformation. Much works have been done to clarify the effects of aging conditions [3-6] on the serrated yielding. For instance, in Al-Mg-Si alloys, the serrated yielding is clearly observed in the solution treated specimens and disappeared gradually with aging proceeds [6]. Furthermore, the serrated yielding is eliminated by aging at above 353 K due to the formation of solute clustering in a 6061 alloy [6]. However, there has been limited number of published work regarding the serrated yielding occurring in Al-Mg-Cu alloys.

In this chapter, the effect of different alloy compositions on the age-hardening behavior and serrated yielding behavior in the stress-strain curves of an Al-Mg-Cu alloy are investigated.

4.2 Experimental Procedure

4.2.1 Alloy Compositions

The chemical composition of the alloys utilized in this chapter is listed in **Table 4.1**. The Base alloy which was used in the previous chapter is renamed as 3M1C alloy (3% Mg and 1% Cu). The letters of M and C are abbreviation pf Mg and Cu. In addition to the 3M1C alloy, 3M1.5C, 4M1C and 4M1.5C alloys with different Cu, Mg compositions are prepared. All of the investigated alloys lie in (α+S+T) [7] **(Fig. 4.1)**.

4.2.2 Heat Treatment

Samples were solution treated in a salt bath at 793 K and kept for 3.6 ks, followed by quenching in ice-water and held for 60 s. The aging treatment was carried out in an oil bath at 443 K and 323 K.

4.2.3 Hardness, Electrical Resistivity and DSC

Hardness, electrical resistivity and DSC measurements were conducted in the same procedure as described in the Chapter 2.

4.2.4 PAS

PALS measurements were conducted in the same procedure as described in the Chapter 3.

4.2.5 Tensile test

Tensile test was conducted at room temperature with a cross head speed of 0.017 mm/s for the specimen aged at 443 K for various times by using a Shimazu autograph AG-X plus tensile machine. Specimens for the tensile tests were taken in the longitudinal orientation (i.e. parallel to the rolling direction) with 30.0 mm gauge length. The fracture surface was observed by Field Emission Scanning Electron Microscope (JEOL JSM-7000F) at room temperature.

4.3 Results

4.3.1 Effect of Different Cu, Mg Compositions on the Age-hardening Response

I. Hardness and Electrical Resistivity Changes During Aging at 443 K

Hardness changes for the 3M1C (Base), 3M1.5C and 4M1C during aging at 443 K are shown in the upper part of **Fig. 4.2**. In 3M1.5C and 4M1C, the hardness at A.Q. state is increased by solid-solution strengthening. Age-hardening response is improved by increasing amount of Cu or Mg (3M1.5C and 4M1C), not only at the hardness peak but overall aging curve. Especially, the increasing amount of Cu apparently enlarges the increase of the hardness in the initial stage of aging. However, by increasing amount of Mg, the time to reach the hardness peak becomes longer. Electrical resistivity changes during aging at 443 K well corresponds to that of the hardness (lower part of the **Fig. 4.2**). The rapid increase in the resistivity is caused by the formation of the nanostructures (solute clusters or structural units of GPB zone). It is suggested that the volume fraction of nanostructures which form during initial stage of aging increased by increasing amount of Cu. The rapid fall of the electrical resistibility is due to the formation and growth of the precipitates such as GPB zones, S' or Z phases, according to the results obtained in the previous chapter. In 4M1C, the fall of the electrical resistivity is delayed by Mg addition. In consistent with the results of the hardness measurements, it is suggested that increasing amount of Mg retards the precipitation reaction after long term aging.

II. DSC Analysis

In all alloys, four exothermal peaks (peak A, B, C and D) are observed in the DSC curves for the specimens at A.Q. state [**Fig. 4.3(a)**]. After aging for 0.01 ks at 443 K, the peak A is fully disappeared in all alloys [**Fig. 4.3(b)**]. According to the previous chapter, each of four peak is

attributed to the formation of structural units of GPB zone, GPB zone, S' phase and Z phase, respectively. **Figures 4.4** summarizes the peak area and temperature for the peak A observed in the DSC curves in **Fig. 4.3 (a)**. Peak area can be understood as the volume fraction of the structural units of GPB zone formed during DSC scan. In 3M1.5C, the peak area is strongly increased by Cu addition. Thus increasing amount of Cu is effective to promote the formation of GPB zones in the Al-3Mg-1Cu alloys, whereas increasing amount of Mg seems to be less effective. In addition, the peak temperature is increased by increasing amount of Mg.

4.3.2 PALS

Figure 4.5 shows the evolution of the positron lifetime and hardness for the investigated alloys during aging at 443 K. In all alloys, the positron lifetime decreases rapidly in the initial, then it remains almost constant for a long time. Initial strong decrease of the positron lifetime is a common feature in Al-Cu based alloys, as described in previous chapter. This behavior is attributed to a concomitant effect of a decrease of the fraction of positrons trapped in vacancies and an increasing concentration of Cu atoms in contact with vacancies [8, 9]. After the plateau stage, the positron lifetime increased again corresponding to the increase in hardness. The evolution of positron lifetime appears to be sensitive to the change of alloy compositions. In 4M1C, the reduction of the lifetime in the initial is less marked and the overall lifetime value is consistently higher than that of other two alloys, whereas the reduction is enhanced in 3M1.5C,. The duration of the plateau stage is shortened in the 3M1.5C.

4.3.3 Tensile Tests

Fig. 4.6 shows the stress-strain curves for 3M1C aged at 443 K for various times. All flow curves show serrated flow. The critical (onset) strains for serrated yielding (ε_c) increase with increasing aging time. **Fig. 4.7** shows the stress-strain curves for the investigated alloys aged

at 443 K for 1.2 ks which corresponds to the middle of the plateau stage. Increasing amount of Cu or Mg causes the increase of the flow stress and ductility. All of the investigated alloys show dimple fracture surface (**Fig. 4.8**). **Fig.4.9** shows the variation for the (a) 0.2 % proof stress and (b) critical strain for 3M1C, 3M1.5C and 4M1C after aging at 443 K for various times. In all alloys, 0.2% proof stress increases rapidly after aging for 0.06 ks, and then they show almost constant value during aging. However, the critical strain increases very slightly as aging proceeds in all alloys. The increment of the 0.2% proof stress in 3M1.5C is the largest of all.

Fig.4.10 shows the variation of the stress amplitude for the 3M1C, 3M1.5C and 4M1C alloys aged at 443 K for 1.2 ks. In all alloys, the stress amplitude increases slightly with increasing the strain, however there are no significant difference among the three alloys. These results indicate that microstructural changes by different alloy compositions do not have significant effect on the serrated yielding behavior of the specimens.

4.4 Discussion

4.4.1 Role of Cu and Mg atoms in the Initial Decomposition

In all investigated alloys, the positron lifetime values in the initial stage are higher than that of vacancy-Cu pairs (180 ps), suggesting the presence of Mg atoms associated with vacancy-Cu complexes formed during the initial stage of aging. According to the evolution of positron lifetime during aging (**Fig. 4.5**), it is clearly indicated that Mg atoms promote the quenched-in vacancies to be retained during aging. However, based on the DSC results, increasing amount of Mg was found to be less effective to promote the formation of the structural units of GPB zone comparing to Cu. One possible explanation is that vacancy is trapped by Mg atoms and delay the formation kinetics of the structural units of GPB zone. Thus, peak

temperature for the exothermic peak A in the DSC curve (Fig. 4.3 (a)) for 4M1C is shifted to the higher temperature. CDB investigation is needed here. In 3M1.5C, amount of Cu in contact with vacancy might be increased and it promotes the formation of the structural units. Therefore, the area of exothermic peak A in 3M1.5C becomes large.

4.4.2 Evolution of Serrated Yielding in the Stress-strain Curves

Mg solute atoms are commonly believed to cause the serrated yielding [10] and a lot of work have been done regarding serrated yielding in Al-Mg alloys. However, the serrated yielding is generally not observed in Al-Cu-Mg alloys which lie in (α+S) phase field [11]. In the present study, serrated yielding appears in the specimen at A.Q. state and it remains after aging for 0.06 ks, in spite of the microstructural change, i.e. formation of Structural units of GPB zone. In Al-Cu-Mg alloys, solute clusters, structural units of GPB zone and GPB zones are considered to be formed as well as in Al-Mg-Cu alloys during aging. The difference between two alloy systems is Mg content. According to the microstructural investigation in the previous chapter, structural units of GPB zone which consists of Cu and Mg atoms form after aging for 0.06 ks in the Base (Al-3Mg-1Cu) alloy. However there must be substantial amount of Mg solutes which is not incorporated to the structural units of GPB zone. In the present study, it seems that formation of the structural units of GPB zone do not significantly affect the serrated yielding and Mg solutes might cause the serrated yielding. The serrated yielding remains after aging for 864 ks, where precipitates such as GPB zones, S' phase and Z phase are formed. It indicates that large amount of solute Mg atoms which causes the serrated yielding are exist even after long term aging. It is the characteristic feature of Al-Mg-Cu alloys.

4.5 Conclusions

1. Age-hardening response is improved by increasing amount of Cu or Mg in the alloy composition. Cu addition has strong effect on the rapid age-hardening response.
2. It is clearly indicated that Mg atoms promote the quenched-in vacancies to be retained during aging. However, increasing amount of Mg in alloy composition is less effective to promote the formation of the structural units of GPB zone. Increasing amount of Cu results in the large amount of Cu in contact with vacancies and the formation of the structural units of GPB zone is promoted.
3. Serrated yielding is observed in stress-strain curves for the investigated alloys. The critical strains for serrated yielding slightly increase with increasing aging time however it remains during aging. Different alloy compositions do not have significant effect on the serrated yielding behavior. It is indicated that Mg solutes causes the serrated yielding and large amount of solutes which causes the serrated yielding are exist even after long term aging. It is the characteristic feature of Al-Mg-Cu alloys.

References

1) P.G. Mccormick and C.P. Ling, Acta Metall. Mater., 43 (1995) 1969.

2) W.A. Curtin, D.L. Olmsted and L.G. Hector Jr., Nature Materials, 5 (2006) 875.

3) K. Matsuura, T. Nishiyama and S. Koda, Trans. Jpn. Inst. Met., 10 (1969) 429.

4) Y. Nakayama, J. Japan Inst. Metals, 65 (2001) 1.

5) E. Pink and J. Król, Acta Metall. Mater., 43 (1995) 2351.

6) Y. Nakayama and K. Naruke, Journal of Japan Institute of Light Metals, 51 (2001) 346-350.

7) G. B. Brook: Precipitation in Metals, Spec. Rep. No. 3, Fulmer Res. Inst., UK (1963).

8) A. Somoza, R. Ferragut, A. Dupasquier, P. Folegati, and I. J. Polmear, Phys. Rev. B 61 (2000) 14 454.

9) Y. Nagai, M. Murayama, Z. Tang, T. Nonaka, K. Hono, and M. Hasegawa, Acta Mater. 49 (2001)913.

10) Wen, Wei. PhD thesis (2004)University of Kentucky, ProQuest Dissertations Publishing.

11) M.J. Starink, N. Gao and J.L. Yan, Materials Science and Engineering A 387 (2004) 222-226.

Table 4.1 Chemical compositions for the investigated alloys.

(wt %)

Sample	Mg	Cu	Si	Fe	Ti	Al
3M1C (Base)	3.04	1.01	0.01	0.01	0.00	Bal.
3M1.5C	2.99	1.50	0.01	0.01	0.00	Bal.
4M1C	3.95	0.99	0.00	0.01	0.00	Bal.

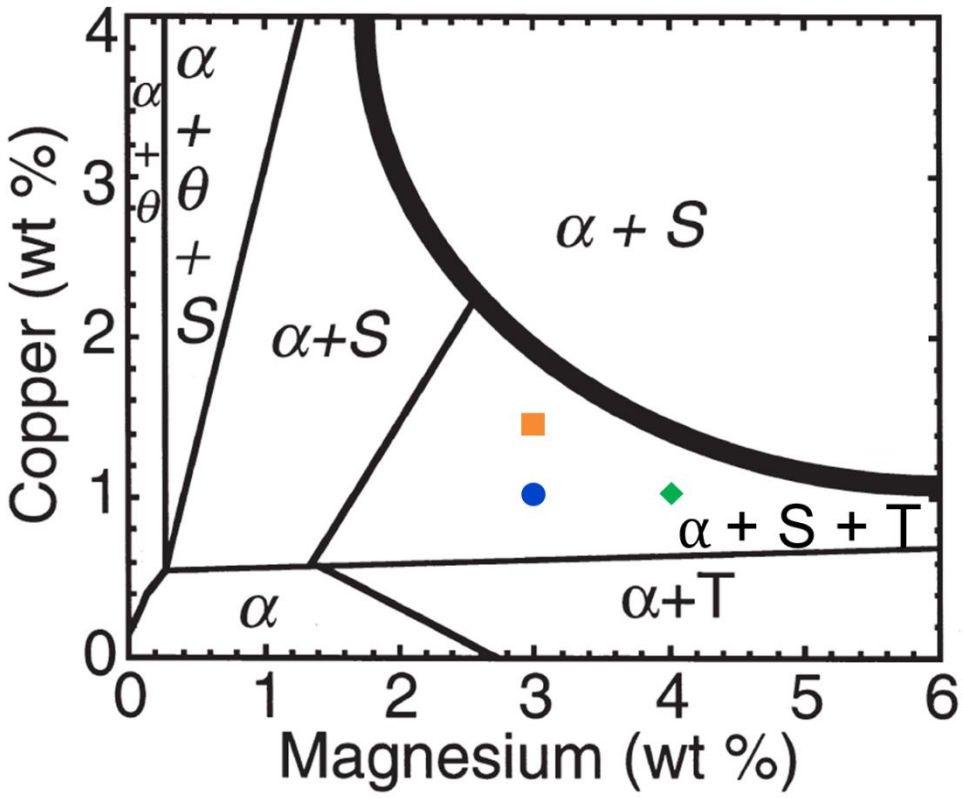

Fig. 4.1 Al-Cu-Mg phase diagram showing phase boundaries at 463K with the investigated alloys marked.[1]

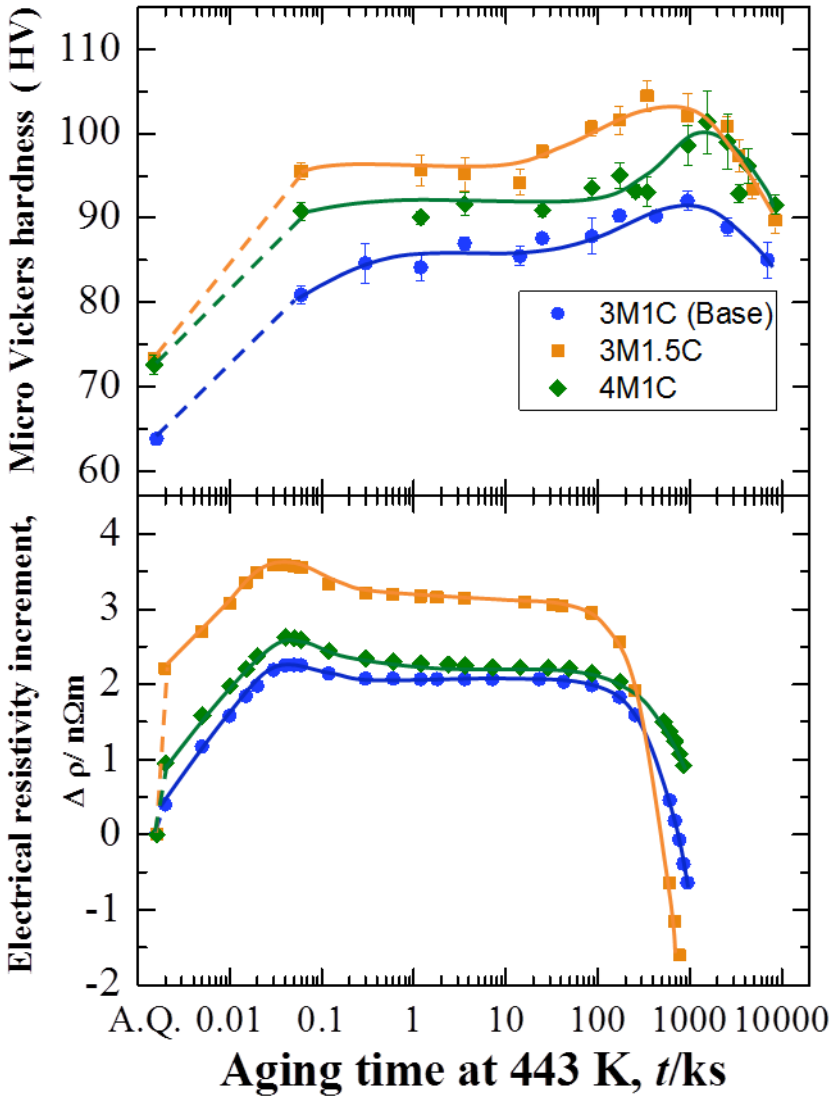

Fig. 4.2 Hardness and electrical resistivity changes during aging at 443 K for the investigated alloys.

(a)

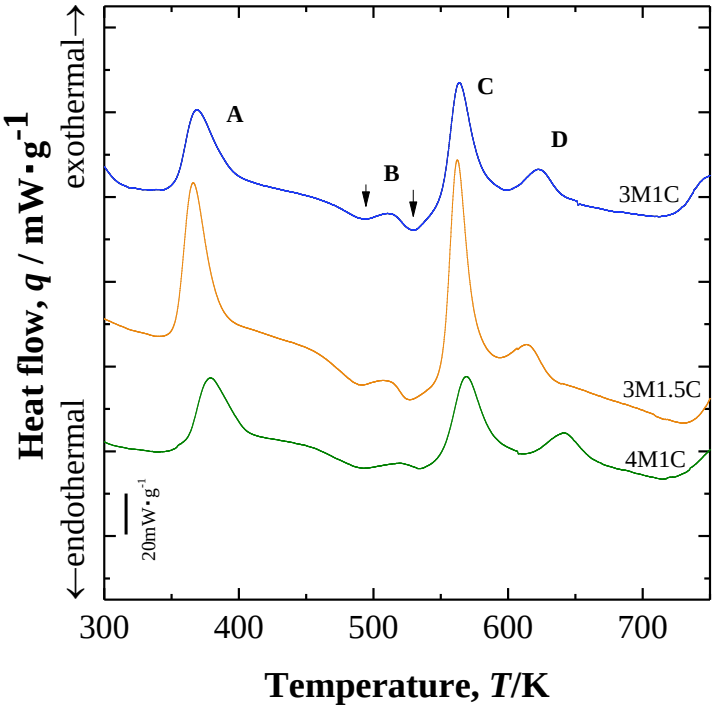

(b)

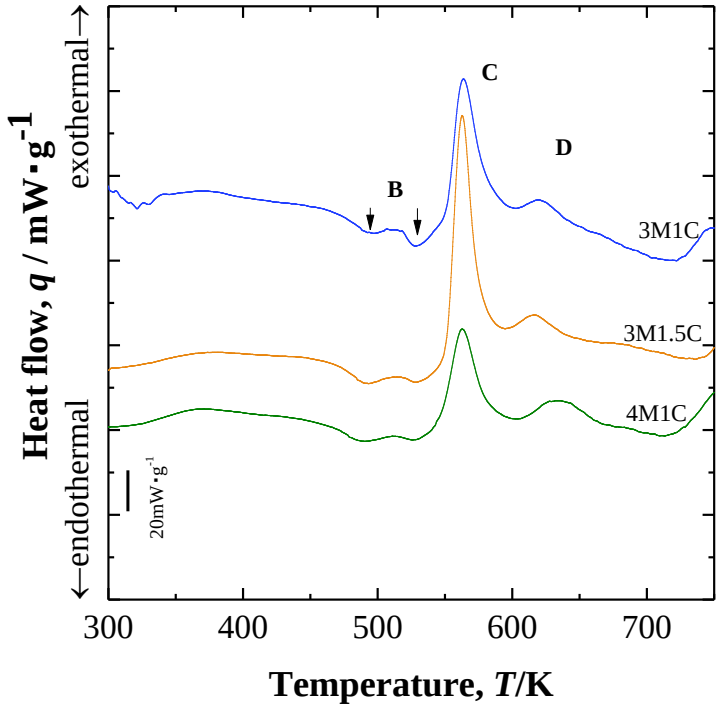

Fig. 4.3 DSC curves for the investigated alloys (a) at A.Q. state and (b) aged at 443 K for 0.06 ks. Heating rate is 10 K/ min.

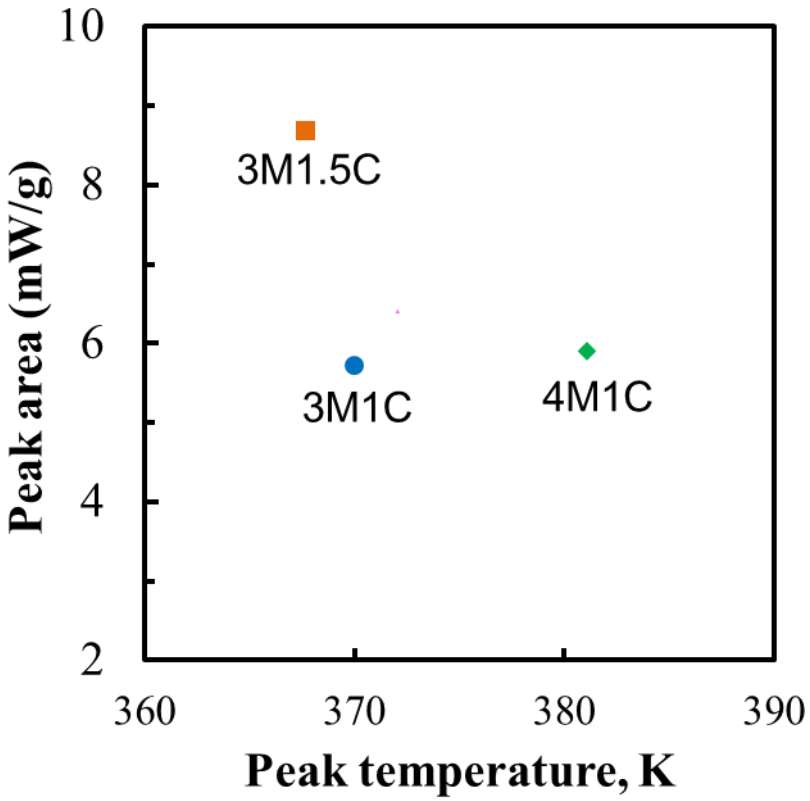

Fig. 4.4 Peak area for the peak A obtained by DSC curves as a function of peak temperature for the investigated alloys.

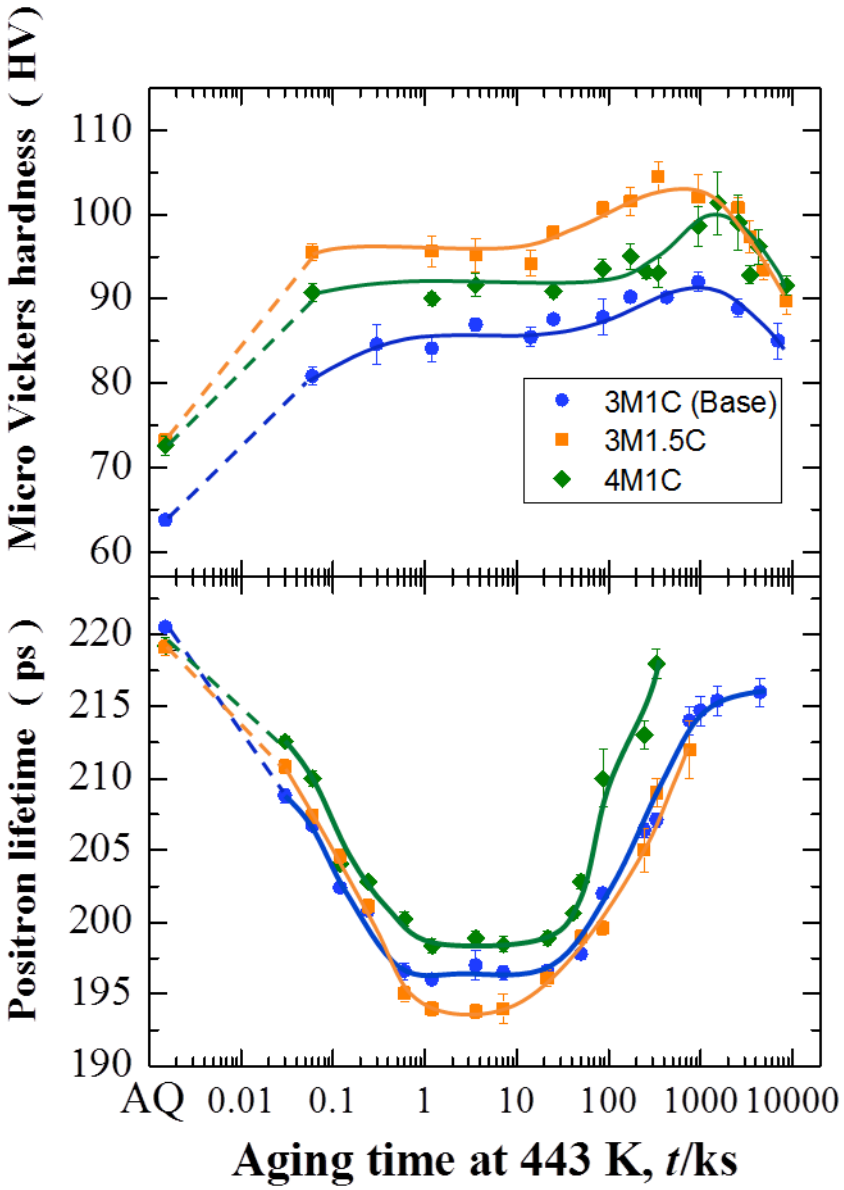

Fig. 4.5 Hardness and positron lifetime evolution during aging at 443 K for the investigated alloys.

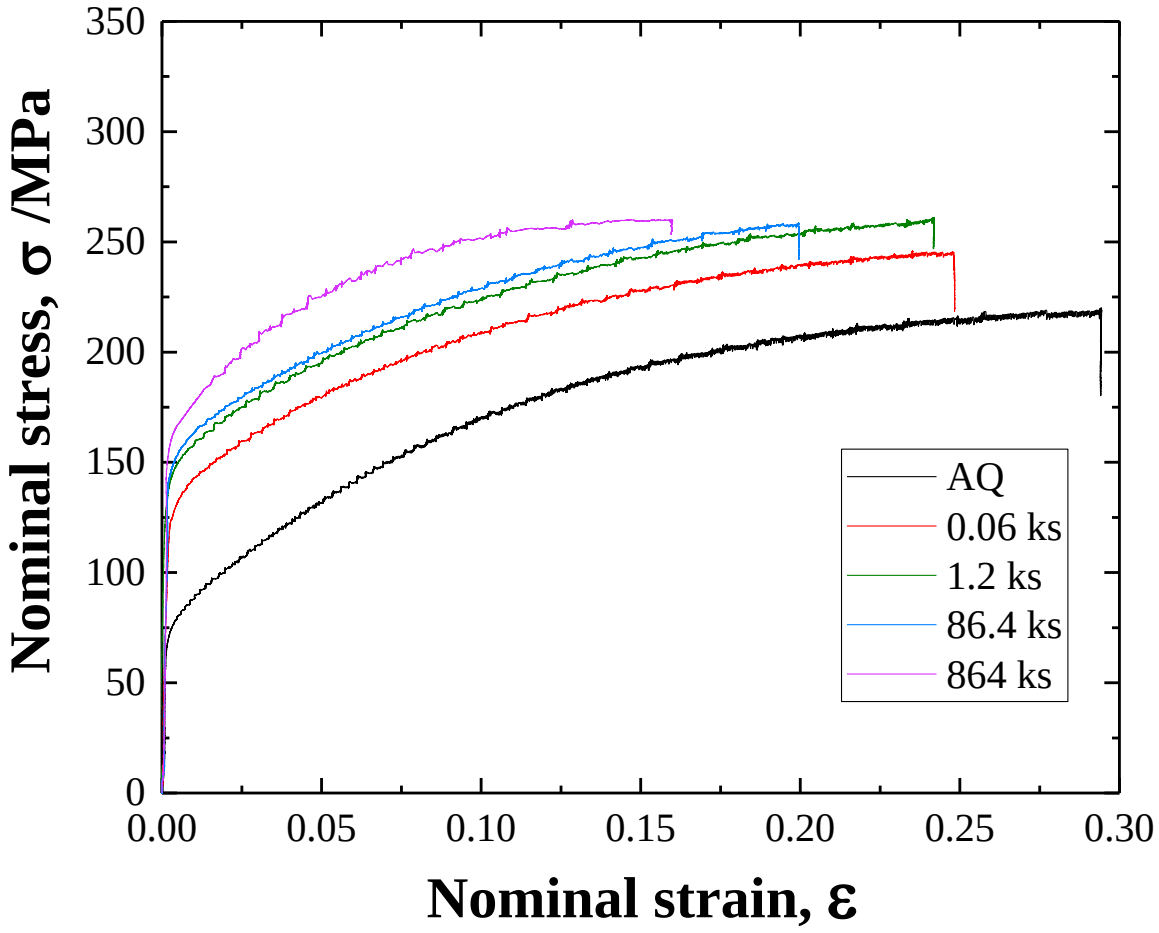

Fig. 4.6 Stress-strain curves for the 3M1C aged at 443 K for various times.

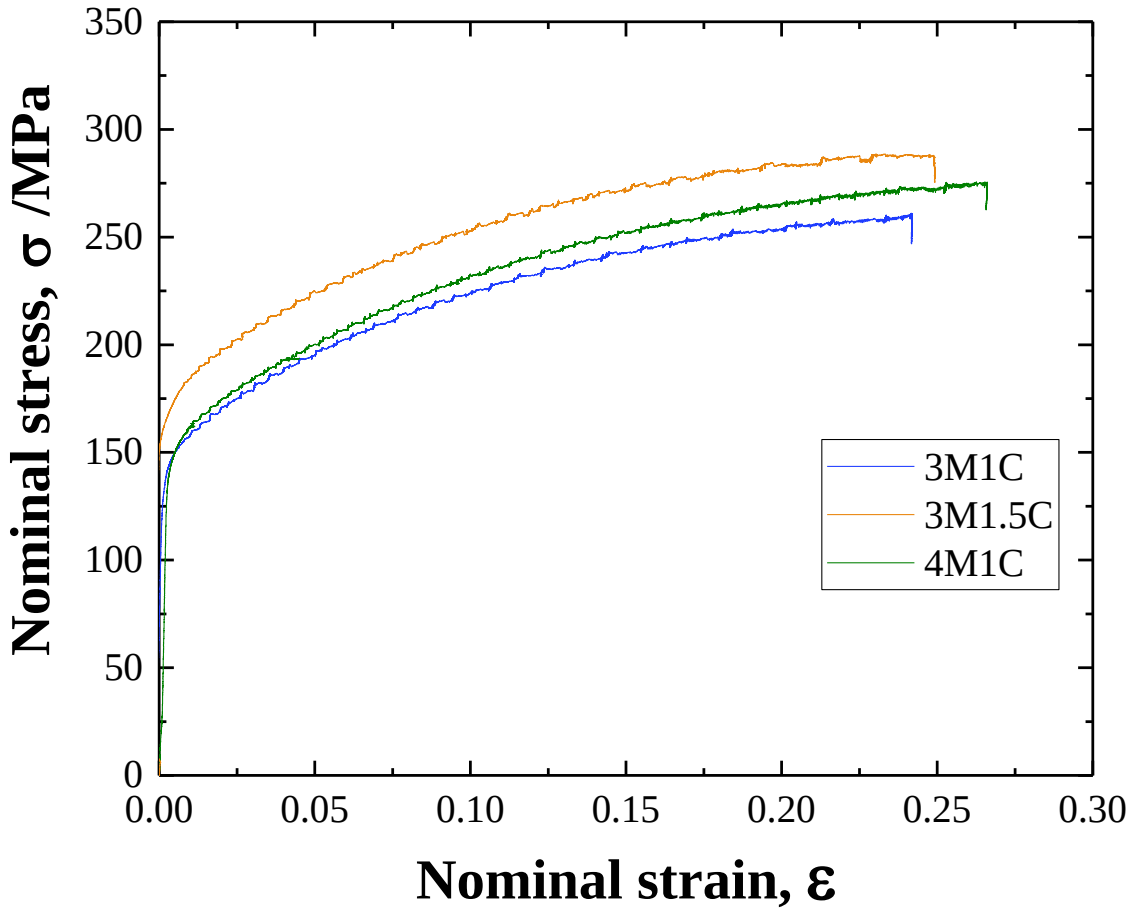

Fig. 4.7 Stress-strain curves for the investigated alloys aged at 443 K for 1.2 ks.

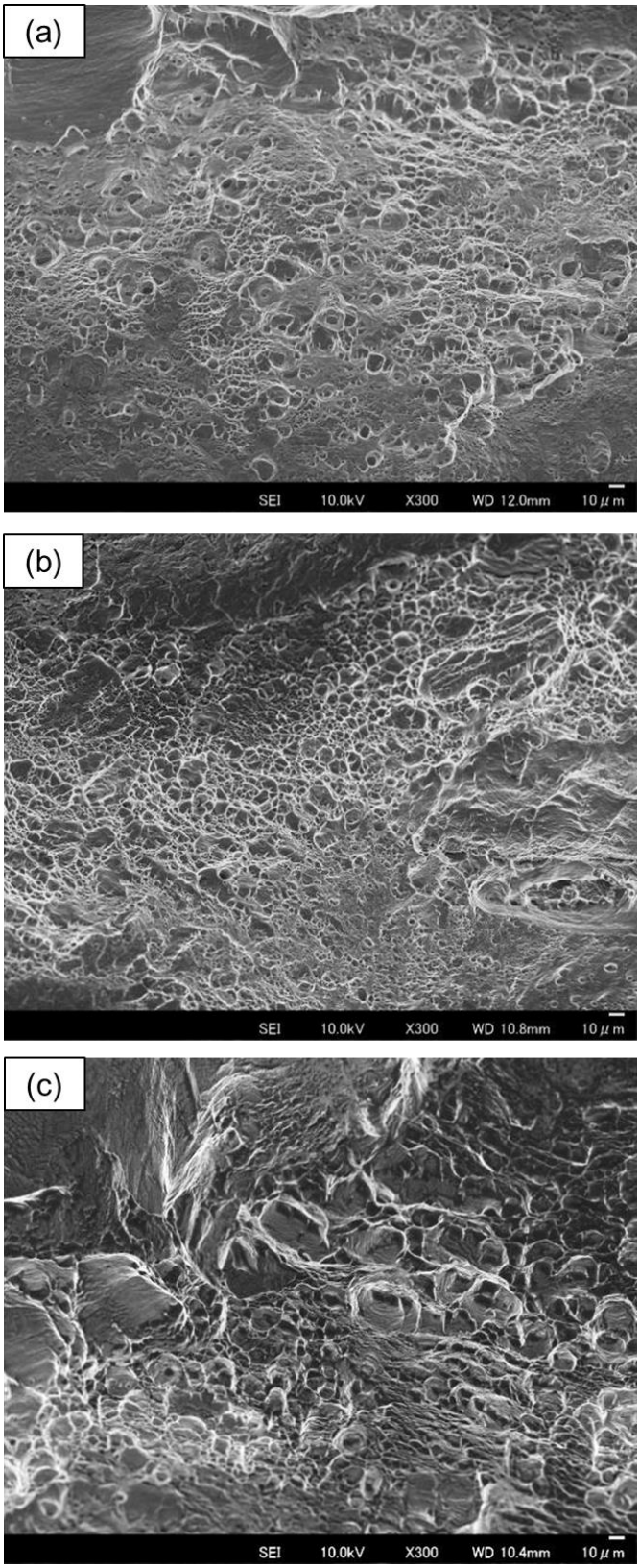

Fig. 4.8 Fracture surface of the (a)3M1C, (b)3M1.5C and (c)4M1C alloys aged at 443 K for 1.2 ks.

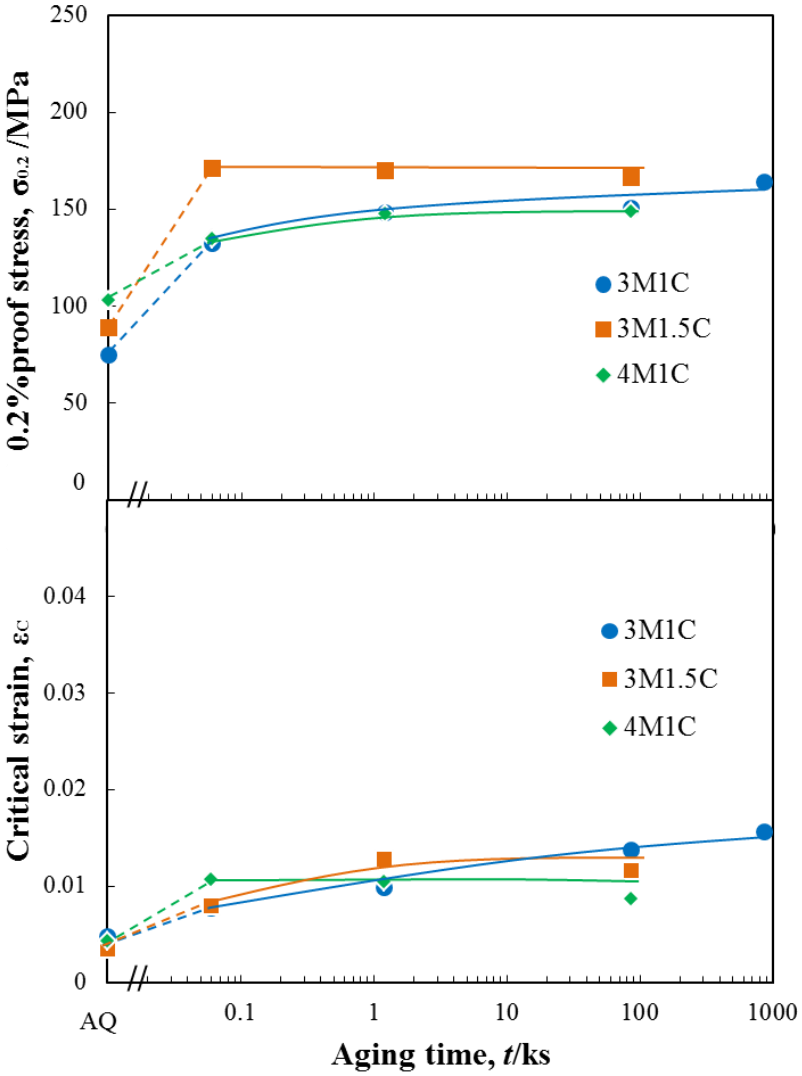

Fig. 4.9 Variation for the (a) 0.2 % proof stress and (b) critical strain for 3M1C, 3M1.5C and 4M1C alloys with aging time at 443K.

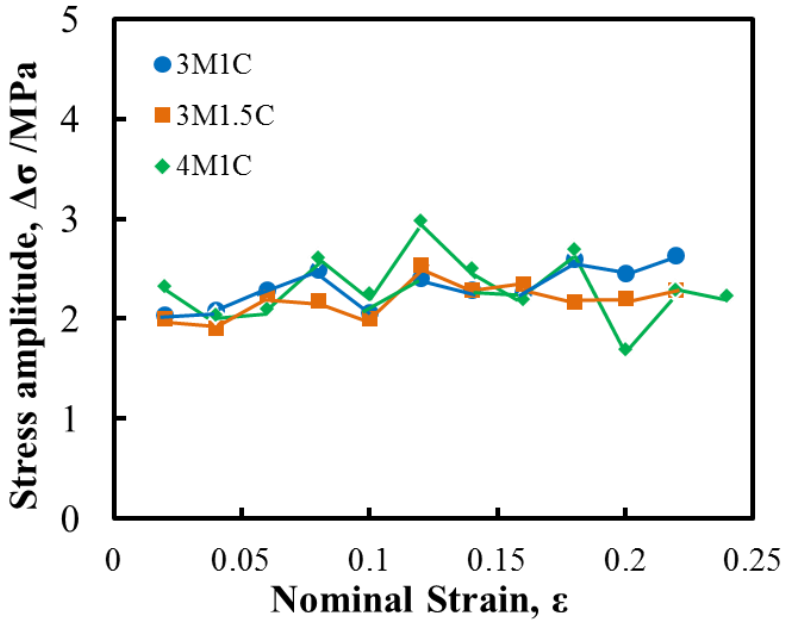

Fig. 4.10 Variation of the stress amplitude for the 3M1C, 3M1.5C and 4M1C alloys with aging time at 443K.

Chapter 5

Effect of Small Addition of Ag on Age-hardening Behavior in an Al-Mg-Cu alloy

5.1 Introduction

Small additions of particular alloying elements have been recognized to be effective in controlling Al-Mg-Cu alloy precipitate microstructure and properties [1-4]. According to several reports [4-7], silver is one of such elements with a tremendous influence on the age-hardening response. It has been reported that the trace addition of Ag can promote the formation of three different phases depending on the Cu/Mg ratio [8-10]. A micro-beam electron diffraction (MBED) study by Chopra et al. [9] indicated that the fine precipitates in the Al-1.5Cu-4.0Mg-0.5Ag (wt %) alloy which lie in (α+S+T) phase field are not isomorphous with the T phase. They proposed that the hardening precipitate in this alloy is the Z-phase. Hirosawa et al. [4] and Ringer et al. [6] also concluded that Ag enhances age-hardening by promoting precipitation of the Z-phase. Recently, Kubota et al. [11, 12] reported that precipitates having a quasi-crystalline structure is formed as the primary strengthening phase in the Al-10Mg-0.5Ag (wt%) alloy. The quasi-crystalline phase in this alloy is structurally related to T-$Mg_{32}(Al, Ag)_{49}$ by similar internal atomic clusters, so called Bergman-type atom clusters [13-15]. Once again it has been reported that trace addition of Ag can promote an increased age-hardenability. Since the investigated alloys in the present study lie in (α+S+T) phase field, the effect of the addition of Ag is of particular interest from both engineering and academic aspects. Furthermore, it is important to clarify the role of Ag and vacancies during the initial decomposition. In this chapter, the effect of trace addition of Ag on the age-hardening response in an Al-3Mg-1Cu (wt %) alloy is investigated. The alloys are prepared by high-purity materials in order to remove the influence of impurity elements and clarify the effect of the small addition of Ag.

5.2 Experimental procedure

5.2.1 Alloy compositions

The chemical composition of the alloys utilized in this chapter is listed in **Table 5.1**.

5.2.2 Heat treatment

Samples were solution treated in a salt bath at 793 K and kept for 3.6 ks, followed by quenching in ice-water and held for 60 s. The aging treatment was carried out in an oil bath at 443 K.

5.2.3 Hardness, Electrical resistivity and DSC

Hardness, electrical resistivity and DSC measurements were conducted in the same procedure as described in the Chapter 2.

5.2.4 TEM

Specimens for TEM measurement were prepared by electro-polishing with a Tenupol 5 machine (Struers). The TEM investigations including HAADF-STEM observations were conducted in the same procedure as described in the Chapter 2.

5.2.5 PAS

The two main experimental techniques of PAS, positron annihilation lifetime spectroscopy (PALS) and coincidence Doppler broadening (CDB) were utilized to investigate the decomposition phenomena during aging, especially evolution of the vacancy-like defects. PALS and CDB measurements were conducted in the same procedure as described in the Chapter 3.

5.3 Results

5.3.1 Effect of Ag Addition on Age-hardening Response

I. Hardness and Electrical Resistivity Changes During Aging at 443 K

The hardness change for the Ag-added alloy during aging at 443 K is shown on the top of **Fig. 5.1**. For comparative purpose, the hardness change for the Base alloy is also shown. In consistent with the Base alloy, the Ag-added alloy shows two distinct hardening stages separated by a plateau. The hardness of the Ag-added alloy increased significantly and the overall hardness is consistently higher than that of the Base alloy (a difference up to ~25 HV). In addition, the plateau stage is shortened by Ag addition. Both alloys reach their maximum hardness after similar aging time. In the Ag added alloy, the initial increase in the electrical resistivity is smaller than that of the Base alloy, however the resistivity decreases more rapidly as aging proceeds (the bottom of **Fig. 5.1**), suggesting that formation of precipitates which causes the decrease in the resistivity is strongly promoted by Ag addition.

II. Microstructural Evolution During Aging

Figure 5.2 shows TEM microstructures with SA diffraction patterns for the Ag-added alloy aged at 443 K for (a) 10.8 ks (b) 432 ks, and (c) 950.4 ks, respectively. From the bright field images, it is evident that the addition of Ag has a drastic effect on the precipitate microstructure. In contrast with the Base alloy (**Fig. 2.10**), fine, homogeneous precipitates are observed. Although the contrast of the precipitates is quite different between the Base and Ag-added alloys, the weak spots in the selected area diffraction patterns in **Fig. 5.2 (a)** and **Fig. 2.10 (a)** are surprisingly similar. This indicates that they originate from the same type of initial GPB zones / clusters. **S**ize distributions of the precipitate in diameters in **Fig. 5.2** are summarized in **Fig. 5.3**. The precipitates follow a double distribution from the early stages, suggesting the existence of two types of precipitates. The smallest precipitates disappear

gradually with aging time. At the peak hardness, the microstructure comprises a dense and homogeneous distribution of ~10 nm fine precipitates [**Fig. 5.2 (c)**]. A relatively small amount of coarser precipitates of the lath-shaped S' phase exists after prolonged aging, mainly associated with dislocations.

III. HAADF-STEM Investigation for the Ag-added Alloy Aged for 950.4 ks

After aging for 950.4 ks, two types of precipitates, (i) uniformly distributed fine precipitates and (ii) small amount of S' phase, were detected in the Ag-added alloy.

(i) Evolution of uniformly fine precipitates in the Ag-added alloy agrees with the previous observations [6, 9, 10], where Ag was found to promote the formation of the fine distributed Z phase which was also found in the present study on the Ag- free Base alloy. The weak, squarely arranged spots in the SADPs in **Fig. 5.2(b), (c)** do not match the ones between the Al reflection spots in the nano-beam diffraction pattern in **Fig. 2.14(a)**. A detailed investigation showed that the weak spots were more likely to originate not from a single zone axis, but from precipitates oriented in the Al matrix with some high symmetry zone parallel with $<100>_{Al}$ directions. High resolution HAADF-STEM images of the precipitates taken in $<112>_{Al}$ zones indicates that they were disordered, but showed a 5-fold symmetry [**Fig. 5.4 (a)**]. **Figure 5.4 (b)** shows the contrast-improved inverse transformed image with the FFT image from a part of the particle in an Al zone, annotated by 'i_5' (to suggest 'icosahedral' arrangement). The image is overlaid by pentagons with vertices defined to the high intensity columns/positions. The FFT image shows a ring of strong spots of near 5-fold intensity distribution [inset in **Fig. 5.4 (b)**]. The weaker spots of the inner ring are less perfectly arranged. The pseudo-pentagonal symmetry and lack of overall periodicity strongly suggest the main precipitate in this alloy is an icosahedral quasi-crystal (iQC).

Kubota et al. [11, 12] reported that the addition of 0.5 wt% Ag promoted the precipitation in Al-5Mg and Al-10Mg alloys. In spite of the much higher Mg content in his alloys, the small, often spherical precipitate shape, distribution and the SA diffraction intensity visible in his patterns of the Ag-containing alloys have clear similarities with the present observations (**Fig. 5.5 (a)-(c)**). Thus, the fine precipitates observed in current study are likely to be the similar icosahedral quasi-crystalline (iQC) particles. They also demonstrated the similarity between the iQC particles and the T-$Mg_{32}(Al, Ag)_{49}$ phase both in diffraction and in composition [11]. Kubota et al. also found that the cube cells of α-Al and T to be parallel. Since T is an approximation phase to the iQC (related to the iQC of the Al-Mg-Zn system [13]), if composition and heat-treatment is not optimal, it is likely that small regions of T could coexist with the iQC, explaining the pseudo 5-fold pattern in **Fig. 5.4(b)**.

Fig. 5.6 shows (a) the enlarged SADP for the Ag-added alloy aged for 950.4 ks, (b) the diffraction pattern for the T phase and (c) schematic illustration of the diffraction pattern for the T phase [16]. In **Fig. 5.6 (c)**, solid, red and open circles show the spots from Al matrix, T phase and double diffraction, respectively. red and open circles are overlaid in SADP for the Ag-added alloy [**Fig. 5.6 (a)**]. The patterns in **Fig. 5.6 (a)** correspond with the T phase. Therefore, the fine precipitates are icosahedral quasi-crystals intermixed with small regions of the cubic approximation T phase.

(ii) S’ phase observed in the Ag-added alloy aged at 443 K for 950.4 ks is shown in **Fig. 5.7**. Ag has the effect of refining the particles and giving more roundish cross-sections. The orientation relationship between Al matrix and S’ phase is the same as for the Base alloy. The absence of the crosses which was observed in the SADP of **Fig.2.10 (c)** indicates that S' phase must be relatively sparse in the Ag-added alloy. The amount was not quantified.

The S' particle in **Fig. 5.7** has strong contrast columns at the boundary with intensity varying from place to place; the upper right part contains a darker region, whereas most of the left interface contains strong contrast columns breaking the normal period. It is likely, but still unclear how these effects are related to Ag. More dedicated experiments would be needed to determine where the Ag atoms are.

IV. DSC Analysis

Figure 5.8 shows DSC curves for the Ag-added alloy aged at 443 K for various times. For comparison, a curve for A.Q. specimen of the Base alloy is also shown. In a curve for A.Q. specimen of the Ag-added alloy, there is a large exothermic peak A at around 380 K. At around 540 K, 610 K, there are two exothermic peaks named peak E and F, respectively. The exothermic Peak B are not observed in the Ag-added alloy. An endothermic peak appears at around 490 K. This peak is attributed to the dissolution of precipitates whose formation give rise to peak A. In order to characterize the three exothermic peaks (A, E and F in **Fig. 5.8**), various heating rate are applied to DSC measurement. **Figure 5.9** shows DSC curves with different heating rate from 2 to 20 K/min. The Kissinger method is applied to determine the activation energy for the precipitation process using peak temperature in DSC curves. **Figure 5.10** shows $\ln(\gamma/T_P^2)$ versus $1000/T_P$ relationships. The activation energies for each peak are calculated from the slopes of the obtained relationships are summarized in **Table5.2**.

(i) The activation energy for peak A is much smaller than the activation energies for diffusion of alloying elements, Cu and Mg in Al (133.9 kJ/ mol and 120.5 kJ/ mol, respectively) [17]. Thus, the kinetics of the precipitation process which corresponds to peak A could be controlled by the migration of vacancies, in other words, Cu/Mg/Ag vacancy solute clustering. Peak A is fully disappeared after aging for 0.06 ks, where the hardness and electrical resistivity increase rapidly. The precipitates responsible for the peak A in the Ag-

added alloy might be vacancy-solute (Cu, Mg, Ag) complexes and are responsible for the rapid increase in the hardness and electrical resistivity. The value of the activation energy for peak A in the Ag-added alloy (81.7 kJ/mol) is larger than that of the peak A observed in the Base alloy (73.9 kJ/mol). Based on the first principle calculation, Ag has strong positive binding energy (energetically favorable binding) with vacancy [18]. In addition, it has been reported that Ag atoms strongly participated into precipitates when Ag is microalloyed to Al-Cu-Mg alloys [6, 7]. Thus, Role of Ag atoms and vacancies during the initial decomposition will be discussed later.

(ii) The activation energy for peak E is close to the activation energies for diffusion of alloying elements, Cu and Mg in Al (133.9 kJ/ mol and 120.5 kJ/ mol, respectively). Thus, precipitation which corresponds to peak E could be controlled by Cu and Mg diffusion in Al. According to the microstructural observation, T phase is uniformly formed whereas the formation of S' phase is suppressed by Ag addition. Thus, peak E might be associated with the precipitation of T phase.

(iii) Peak F appears very small. According to the microstructural observation, the precipitate responsible for peak E is S' phase. The activation energy for the formation of S' phase is increased by Ag-addition (from 142.9 kJ/ mol to 151.2 kJ/ mol).

5.3.2 Microstructure Evolution During Initial Decomposition Stage

HAADF-STEM investigation are conducted for the Ag-added alloy aged at 443 K for 0.06 ks. **Figure 5.11** shows the HAADF-STEM image for the Ag-added alloy aged at 443 K for 0.06 ks. The contrast of the image in **Fig. 5.11** indicates there are substantial amounts of solute ordering. FFT in **Fig. 5.11** shows the same spots as the SADPs obtained for the Ag-added alloy aged for 10.8 ks [**Fig. 5.2 (a)**]. The FFT in **Fig. 5.11** is also the same as the FFT of the HAADF-STEM image for the Base alloy aged at the same condition (**Fig. 3.3**). Enlarged

HAADF-STEM images in **Fig. 5.12** indicates that the microstructure consists of a multitude of structural units of GPB zone (yellow circles) and spherical zones (red circles). Since the atomic column intensity in the HAADF-STEM images increases strongly with the atomic number [19], there is often high contrast around Ag atoms [20] because of the large atomic number (the atomic number of Ag, Cu, Mg and Al are 47, 29, 12 and 13 respectively). The high intensity of the atomic column in the structural units of GPB zone (**Fig. 5.13**) comparing to that of the Base alloy (**Fig. 3.5**) suggests that structural units of GPB zone in Ag-added alloy are enriched with Cu and/or Ag atoms. It seems that some units are part of the extended regions, thus the extended regions nucleated and grew around some of the structural units of GPB zone. The extended regions (spherical zones) observed in **Fig. 5.12** do not have a strong ordering, or unit cell and they mainly enriched fcc matrix. HAADF-STEM image taken in $<110>_{Al}$ zone for the Ag-added alloy aged at 443 K for 0.06 ks are shown in **Fig. 5.14** . There is no strong indication of preferential growth on $\{111\}_{Al}$ or $\{100\}_{Al}$, suggesting that the observed spherical zones do not have a high aspect ratio and they are more or less round in shape.

5.3.3 Positron Annihilation

I. PALS

Figure 5.15 shows the evolution of the positron lifetime and hardness for the Ag-added alloy during aging at 443 K. For comparison, the result obtained for the Base alloy is also shown in **Fig. 5.15**. The positron lifetime decreases rapidly in the initial, and then it starts to increase slightly, and finally it increases significantly corresponding to the increase in hardness at peak aging. The reduction of the lifetime in the initial is less marked compared to the reduction observed in the Base alloy. As described in **Chapter 3**, a decrease in positron lifetime is generally observed during initial stage of decomposition of Al-Cu based alloys and vacancy

trapping at Mg would cause the reduction of the lifetime drop. In the Ag-added alloy, the reduction of the lifetime drop is promoted and the overall lifetime value is consistently higher than that of the Base alloy. After the drop in lifetime value to 205 ps, it starts to increase slightly. This increase might be attributed to the transition of GPB zones to T phase. Misfit interfaces provide new trapping sites where positrons can survive with small overlap to matrix. The rapid increase in lifetime value occur at peak aging due to the formation of T phase.

II. CDB

Obtained Δ curves in **Fig. 5.16** show the CDB results presented as relative differences to the balk Al reference. In spite of the low composition of Cu (0.45 at%), strong Cu signal is observed (the structure peaked around ±2 atomic units, see the fingerprint of Cu in **Figure 3.2**). In order to estimate the fraction of alloy components in contact with vacancies, the obtained curves are analyzed by fitting a linear combination of momentum spectra measured for the pure elements through Eq. (3.9). **Figure 5.17** shows the fitting results. There is an excellent agreement between the Δ curves corresponding to the fitting curves (red curves). **Table 6.3** summarizes the obtained fractional concentrations of the alloy components in contact with vacancy-like defects in the Ag-added alloy for different aging conditions. F_{trap} is the trapping fraction of the positrons annihilated in the solute-vacancy clusters or nanoprecipitates. The complementary percentage (100 %- F_{trap}) represents the fraction of positrons annihilated into the matrix. According to the results, 58-63 % of positrons are trapped and annihilated in solute-vacancy clusters or nanoprecipitates in the Ag-added alloy under the aging conditions. This value is larger than that of the Base alloy, suggesting that Ag addition promotes the vacancy-like defects to be retained after quenching and during aging.

Fractional concentrations of the alloy components in contact with vacancy-like defects are also plotted in **Fig. 5.18**. The obtained results are summarized as follows,

(i) At A.Q. state, the amount of Mg and Ag is almost the same. The amount of Cu is more than three times that of Mg and Ag.

(ii) After aging for 0.06 ks, the amount of Al strongly decreases, the amount of Mg increases twofold, the amount of Cu increases in 50 % and the amount of Ag increases in 70 %.

(iii) After aging for 3.6 ks, the amount of Al slightly decreases, the amount of Mg and Ag stay constant and the amount of Cu slightly increases.

By Ag addition, the fractional concentration of Mg atoms after aging for 0.06 ks is increased. It is revealed that the initial decrease in lifetime value (**Fig. 5.16**) is related to the strong increase in the Cu, Mg and Ag content in contact with vacancies. The vacancy-solute (Cu, Mg, Ag) complexes might be formed after short term aging.

5.4 Discussion

5.4.1 Evolution of Structural Units of GPB Zone

By addition of Ag, the microstructure was changed drastically (**Fig. 5.2**). In spite of the quite different microstructure between the Base and Ag-added alloy after aging for 10.8 ks [**Fig.5.2 (a)**], there were no additional diffraction spots in the SADP compared with the Base alloy. HAADF-STEM investigation for the Ag-added alloy aged for 0.06 ks revealed that structural units of GPB zone are formed. In addition, GPB zones are formed after aging at 443 K for. Some of the structural units are found to be part of the spherical zones. It indicates that the formation of the spherical zone is originated from the structural units of GPB zone. In the Base alloy, formation of the structural units are confirmed after aging for 0.06 ks. Therefore, it is revealed that in both alloys the evolution of the microstructure originates from the same

nanostructure, i.e. structural units of GPB zone. This is the main reason that the SADPs and FFT of both alloys aged for 10.8 ks **[Fig. 2.10 (a) and Fig. 5.2 (a)]** and 0.06 ks [**Fig. 3.3** and **Fig. 5.11**] show the same spots. Furthermore, since the GPB zones in the Ag-added alloy do not have a strong ordering, there are no extra spots in the FFT (**Fig. 5.11**).

In both alloys, the evolution of exothermic peak A was observed during DSC scan for the A.Q. state specimen (**Fig. 2.15** and **Fig. 5.8**). In the Base alloy, peak A is associated with the formation of structural units of GPB zone. In contrast, in the Ag-added alloy, the peak A is associated with the formation of the structural units of GPB zone and spherical zones, since those structural units and zones are already formed after aging for 0.06 ks. This is the reason that Ag addition changed the activation energy from 79.9 kJ/ mol to 81.7 kJ/ mol for the peak A. This is also in agreement with the disappearance of the exothermic peak B which is associated with the formation of the GPB zones.

5.4.2 Role of Vacancies and Ag Atoms During the Initial Decomposition

In a FCC structure, one atomic site has 12 first neighbour atoms. Therefore, around a vacancy-like defect there are 12 first neighbor atoms. The results of the fractional concentrations of the alloy component in contact with vacancy-like defects C_i (**Table 6.2**) can be roughly interpreted as follows:

$$\left(C_{Al} = \frac{N_{Al}}{12}, C_{Mg} = \frac{N_{Mg}}{12}, C_{Cu} = \frac{N_{Cu}}{12}, C_{Ag} = \frac{N_{Ag}}{12} \right) \tag{6.1}$$

where, N_{Al}, N_{Mg}, N_{Cu} and N_{Ag} are the average number of Al, Mg, Cu and Ag atoms around a vacancy.

(i) Aging after 0.06 ks: Around a vacancy, there approximately 2 Mg atoms, 4 Cu atoms, 1 Ag atom and the rest are Al atoms.

(ii) Aging after 3.6 ks: Around a vacancy, there approximately are 2 Mg atoms, 5 Cu atoms, 1 Ag atom and the rest are Al atoms.

The results indicates the formation of the vacancy-solute (Cu, Mg, Ag) complexes during aging. Small addition of Ag strongly promoted the vacancies to be retained after quenching and during aging. Thus, formation of the structural units of GPB zone and spherical zones is accelerated by Ag addition.

5.4.3 Double Distribution of the Size of Precipitates

Size distribution of the precipitates in the Ag-added alloy aged for (a) 10.8 ks, (b) 432 ks and (c) 950.4 ks is shown in **Fig. 5.3**. The precipitates follow a double distribution, suggesting the existence of two types of precipitates. According to the microstructural investigation, the double distribution can be understood as shown in **Fig. 5.19**. The small (～5 nm)precipitates which is corresponds to the GPB zones disappear gradually with aging time. After long term aging, the microstructure comprises a dense and homogeneous distributed T phase. Structural units of GPB zone appear as the smallest precipitates in **Fig. 5.19**.

5.4.4 Relation Between T Phase and Z Phase

The precipitation sequence leading to the formation of S phase is well established in Al-Cu-Mg system. However, the precipitation sequences of T phase and Z phase are not clear. The unit cell of T-$Mg_{32}(Al, Zn)_{49}$ contains 162 atoms, in two Bergmann clusters, which each can be viewed as constructed by several layers or concentric atomic shells [13, 21]. The structure of the Z phase is not known. The Z phase is not an isomorph of the T-phase [8] but may still be structurally related.

It has been proposed that Ag addition promotes the precipitation of a finely distributed metastable T phase in Al-Cu-Mg alloys with high Mg to Cu composition ratio which lie in the (α+S+T) phase fields. However, the existence of the T phase in Al-Cu-Mg-Ag system was based only on the visual observations of X-ray intensities which shows similarity to the T phase observed in the Al-Zn-Mg system. Chopra et al. [8] re-examined an Al-1.5Cu-4Mg-0.5Ag (wt %) alloy which lie in (α+S+T) phase field and clarified that the obtained precipitates were not isomorph of the T phase designated by Bergman et al.. The precipitates observed in the alloy were newly designated as Z phase. However, in the present study, Z phase was found to form in the ternary Al-Mg-Cu alloy. In contrast, the T phase was found to form in the Ag-added alloy.

Recently, Xia et al. reported that Z' phase coexists with GPB zones and S phase in an Al-1.5Cu-0.4Mg-0.25Ge at peak aged condition (25 h at 200 ℃) [27]. In their study, Ge promoted the formation of Z phase, although Ge did not partition into the Z' phase. Based on the analysis of diffraction patterns, they described that Z' phase represents quasiperiodicity in some directions and crystalline periodicity in other directions. The latter exhibits the characteristics of a fcc structure with lattice parameter a≒2 nm. The Z' phase transformed into the more stable fcc structure, Z phase, in over-aged condition.

In the present study, such quasiperiodic arrangements were not observed in the microstructures of the Base alloy. However, the intensity distribution along the $<111>_Z$ direction seen in the diffraction patterns in **Fig. 2.15** bears the mark of icosahedral symmetry of internal building blocks. For example, along the $<111>_Z$ direction, without considering extinctions and other diffraction effects the intensity is increasing as the first, second, third, and fifth spots. This is clearer from the images (e.g. Fig. 2) of Chopra's dedicated study of the Z phase [8]. These numbers are the Fibonacci numbers, closely connected with the geometry

of the icosahedron and the icosahedral quasicrystals and are reflected in the approximation phases. This is therefore a strong indication that Z is also an approximation phase for the iQC phase. Approximation phases are based on the same units as the parent quasi-crystal but can differ widely in structure type [22, 23]. Further studies are needed in order to understand the structural connections existing between the T phase, the Z phase and the iQC phase.

5.5 Conclusions

1. The age-hardenability of the Base alloy is significantly improved by small amount of Ag addition. Ag addition reduces the activation energy to form nanostructure during the initial decomposition and promotes the formation of uniformly distributed fine precipitates on further aging.
2. The pseudo-pentagonal symmetry and lack of overall periodicity suggested that the dense precipitates are icosahedral quasi-crystals. HAADF-STEM showed the icosahedral quasi-crystals tended to deviate from perfect symmetry, because of an inter-mix with the cubic approximation T phase. S' phase was found to be smaller to that of the Base alloy, with a more roundish cross-section.
3. In the initial stage of aging, In the initial stage of aging, structural units of GPB zone are formed and they grow to form zones which has spherical shape. Ag addition accelerate the formation of the spherical zones, resulted in the large increase in the hardness during rapid age-hardening.
4. PAS investigation clarified that Ag addition promotes more vacancies to be retained after quenching. In addition, the initial decrease in lifetime value is related to the strong increase in the Cu, Mg and Ag content in contact with vacancies, suggesting the formation of vacancy-solute (Cu, Mg, Ag) complexes from the early stage of aging.

Reference

1) I. J. Polmear, S. P. Ringer, J. Jpn. Inst. of Light Metals 50 (2000) 633-642

2) S. Hirosawa, T. Sato, Metals 73 (2003) 191-195

3) T. Sato, S. Hirosawa, K. Hirose, T. Maeguchi, Metall. Mater. Trans. 34A (2003) 2745-2755

4) S. Hirosawa, T. Omura, Y. Suzuki, T. Sato, Mater. Sci. Forum 519-521 (2006) 215-220

5) P. I. Gouma, D. J. Lloyd, M. J. Mills, Mater. Sci. Eng. A 319-321 (2001) 439-442

6) S. P. Ringer, G. C. Quan, T. Sakurai, Mater. Sci. Eng. A 250 (1998) 120-126

7) C. Li, G. Sha, B. Gun, J. H. Xia, X. F. Liu, Y. Y. Wu, N. Birbilis, S. P. Ringer, Scripta Mater. 68 (2013) 857-860.

8) H. D. Chopra, B. C. Muddle, I. J. Polmear, Phil. Mag. Lett. 73 (1996) 351-357.

9) H. D. Chopra, L. J. Liu, B. C. Muddle, I. J. Polmear, Phil. Mag. Lett. 71 (1995) 319-324.

10) I. J. Polmear: Light Alloys, 4th ed, Elsevier / Butterworth-Heinemann, Amsterdam (2006).

11) M. Kubota, J. F. Nie, B. C. Muddle, Mater. Trans. A 46 (2005) 1278-1287

12) M. Kubota, PhD thesis: The precipitation hardening response in Al-Mg(-Ag) alloys, Aug. 2001, Monash University, Dept. Mater. Eng., Clayton, Victoria 3168, Australia

13) M. Audier, P. Guyot, *Extended Icosahedral Structures,* San Diego: Academic Press (1989).

14) G. Bergman, J. L. T. Waugh, L. Pauling, Nature, 169 (1952) 1057-1058.

15) G. Bergman, J. L. T. Waugh, L. Pauling, Acta Cryst. 10 (1957) 254-259.

16) T. Omura, Mater thesis, Tokyo Institute of Technology (2005).

17) Yong Du, Y.A. Chang, Baiyun Huang, Weiping Gong, Zhanpeng Jin, Honghui Xu, Zhaohui Yuan, Yong Liu, Yuehui He, F.-Y. Xie, Materials Science and Engineering A363 (2003) 140–151.

18) C. Wolverton , Acta Materialia 55 (2007) 5867–5872.

19) P.D. Nellist and S.J. Pennycook, Adv. Imaging Electron Phys. 113 (2000) p.147.

20) C.D. Marioara, J. Nakamura, K. Matsuda, S.J. Andersen, R. Holmestad, T. Sato, T. Kawabata and S. Ikeno, Philosophical Magazine 92 (2012) 1149–1158.

21) M. Audier, P. Guyot, Extended Icosahedral Structures, San Diego: Academic Press (1989).

22) K. Hiraga, T. Ohsuna, K. Sugiyama, Rigaku Journal 16 (1990) 38-45.

23) W. Steurer, Z. Kristallogr. 219 (2004) 391-446.

24) G. Eger, Int. Z. Metallographie, 4 (1913) 50-128.

25) G. Bergman, J.L.T. Waugh and L. Pauling, Acta Cryst. 10 (1957) 254-259.

26) R. Vogel, Z. Anorg. Chem. 107 (1919) 265-307.

27) J.H. Xia, G. Sha, Z.G. Chen, X.Z. Liao, H.W. Liu and S.P. Ringer, Philosophical Magazine Letters 93 (2013) 77–84.

Table 5.1 Chemical compositions of the investigated alloys.

(wt %)

Sample	Mg	Cu	Ag	Si	Fe	Ti	Al
Base alloy	3.04	1.01	-	0.01	0.01	0.00	Bal.
Ag-added alloy	3.05	0.99	0.41	0.00	0.00	0.00	Bal.

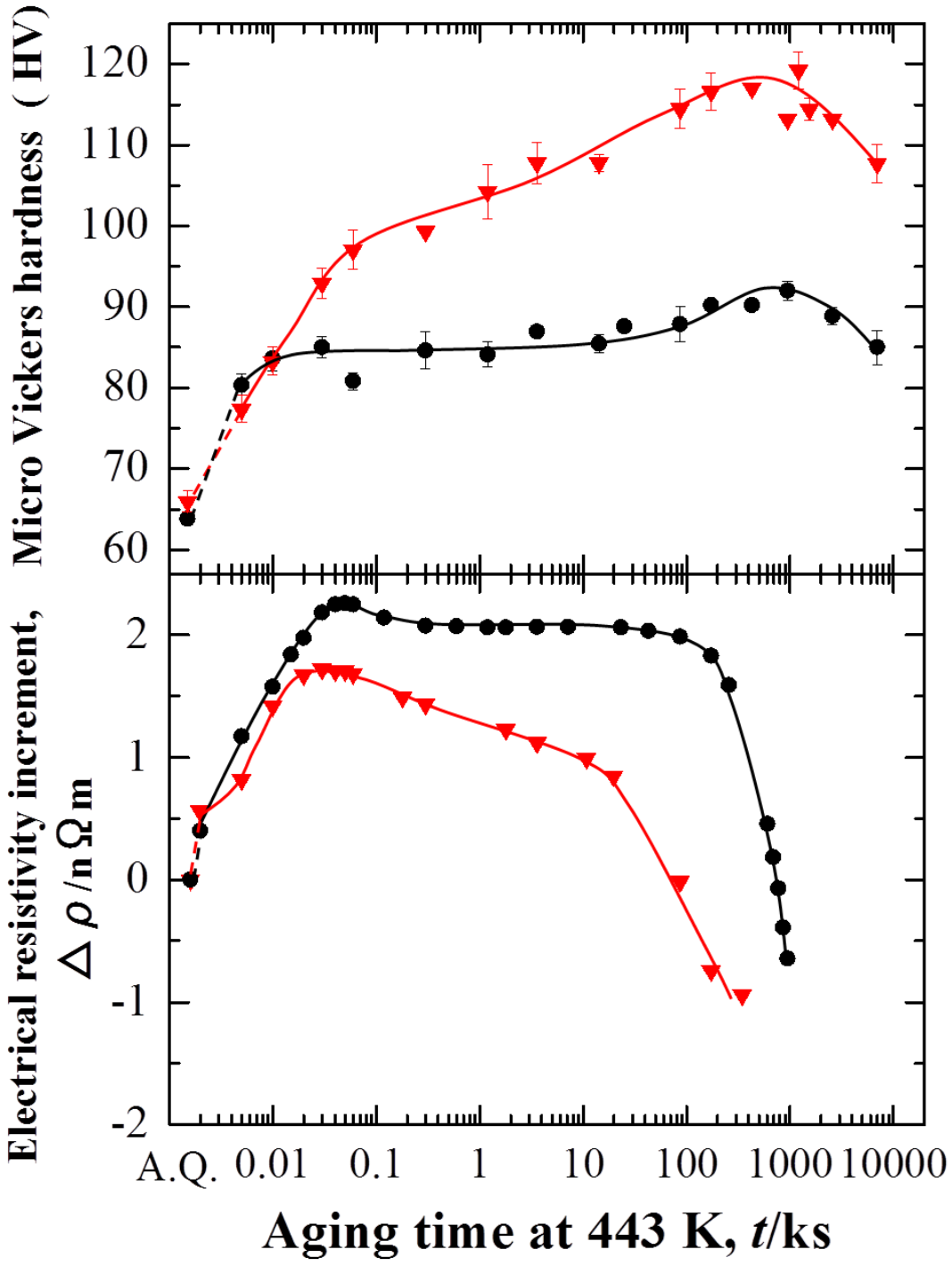

Fig. 5.1 Hardness and electrical resistivity changes for the Ag-added alloy during aging at 443 K.

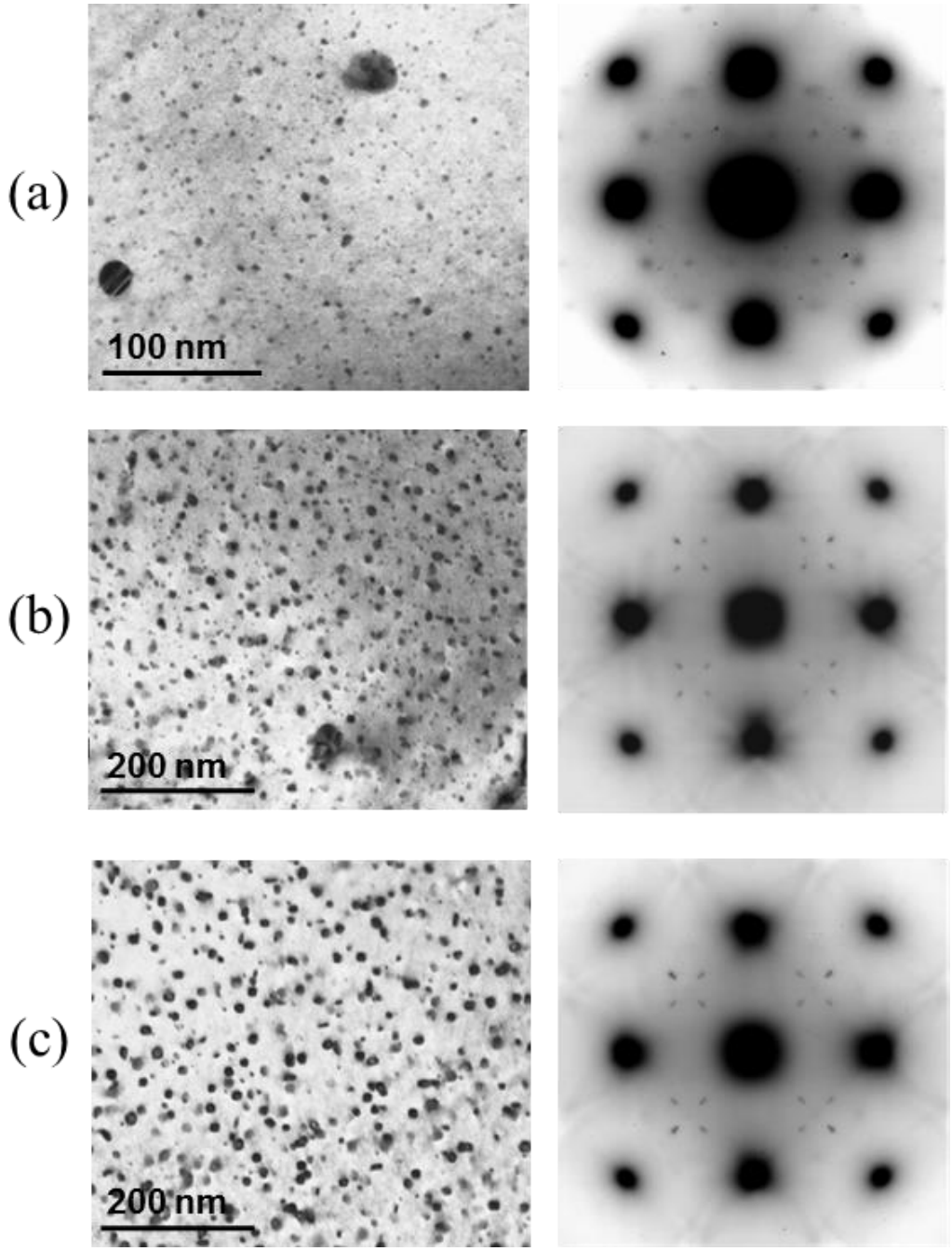

Fig. 5.2 Bright field TEM images with selected area diffraction patterns taken along $<001>_{Al}$ for the Ag-added alloy aged at 443 K for (a) 10.8 ks, (b) 432 ks, and (c) 950.4 ks. The aging times correspond to the plateau, the peak, and above the peak, respectively.

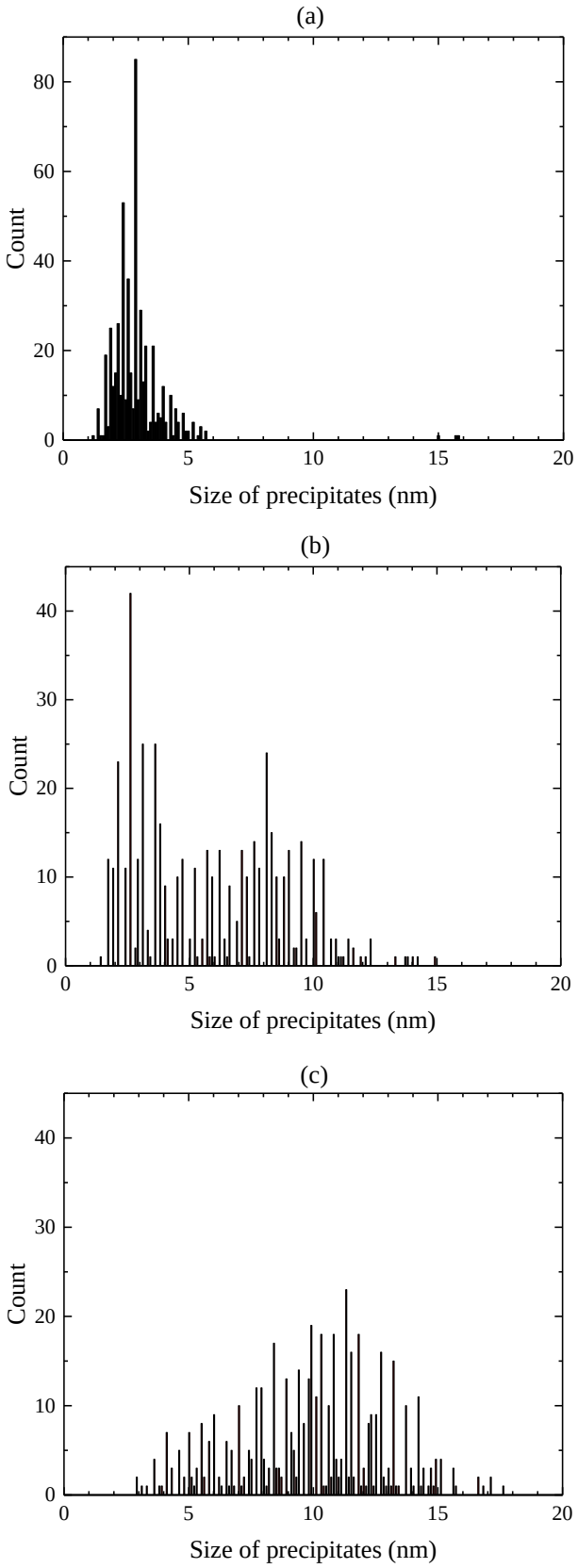

Fig. 5.3 Size distribution of the precipitates in the Ag-added alloy aged at 443 K for (a) 10.8 ks, (b) 432 ks and (c) 950.4 ks.

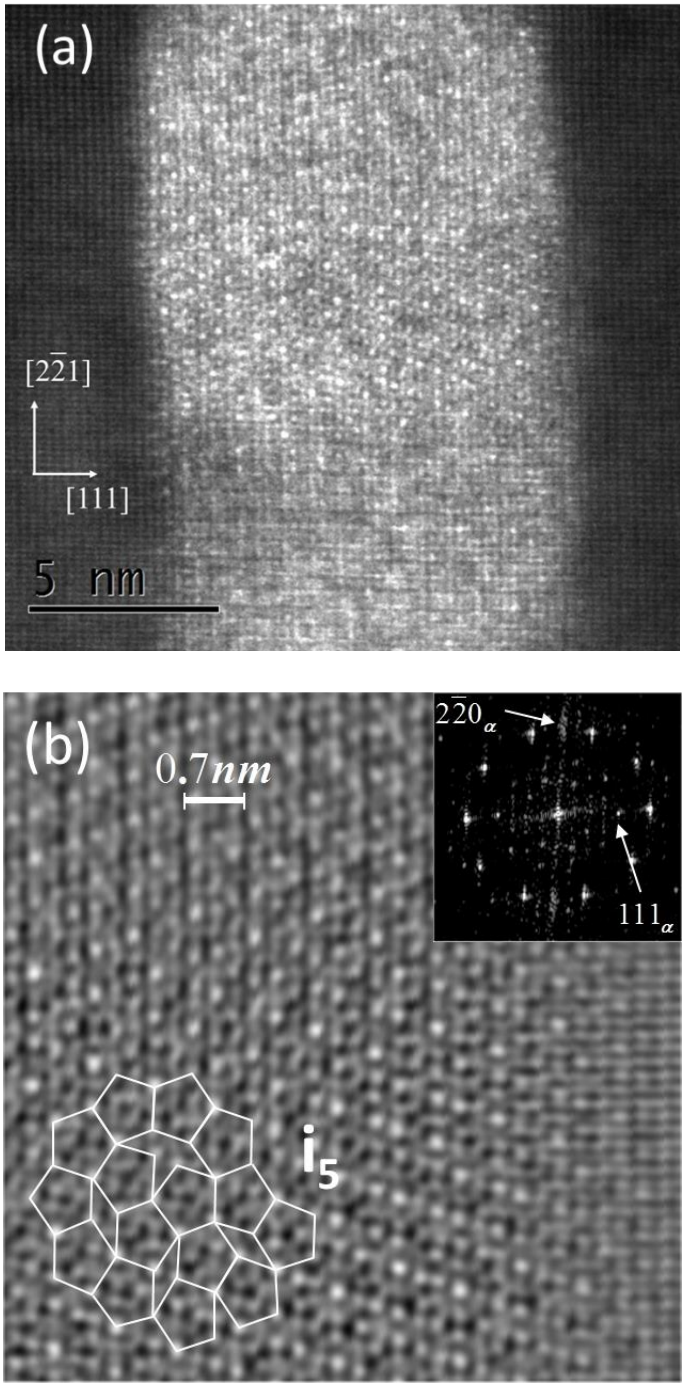

Fig. 5.4 HAADF-STEM image in a <112> $_{Al}$ zone of a typical precipitate in the Ag-added alloy aged at 443 K for 950.4 ks. (a) Region 'i_5' has 5-fold local symmetry. An enlarged magnification is shown in (b).

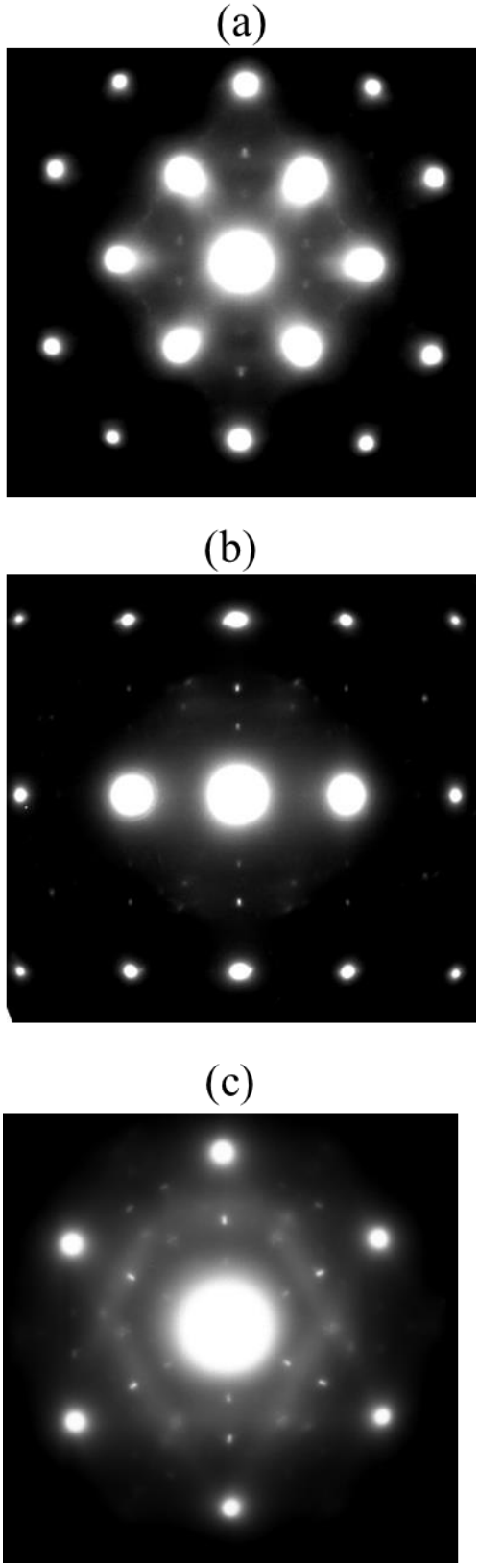

Fig. 5.5 Selected area diffraction patterns taken along the (a) $<110>_{Al}$, (b) $<112>_{Al}$, (c) $<111>_{Al}$ for the Ag-added alloy aged at 443 K for 950.4 ks.

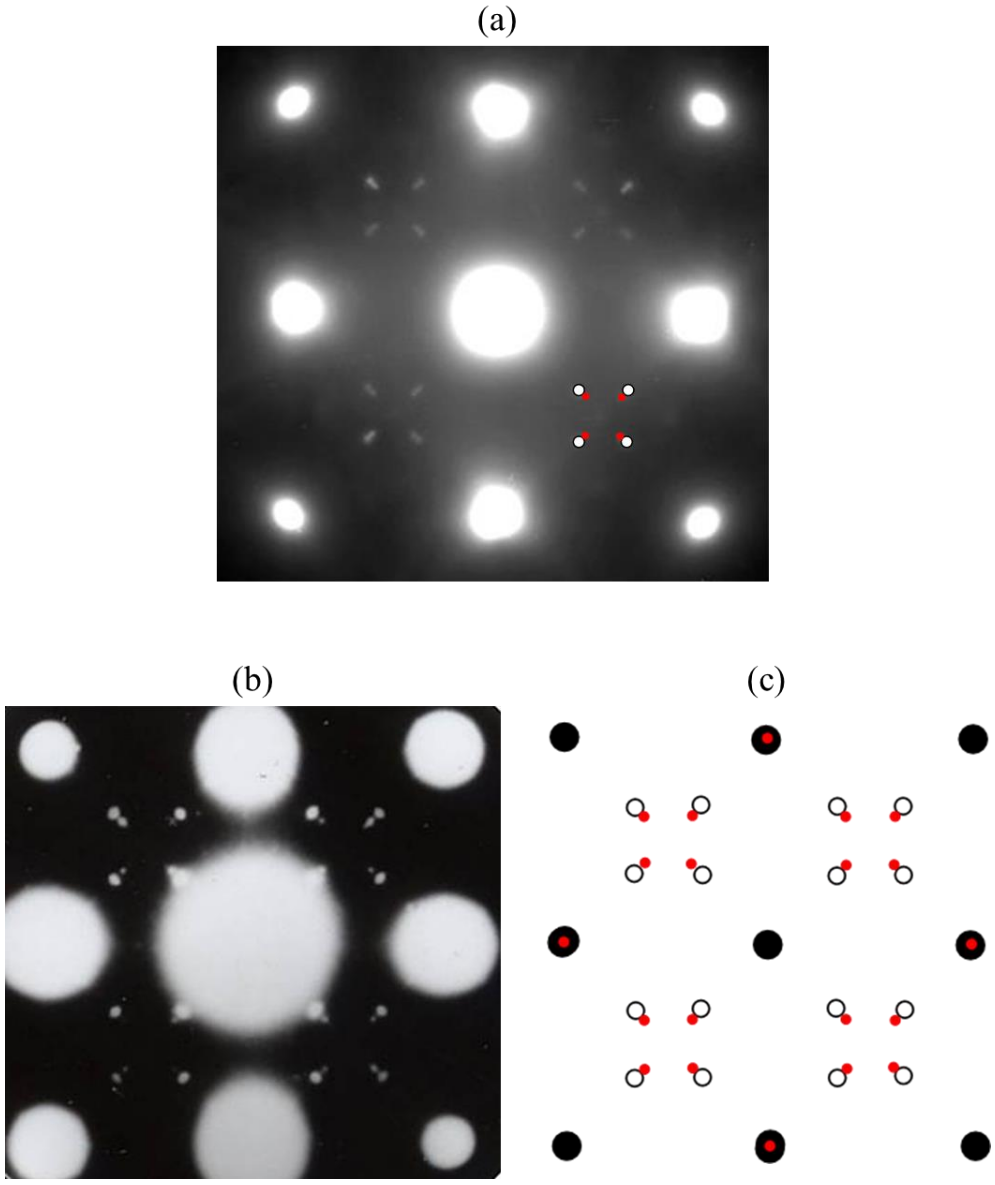

Fig. 5.6 (a) Enlarged SADP for the Ag-added alloy aged for 950.4 ks, (b) diffraction pattern for the T phase and (c) schematic illustration of the diffraction pattern for the T phase [16]

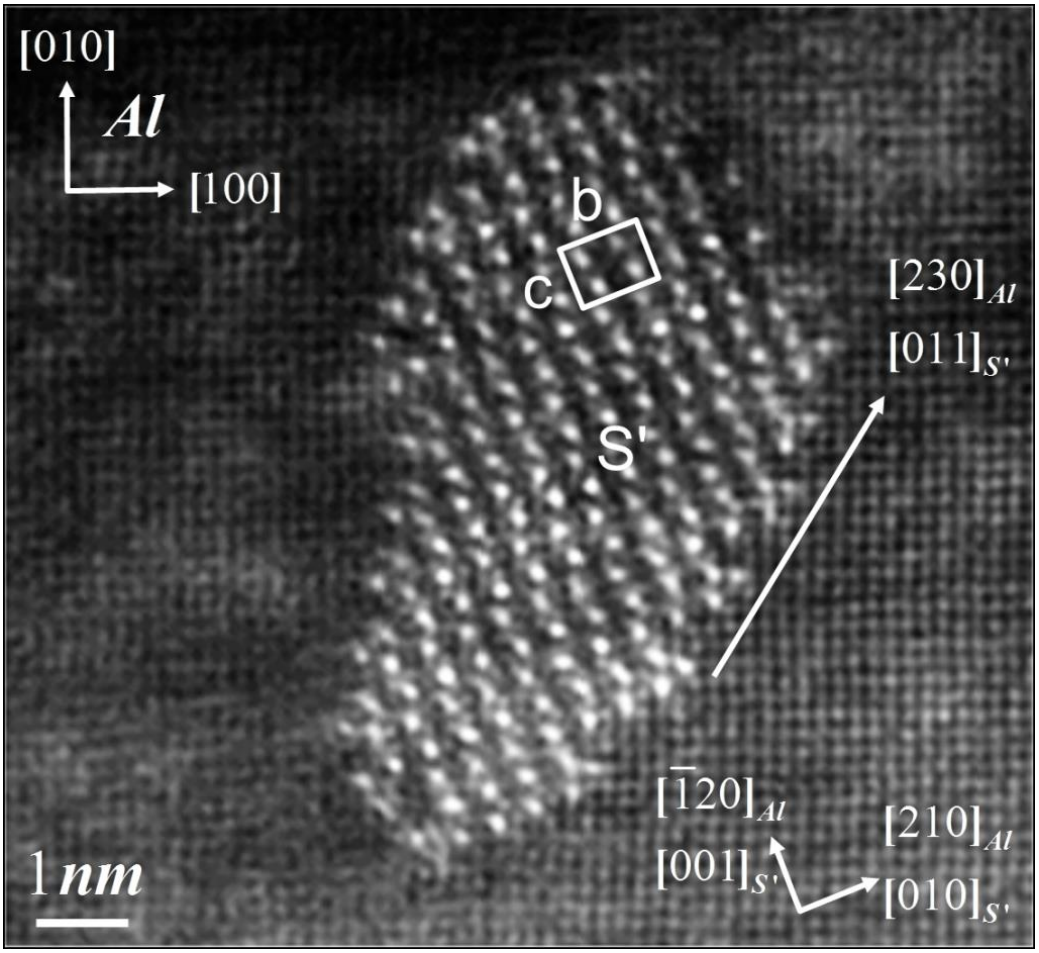

Fig. 5.7 HAADF-STEM image of the <100>$_{Al}$ zone in the Ag-added alloy aged for 950.4 ks, showing a cross-section of S'- rod (along [100]$_{S'}$).

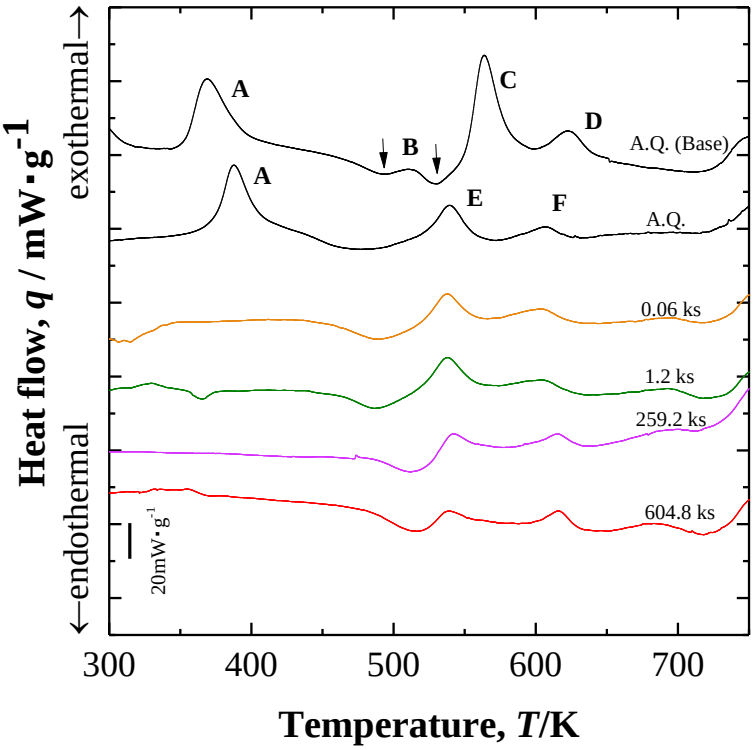

Fig. 5.8 DSC curves for the Ag-added alloy aged at 443 K for various times. For comparison, a curve for A.Q. specimen of the Base alloy is also shown.

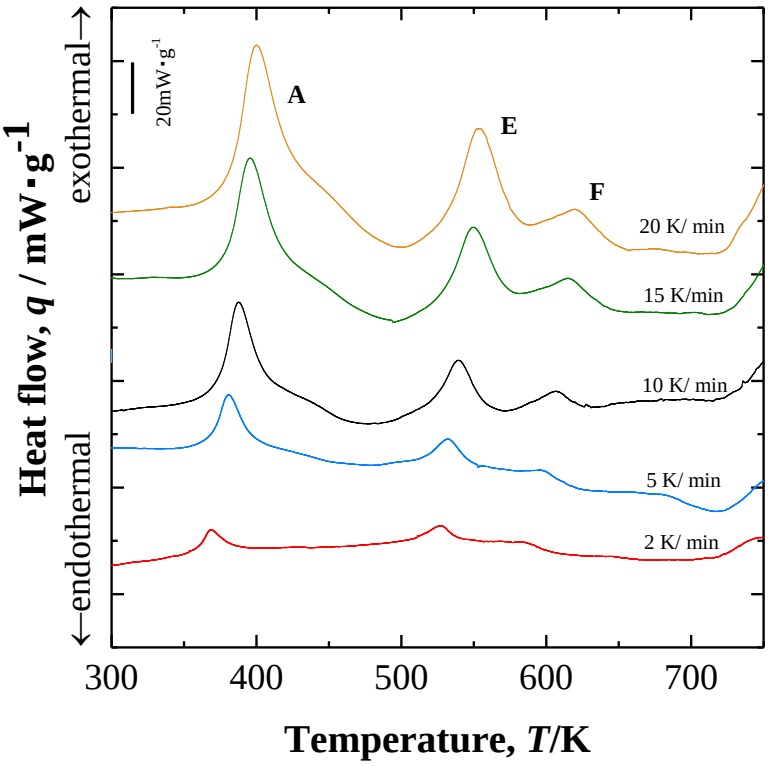

Fig. 5.9 DSC curves for the Ag-added alloy with different heating rate from 2 to 20 K/min.

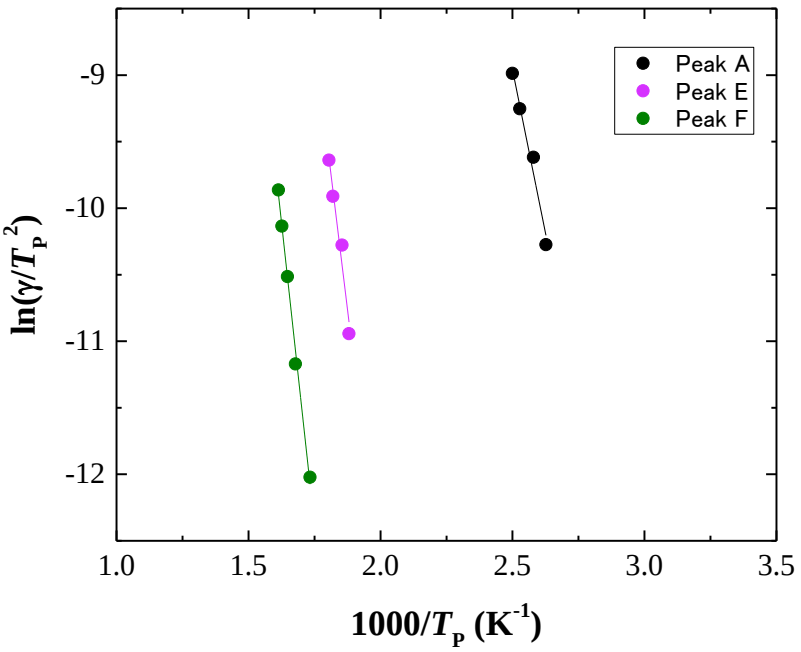

Fig. 5.10 $\ln(\gamma/T_P^2)$ as a function of $1000/T_P$ of Peak A showing the activation energy obtained by using Kissinger's method.

Table 5.2 Activation energy values obtained by Kissinger's method.

Alloy	Activation energy, kJ/mol		
	peak A	peak E	peak F
Ag-added	81.7	135.0	151.2

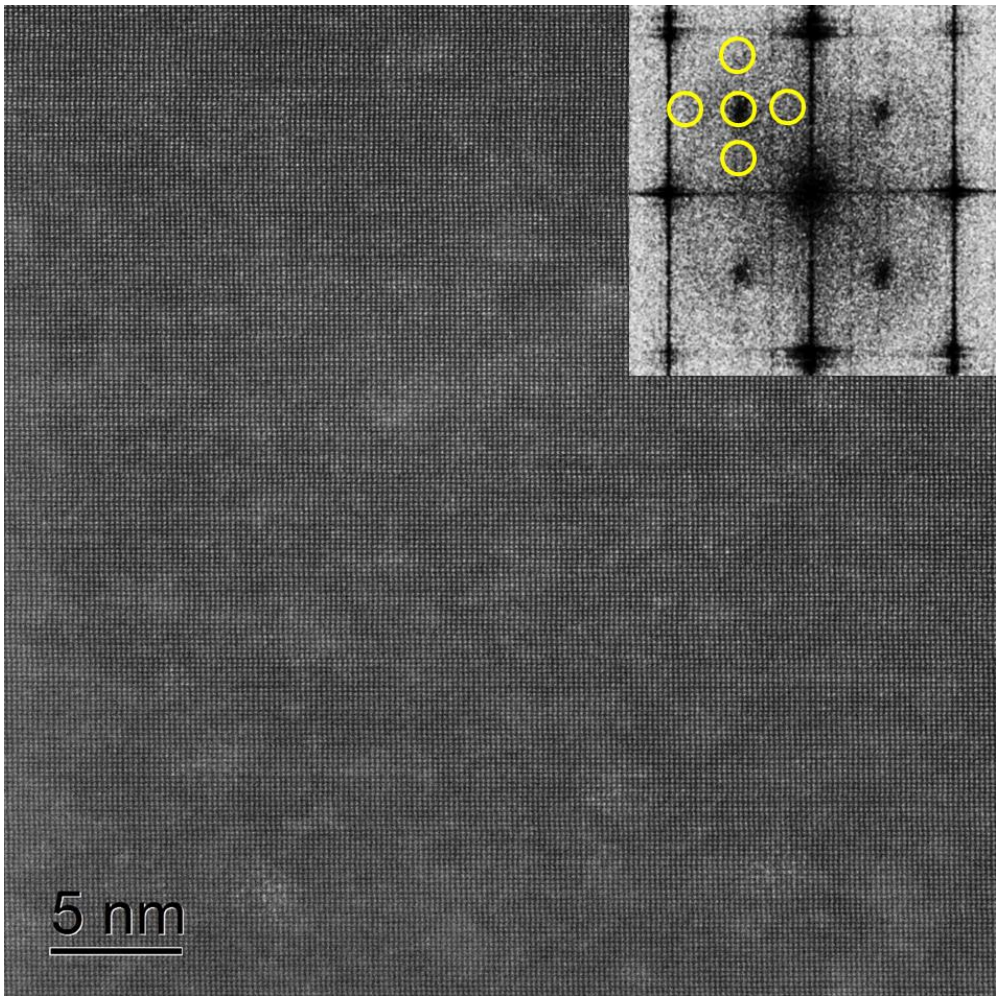

Fig. 5.11 HAADF-STEM image for the Ag-added alloy aged at 443 K for 0.06 ks. FFT shows the same spots as the SADPs obtained for the specimen aged for 10.8 ks [Fig. 5.2 (a)]. The FFT is also the same as the FFT of the HAADF-STEM image for the Base alloy aged at 443 K for 0.06 ks (Fig. 3.3).

(a)

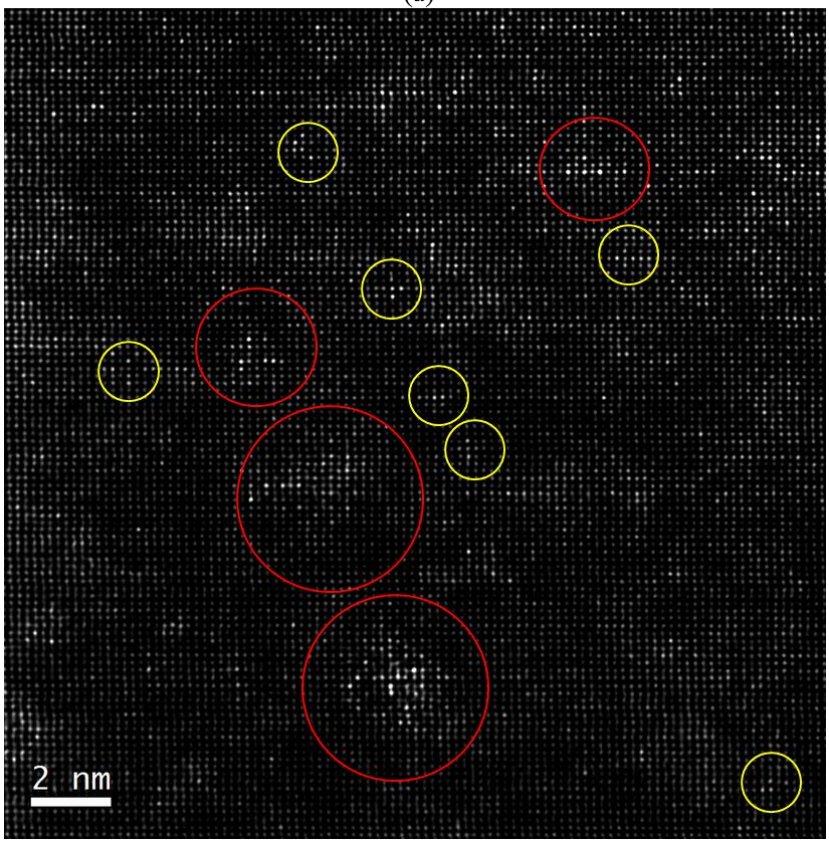

(b)

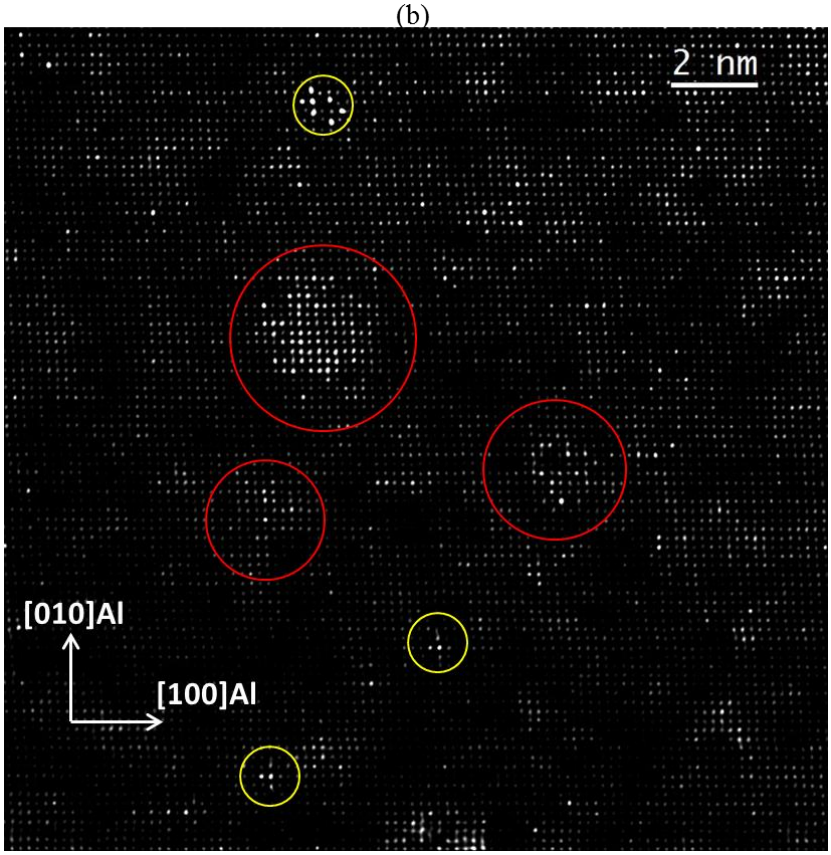

Fig. 5.12 Enlarged HAADF-STEM images for the Ag-added alloy aged at 443 K for 0.06 ks. The microstructure consists of a multitude of structural units of GPB zone (yellow circles) and spherical zones (red circles).

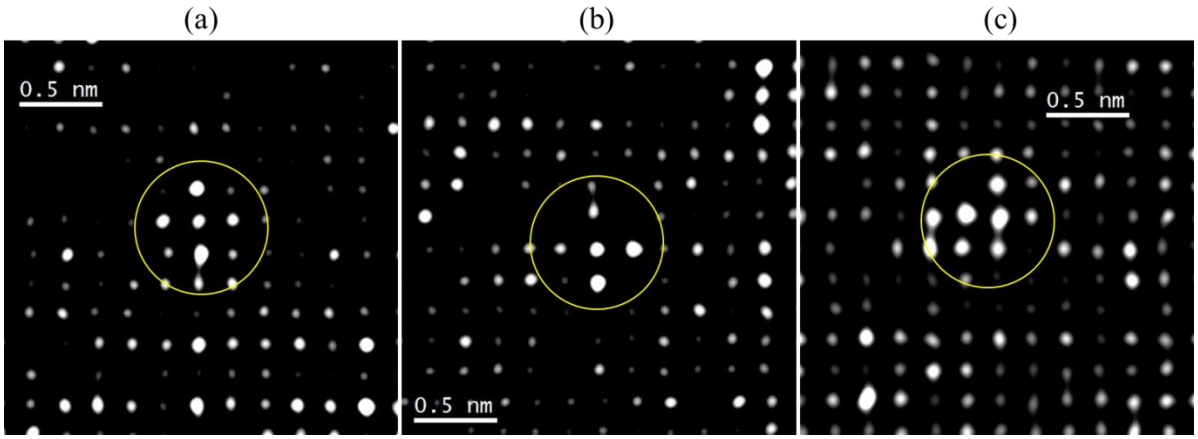

Fig. 5.13 Structural units of GPB zone observed in the Ag-added alloy aged at 443 K for 0.06 ks.

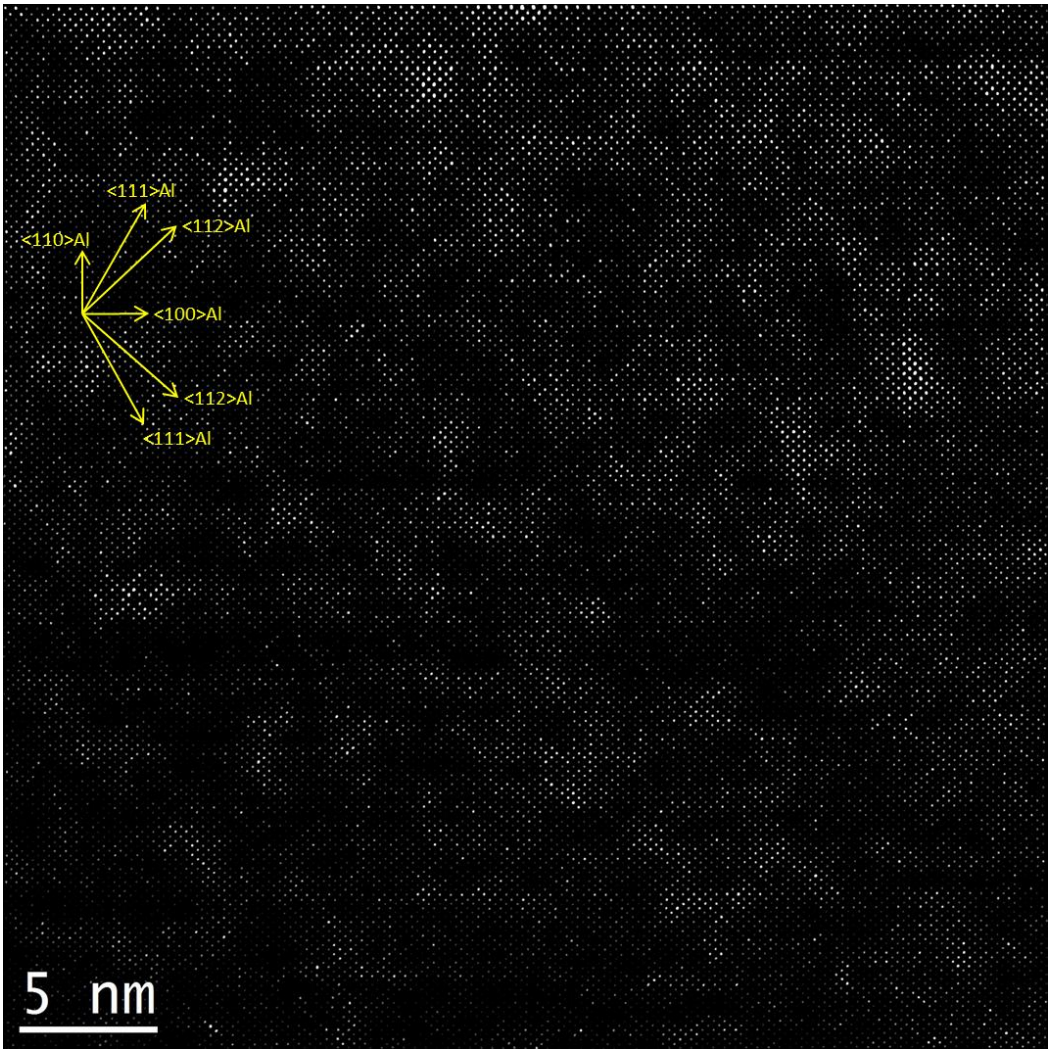

Fig. 5.14 HAADF-STEM image taken in $<110>_{Al}$ zone for the Ag-added alloy aged at 443 K for 0.06 ks. There is no strong indication of preferential growth on $\{111\}_{Al}$ or $\{100\}_{Al}$, suggesting that the observed spherical zones do not have a high aspect ratio.

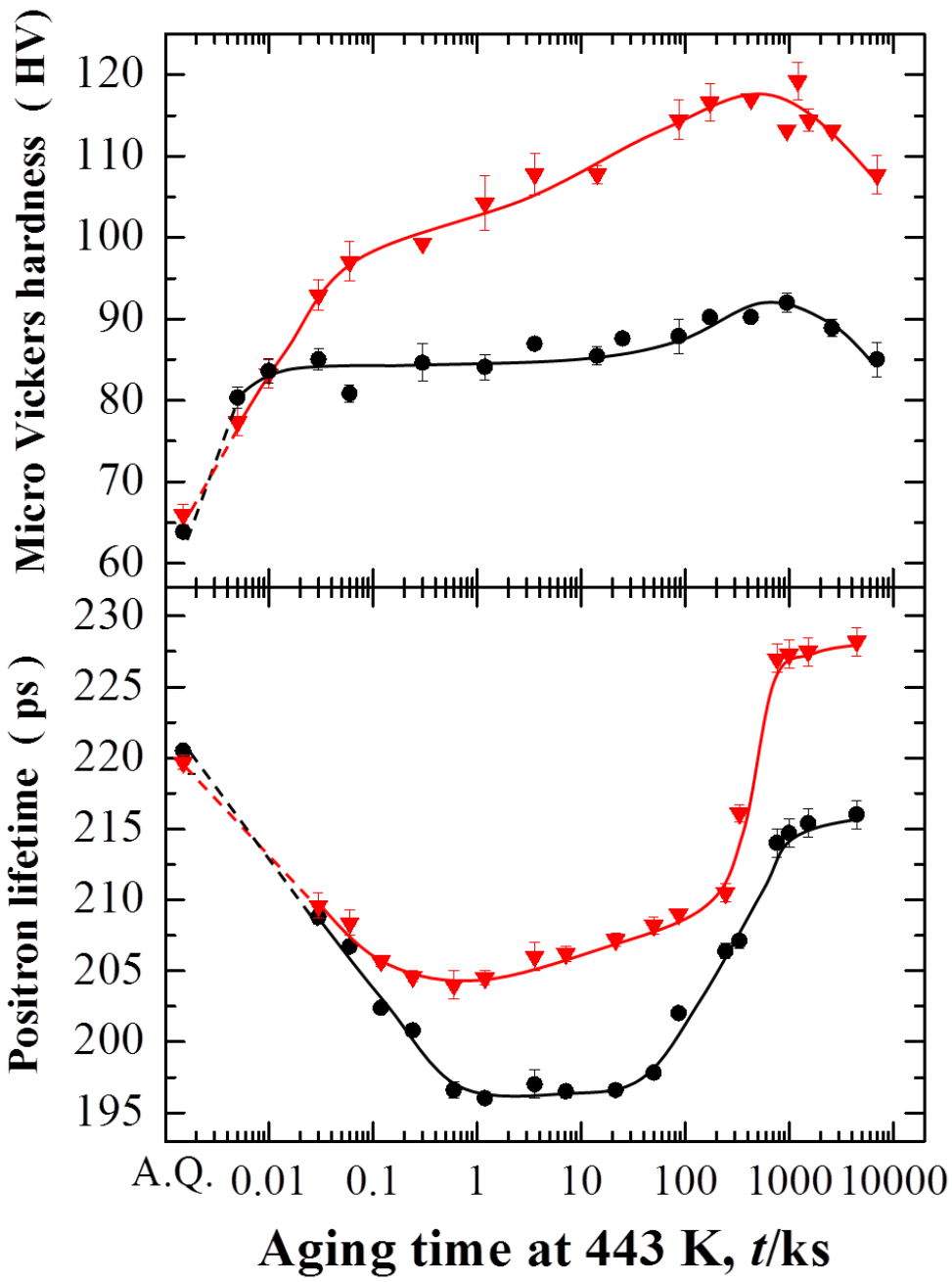

Fig. 5.15 Evolution of the hardness and positron lifetime during aging at 443 K.

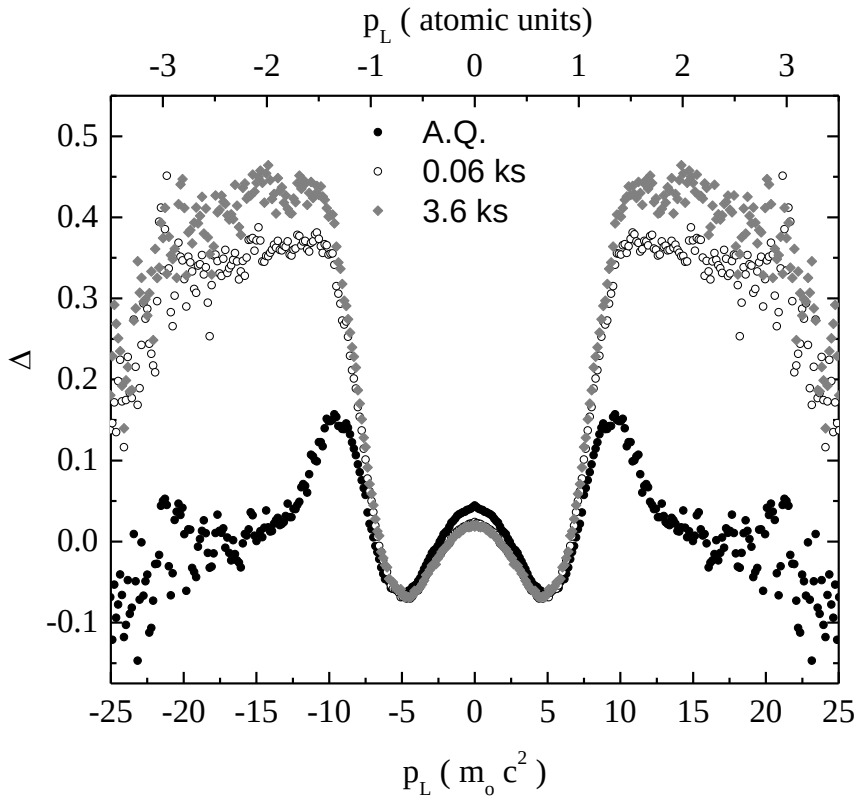

Fig. 5.16 CDB differences curves relative to well-annealed pure Al for the Ag-added alloy aged at 443 K.

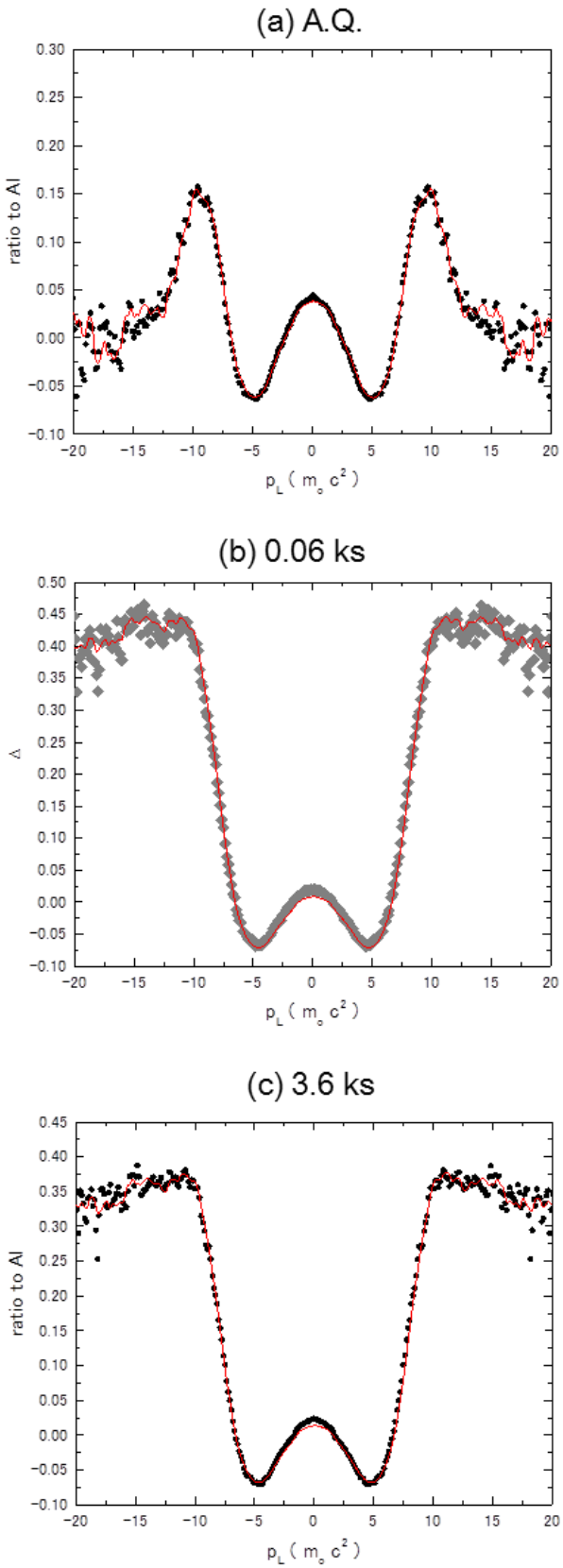

Fig. 5.17 Results of the fitting procedure for the curves in Fig. 6.6 using reference spectra.

Table 5.3 Fractional concentrations of the alloy components in contact with vacancy-like defects in the Ag-added alloy for different aging conditions. These values were obtained by fitting the CDB curves using Eq.(3.9). F_{trap} is the trapping fraction of the positrons annihilated in the Ag-added alloy under the aging conditions.

aging condition	F_{trap} (%)	C_{Al} (%)	C_{Mg} (%)	C_{Cu} (%)	C_{Ag} (%)
A.Q.	58	62	7	25	6
0.06 ks	61	36	16	38	10
3.6 ks	63	32	15	43	10

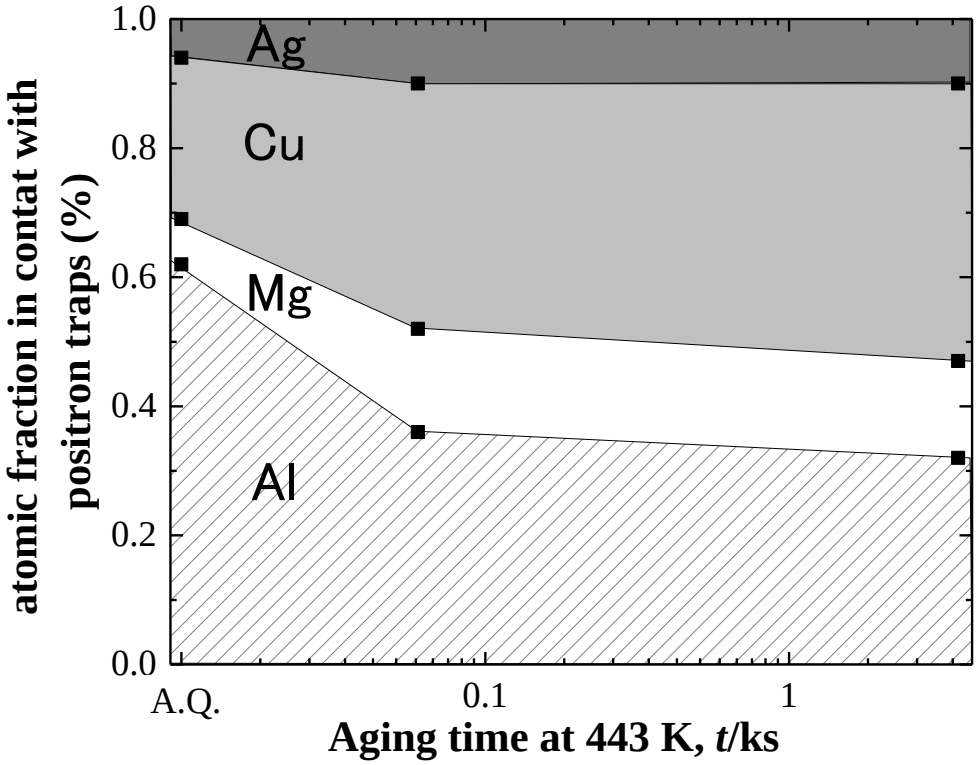

Fig. 5.18 Elemental fractions in contact with vacancies as a function of the aging time at 443 K for the Ag-added alloy.

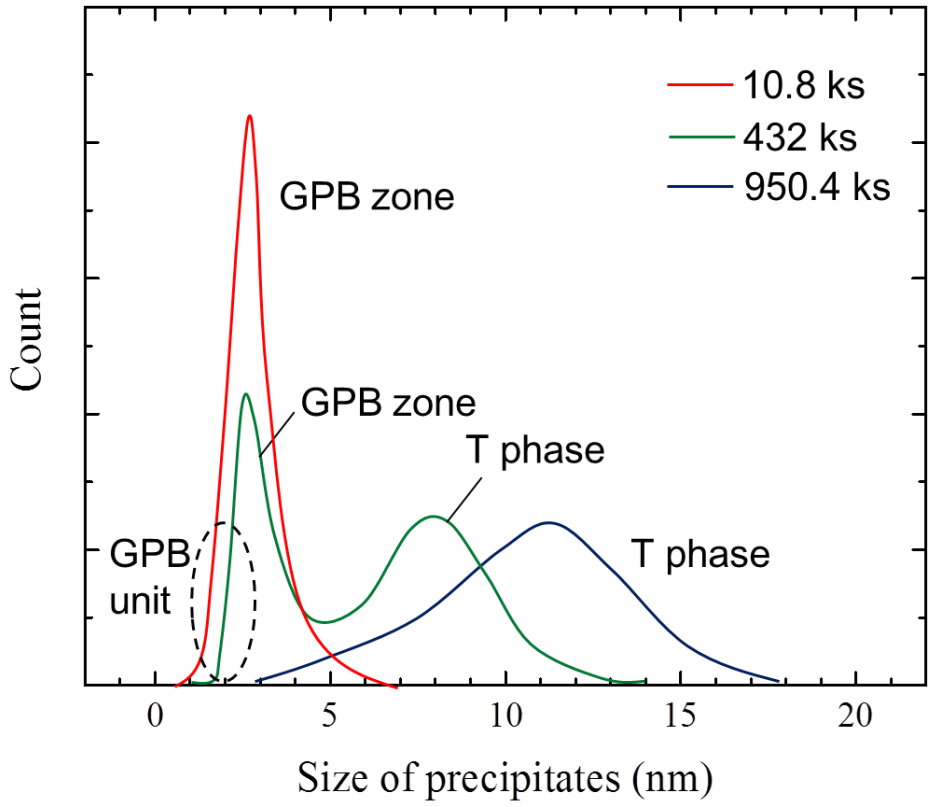

Fig. 5.19 Schematic illustration for the relationship between the precipitates and the double distribution of the size of precipitates.

Chapter 6

General Conclusions

The principle objective of the present thesis is described in **Chapter 1**.

"More precise understanding of the age-hardening behavior in Al-Mg-Cu alloys which lie in (α+S+T) phase field, with particular attention to the rapid age-hardening during the initial decomposition stage" is successfully achieved throughout the previous chapters. Conclusions of the present thesis are summarized in this chapter based on both obtained experimental results as well as discussion described in each chapter.

The background and motivations of the present thesis as well as literature review are described in **Chapter 1** ***"General Introduction"***. The characteristic age-hardening behavior of Al-Cu-Mg based alloys and the importance of the study on solute clustering and vacancy behavior are described.

Characteristic age-hardening behavior of Al-3Mg-1Cu alloys which lie in (α+S+T) phase field is investigated in **Chapter 2** ***"Age-hardening Behavior and Precipitation Sequence in Al-Mg-Cu Alloys"***. A large exothermic peak was detected in the DSC curves for A.Q. state specimens using DSC analysis. This peak disappears after short term aging and is attributed to the formation of nanostructures which is responsible for the rapid age-hardening. After long term aging, three types of precipitates such as GPB zone, S' phase and Z phase are observed. GPB zones are identified as agglomerate of two single units.

The evolution of nanostructures in the initial stage of aging is investigated in **Chapter 3** ***"Evolution of Nanostructures and Role of Vacancies During Initial Stage of Aging in an Al-Mg-Cu Alloy"***. It is revealed that microstructure after aging for short term consists of a multitude of the structural units of the GPB zone by HAADF-STEM investigation. It is the first direct observation for the structural units of GPB zone which form in the initial stage of aging. 3DAP analysis shows strong Cu-Cu correlation after short trem aging. It is clarified

that the rapid age-hardening in Al-Mg-Cu alloys is related to the strong increase in the Cu content in contact with vacancies by PAS investigation.

Age-hardening response of Al-Mg-Cu alloys with different Cu, Mg compositions which lie in (α+S+T) phase field is investigated in **Chapter 4** ***"Effect of Different Cu, Mg Compositions on Age-hardening Behavior in an Al-Mg-Cu Alloy"***. Age-hardening response is improved by increasing amount of Cu or Mg in the alloy composition. Cu addition has strong effect on the rapid age-hardening response. DSC results indicates that increasing amount of Cu promotes the formation of the structural units of GPB zone, although increasing amount of Mg in alloy composition is less effective. PAS investigation clearly indicated that Mg promotes the quenched-in vacancies to be retained during aging. Serrated yielding is observed in stress-strain curves for the investigated alloys. Different alloy compositions do not have significant effect on the serrated yielding behavior. It is indicated that Mg solutes causes the serrated yielding and large amount of solutes which causes the serrated yielding are exist even after long term aging. It is the characteristic feature of Al-Mg-Cu alloys.

The effect of Ag addition on the age-hardening response is investigated in **Chapter 5** ***"Effect of Small Addition of Ag on Age-hardening Behavior in an Al-Mg-Cu Alloy"***. The age-hardenability of the Base alloy is significantly improved by small addition of Ag. It is revealed that the fine distributed precipitates are icosahedral quasi-crystals intermixed with small regions of the cubic approximation T phase. It is also clarified that the microstructures in the Base and Ag-added alloy originate from the same nanostructure, i.e. structural units of GPB zone. Ag addition accelerate the formation of spherical zones, resulted in the uniform dispersion of the precipitates. Based on PAS investigation, Ag addition promotes the

vacancies to be retained after quenching and during aging. The rapid age-hardening in the Ag-added alloy is related to the formation of vacancy-solute (Cu, Mg, Ag) complexes.

In **Chapter 6**, ***"General Conclusions"***, the overall results and research achievements obtained from **Chapter 2** to **Chapter 5** are summarized.